Distribution Agreement

In presenting this thesis or dissertation as a partial fulfillment of the requirements for an advanced degree from Emory University, I hereby grant to Emory University and its agents the non-exclusive license to archive, make accessible, and display my thesis or dissertation in whole or in part in all forms of media, now or hereafter known, including display on the world wide web. I understand that I may select some access restrictions as part of the online submission of this thesis or dissertation. I retain all ownership rights to the copyright of the thesis or dissertation. I also retain the right to use in future works (such as articles or books) all or part of this thesis or dissertation.

Signature:

_____   _____

Yimin Wang   Date

Theoretical Studies of
Unusual Molecular Vibrational Dynamics

By

Yimin Wang
Doctor of Philosophy

Chemistry

Joel M. Bowman, Ph.D.
Advisor

Michael C. Heaven, Ph.D.
Committee Member

James T. Kindt, Ph.D.
Committee Member

Accepted:

Lisa A. Tedesco, Ph.D.
Dean of the James T. Laney School of Graduate Studies

Date

Theoretical Studies of Unusual Molecular Vibrational Dynamics

By

Yimin Wang

B.S., University of Science and Technology of China, 2005

Adivsor: Joel M. Bowman, Ph.D.

Abstract

Theoretical Studies of Unusual Molecular Vibrational Dynamics

By Yimin Wang

With the recent progress by Braams, Bowman and co-workers, potential energy surface and dipole moment surface of polyatomic systems with up to 10 atoms can now be constructed pretty routinely by doing linear least-squares fit to tens of thousands of scattered *ab initio* energies. The key feature of these surfaces is that the invariance with respect to all permutations of like atoms. Such property is of truly importance to study the highly fluxional systems such as H_5^+. Additionally, by incorporating the permutational invariance explicitly into the function representation, we not only obtain a compact fitting basis, but also reduce the size of the electronic energy data-set to a great extent.

Taking advantage of the above fitting technique, we successfully developed a highly accurate full-dimensional potential energy surface of a nine-atom molecule, malonadehyde, based on only 11 147 near basis-set-limit frozen-core CCSD(T) electronic energies. This potential energy surface has been used in a full-dimensional quantum study of hydrogen-atom transfer reaction of malonaldehyde using diffusion Monte Carlo simulation and a variational method, and obtained tunneling splitting in excellent agreement with the experiment. We very recently developed a full-dimensional, flexible potential energy surface for arbitrary numbers of water monomers built from *ab initio* 2- and 3-body potentials. These potentials are each permutationally invariant fits to roughly 30 000 electronic energies. Tests of these potentials are made against direct high-level *ab initio* results for the water dimer, trimer and hexamer.

The last part of this work devotes to several simple models for post-harmonic quantum vibration analysis on the full-dimensional *ab initio* potential energy surface. We report a local-mode mode model to calculate OH-stretch fundamentals of water clusters and and a new local-monomer model that describes both anharmonic stretches and bends. Furthermore, we present tunneling calculations using a one-dimensional Hamiltonian in the imaginary-frequency, rectilinear normal mode of a saddle point, for the zero angular momentum state. Finally, a similar one-dimension Hamiltonian in normal coordinate has also been used to perform Frank-Condon analysis of the ionization thresholds of the two isomers of C_3H.

Theoretical Studies of
Unusual Molecular Vibrational
Dynamics

By

Yimin Wang

B.S., University of Science and Technology of China, 2005

Adivsor: Joel M. Bowman, Ph.D.

A dissertation submitted to the Faculty of the
James T. Laney School of Graduate School of Emory University
in partial fulfillment of the requirements for the degree of
Doctor of Philosophy
in Chemistry
2010

Acknowledgements

Of the many people who deserve thanks, some are particularly prominent, such as my supervisor, Professor Joel M. Bowman. Through him, I have not only become a better writer and overall thinker, but I have also learned what good science is. He has strengthened my understanding of how to research effectively and think creatively, and continues to serve as an important role-model for me.

Another such person is Dr. Bas Braams. The tangible and intangible benefits of collaboration with him are too numerous to list. He also is the one who inspires me to appreciate the differences between mathematicians and scientists. I would never forget any single productive discussion we had in Joel's sunny office. I would also like to thank Dr. Stuart Carter and Dr. Xinchuan Huang for their constant support on the use of the code MULTIMODE, and Dr. Alex Kaledin for introducing me to the statistical world of quantum molecules.

I must also express my gratitude to the numerous students and research fellows with whom I have shared office and computing facilities. These, together with the administrative staff, have made my days in Emory as a PhD student enjoyable and interesting. My deepest appreciation is also dedicated to my friends and family, whose companion and encouragement are always a faithful source of strength and joy throughout my life.

Last but not least, my thank goes to Professor Keiji Morokuma whose faithful commitment to research significantly influences my attitude towards pursuing scientific accomplishment. I must also thank Professor Michael Heaven and Professor James Kindt for agreeing to take the time to be members of my graduate study committee.

Contents

II. Full-dimensional Quantum Approaches   42

4. Diffusion Monte Carlo   43

III. Approximate Quantum Models   106

8. Intramolecular Vibrations of Clusters   107

9. One-dimensional tunneling calculations   121

List of Tables

List of Figures

Citations to Previously Published Work

Large portions of Chapters 3 and 8 have appeared in the following three papers:

"Towards an ab initio flexible potential for water, and post-harmonic quantum vibrational analysis of water clusters", Y. Wang and J. M. Bowman, Chem. Phys. Lett. **491**, 1 (2010);

"Full-dimensional, ab initio potential energy and dipole moment surfaces for water", Y. Wang, B. C. Shepler, B. J. Braams, and J. M. Bowman, J. Chem. Phys. **131**, 054511 (2009);

"Accurate ab initio and "hybrid" potential energy surfaces, intramolecular vibrational energies, and classical ir spectrum of the water dimer", A. Shank, Y. Wang, A. Kaledin, B. J. Braams, and J. M. Bowman, J. Chem. Phys. **130**, 144314 (2009);

"MULTIMODE quantum calculations of intramolecular vibrational energies of the water dimer and trimer using ab initio-based potential energy surfaces", Y. Wang, S. Carter, B. J. Braams, and J. M. Bowman, J. Chem. Phys. **128**, 071107 (2008).

Most of Chapter 6 has been published as

"Full-dimensional quantum calculations of ground-state tunneling splitting of malonaldehyde using an accurate ab initio potential energy surface", Y. Wang, B. J. Braams, J. M. Bowman, S. Carter, and D. P. Tew, J. Chem. Phys. **128**, 224314 (2008).

Chapter 7 appears in its entirety as

"Shared-Proton Mode Lights up the Infrared Spectrum of Fluxional Cations H_5^+ and D_5^+", T. C. Cheng, B. Bandyopadyay, Y. Wang, S. Carter, B. J. Braams, J. M. Bowman, and M. A. Duncan, J. Phys. Chem. Lett. **1**, 758 (2010).

The numerical methods of Chapter 9 appears in the following paper:

"One-dimensional tunneling calculations in the imaginary-frequency, rectilinear saddle-point normal mode", Y. Wang and J. M. Bowman, J. Chem.

Phys. **129**, 121103 (2008);

"Reduced-Dimensional Quantum Approach to Tunneling Splittings Using Saddle-Point Normal Coordinates" E. Kamarchik, Y. Wang, and J. M. Bowman, J. Phys. Chem. A **113**, 7556 (2009).

Finally, Chapter 10 has been reported as

"Ab Intio Based Potential Energy Surfaces and Franck-Condon Analysis of Ionization Thresholds of Cyclic-C_3H and Linear-C_3H", Y. Wang, B. J. Braams, and J. M. Bowman, J. Phys. Chem. A **111**, 4056 (2007).

Dedicated to my fathr Xumin,
my mother Chaoxian,
and my beloved grandparents.

Chapter 1.

Introduction

1.1. Everything Starts from the Born-Oppenheimer Approximation ...

Molecules of any type are governed by the Schrödinger equation, except in some really extreme cases. When relativity is neglected, then the wave-function describing the motion of a given isolated system (with zero external field) of electrons and nuclei may be obtained from the solution of the time independent Schrödinger equation. The complete Hamiltonian for such system is the sum of kinetic energy operators for the nuclei and for the electrons, plus the various potential energy terms as follows

$$\hat{H} = \hat{T}_e + \hat{T}_n + \hat{V}_e + \hat{V}_{ne} + \hat{V}_n, \tag{1.1}$$

here the kinetic energy operator $\hat{T}_e$ operates only on the electron coordinates, and $\hat{T}_n$ only on the nuclear coordinates, and the potential terms are defined in a similar fashion. More specifically, the Schrödinger wave equation then has for a stationary

state the form

$$\left(-\frac{h^2}{8\pi^2 m} \sum_i \nabla_i^2 - \sum_j \frac{h^2}{8\pi^2 M_j} \nabla_j^2 + \sum_{i<i'} \frac{e^2}{r_{ii'}} - \sum_{i,j} \frac{Z_j e^2}{r_{ij}} + \sum_{j<j'} \frac{Z_j Z_{j'} e^2}{r_{jj'}} \right) \Psi = E\Psi,$$

(1.2)

where summations over i and i' are over the electrons, and the summations over j and j' are over the nuclei. In the first term m has no index because all electrons have the same mass. The M_j denotes the mass of the jth nucleus, and the Z_j refers to the number of protons in it. The distance between two electrons, two nuclei, and nucleus j and electron i is denoted by $r_{ii'}$, $r_{jj'}$, and r_{ij} respectively. The function Ψ here is the total wave-function and E the total energy.

However, even for the simplest molecule, H_2^+, consisting of only one electron and two nuclei, the Schrödinger equation cannot be solved analytically. We have to make an approximation. In 1927, Born and Oppenheimer proposed the famous Born-Oppenheimer approximation [1]. Because of the great difference in masses of electrons and nuclei, the electrons can adjust their motions almost instantaneously to the displacement of the nuclei. This approximation thus suggests a solution of the total wave-function of the form

$$\Psi(\mathbf{r}_e; \mathbf{R}_n) = \psi^{elec}(\mathbf{r}_e; \mathbf{R}_n)\, \Phi^{nuc}(\mathbf{R}_n),$$

(1.3)

where ψ^{elec} is the electronic wave-function which is function of the electronic coordinates $\mathbf{r}_e$ and also depends parametrically on the nuclear coordinates $\mathbf{R}_n$, and Φ^{nuc} is the nuclear wave-function that depends solely on the positions of the nuclei. Now we

substitute this trial solution into Equation 1.2, and obtain

$$\Phi^{nuc}\left(\hat{T}_e\psi^{elec} + (\hat{V}_e + \hat{V}_{ne})\psi^{elec}\right) + \psi^{elec}\left(\hat{T}_n\Phi^{nuc} + \hat{V}_n\Phi^{nuc}\right) + W = E\,\psi^{elec}\,\Phi^{nuc},$$

(1.4)

where

$$W = -2\sum_j \frac{h^2}{8\pi^2 M_j}\left(\nabla_j\psi^{elec}\,\nabla_j\,\Phi^{nuc} + \Phi^{nuc}\,\nabla_j^2\psi^{elec}\right).$$

(1.5)

The quantity W is non-zero because ψ^{elec} depends on the nuclear coordinates, and thus $\nabla_j\psi^{elec}$ is not zero. However, because the nuclear masses are at least three orders of magnitude greater than that of the electron, we see that W is small and thus negligible. In such case, it is approximately equivalent to solve the following two equations sequentially,

$$\left(\hat{T}_e + \hat{V}_e + \hat{V}_{ne} + \hat{V}_n\right)\psi^{elec}(\mathbf{r}_e; \mathbf{R}_n) = E_e(\mathbf{R}_n)\psi^{elec}(\mathbf{r}_e; \mathbf{R}_n),$$

(1.6)

$$\left(\hat{T}_n + E_e(\mathbf{R}_n)\right)\Phi^{nuc}(\mathbf{R}_n) = E_N\Phi^{nuc}(\mathbf{R}_n).$$

(1.7)

Therefore, instead of trying to solve the Schrödinger equation for all the particles simultaneously, we solve the Schrödinger equation for the electrons (Equation 1.6) at each instantaneous configuration of the nuclei, and obtain a set of eigenvalues $E_e(\mathbf{R}_n)$ for each particular arrangement of the nuclei. A sufficiently large set of $E_e(\mathbf{R}_n)$ would allow us to determine a function representation of those values. The function representation is known as the potential energy curve of a diatomic molecule or, in general, a potential energy surface (PES) of a polyatomic system. With the PES in hand, we could then be ready to solve the Schrödinger equation of the nuclei (Equation 1.7). This is exactly the strategy we employ for studies throughout this work.

1.2. Structure of the Thesis

This work is broadly arranged into three parts.

The very first part goes to the potential energy surface (PES), a cornerstone of all our work. In Chapter 2, we describe two approaches to determine the functional representation of the PES that is invariant with respect to all permuations of like nuclei, along with technical details of the applications in practice. In Chapter 3, we present the potential energy surface of water as a real application of techniques mentioned in the previous chapter.

Moving onto the second part, we review two full-dimensional quantum-mechanical approaches to solve the nuclear motion of the molecular system. We describe the Diffusion Monte Carlo method and vibrational configuration interaction calculation in Chapter 4 and Chapter 5, respectively. Theories and implementation are discussed. In the following two chapters, we present two full-dimensional quantum studies using both methods. For Malonaldehyde in Chapter 6, we will focus on determining the ground state H-transfer tunneling splitting, and in Chapter 7 we want to calculate the infrared spectrum for both H_5^+ and D_5^+.

In the last part, we describe several approximate quantum models, along with their applications. In Chapter 8, we introduce local methods to obtain the intramolecular vibrations of water clusters up to ten water monomers using the water PES we developed, and benchmark the results against accurate MULTIMODE calculations for the water dimer and trimer. In Chapter 9, we present one-dimensional tunneling calculations in the imaginary-frequency, rectilinear saddle-point normal mode. Although these calculations are based on full-dimensional PESs, we show that this method can easily be extended to large molecular systems, for which the PES is not easy to obtain.

In the final chapter, we apply Franck-Condon analysis in reduced dimensionality to determine the ionization thresholds of cyclic-C_3H and linear-C_3H.

Part I.

Potential Energy Surface

Chapter 2.

Potential Energy Surface

In the Born-Oppenheimer approximation (sometimes referred to as the adiabatic approximation) the electrons move so much faster than the nuclei that the electrons follow the motion of nuclei instantaneously. In such case, the electronic degrees of freedom are separated from those of the atomic nuclei in the time independent Schrödinger equation, and be solved independently. The solution of the electronic motion at a given nuclear configuration leads to a single point on the so-called potential energy surface (PES). Thus, the potential energy can be regarded as a function of the nuclear structure of a molecular system. For the diatomic molecule, the PES would simply be a curve, of which the x-axis represents the internuclear distance of the two atom and the y-axis represents the solution of its electronic motion. For the polyatomic molecule, the PES would be a much more complicated hyper-dimensional function.

In principle we could solve the Schrödinger equation of the electrons at all relevant nuclear configurations. However, this is extremely computer intensive and thus not practical for many applications, especially quantum ones. There is, therefore a long history of exploring the functional representation of the potential energy. It is almost

impossible to find the exact analytical function form of the PES of any molecule. All we can do is to fit the electronic energies accurately to a proposed mathematical function. But this is still not an easy task especially for the PESs in high dimensionality. A well-behaved mathematical function is the key. The ideal function should not only have the correct asymptotic behavior and have a reasonable number of free coefficients that are easy to fit while still sufficient to represent the complexity of the multi-dimensional surface, but also incorporate permutational symmetry directly of the molecule contains two or more identical atoms, i.e. the invariance of potential energy with respect to all permutations of identical nuclei.

The importance of the permutational invariance has been well-discussed in the literature (REF) and in a variety of recent studies (REF). One easy approach to enforce permutationally symmetry can be done by replicating electronic energies for permutationally equivalent atomic configurations and then fit the enlarged dataset, as was don for both C_2H_2 [2] and H_2CO [3]. The fitted PES could certainly be at least numerically invariant to permutations of identical atoms; however, the number of free coefficients of the fitting basis has be sufficiently large in order to represent the additional data. This is a not a feasible approach for a molecule such as the water trimer, $(H_2O)_3$, where the number of permutations is $4!6!=4\,320$ and the enlarged dataset will be $4\,320$ times as large as the original one.

Clearly a better way to construct permutationally invariant PES is to use a target function that naturally incorporates such invariance by design. The implementation of this approach is by no means trivial. Murrell *et. al.* in their book published in 1984 [4] suggested representing the potential function in terms of what they called an "integrity basis". The techniques they used to generate such basis are in their words rather tedious and to the best of our knowledge have not been developed beyond three and four identical atoms by this group [5].

Two techniques we developed to generate invariant fitting basis will be presented in the following two sections, followed by remarks of both methods. We will talk about related techniques to represent the dipole moment briefly in Section 2.4, and close this chapter with the practical procedures to construct the PES and a summary of potential energy surfaces used in studies presented in latter chapters.

2.1. Monomial Symmetrization

The first approach, which we denote as monomial symmetrization, is relatively transparent and easy to understand compared with the second approach. Details of this approach have been described elsewhere [6,7]. Here we will only take the water monomer for example to illustrate the spirit of this method. The coordinate system of choice in our two approaches is the set of all internuclear distances. For the H_2O molecule labelled as O(1), H(2), H(3), there are three internuclear distances, $\{r_{12}, r_{13}, r_{23}\}$. These internuclear distances are then transformed to Morse variables $\{y_{ij}\}$ defined by $y_{ij} = \exp(-r_{ij}/\lambda)$, where the parameter λ has the same unit as the distance and is not fitted but determined through experience. In fact, our experience indicates that the fits are generally insensitive to the precise value of λ given it is in the range of 1.5 - 3.0 bohr; a typical value is 2.0 bohr.

To begin with, we represent the potential by the following expansion in monomials of Morse variables:

$$V(\mathbf{y}) = \sum_{m=0}^{M} C_{abc} \left[y_{12}^a \, y_{13}^b \, y_{23}^c \right]; \quad (m = a + b + c), \tag{2.1}$$

where a, b, c are all integers. The summation is over all powers of y_{ij} subject to the constraint that the total degree m is at most M. We can now directly do a least-squares fit to determine the linear coefficients and obtain an analytical expression of

the PES. However, unless the dataset includes all permutationally equivalent configu-
rations, the invariance property of the PES is not guaranteed. This can be shown by
first fixing the orders of one monomial, $y_{12}^a\, y_{13}^b\, y_{23}^c$. Next, consider the permutation of
the H(2) and H(3). The monomial $y_{12}^a\, y_{13}^b\, y_{23}^c$ then maps onto $y_{13}^a\, y_{12}^b\, y_{32}^c$, which can be
rewritten as the original monomial with permuted powers as $y_{12}^b\, y_{13}^a\, y_{23}^c$. Clearly, there
is no guarantee that the corresponding coefficients, C_{abc} and C_{bac} would be equal, with
the exception when the permutation symmetry was included implicitly as mentioned,
the numerically equality of the two coefficients might be achieved. On the other hand,
this illustration also suggests that the permutation symmetry can be easily ensured
by using a single coefficient for both terms; the symmetrized expression of potential
reads,

$$V(\mathbf{y}) = \sum_{m=0}^{M} D_{abc} \left[y_{12}^a\, y_{13}^b\, y_{23}^c + y_{12}^b\, y_{13}^a\, y_{23}^c \right] ; \quad (m = a + b + c), \tag{2.2}$$

where we can see the invariance property is incorporated explicitly into the fitting
basis function.

In general, the permutationally invariant potential function of any N-atom molecule
can be written as,

$$V(\mathbf{y}) = \sum_{m=0}^{M} D_{n_1 n_2 \cdots n_K} \, \mathcal{S} \left[y_{12}^{n_1} y_{13}^{n_2} \cdots y_{K-1K}^{n_K} \right] ; \quad (K = N(N-1)/2; \; m = \sum_{i=1}^{K} n_i),$$

$$\tag{2.3}$$

where '$\mathcal{S}$' is the operator that symmetrizes monomials, or more specifically that adds
up all permutationally equivalent monomials. Obviously, the number of equivalent
monomials is equal to the number permutations, that is 2!=2 for the H_2O molecule
and $n! m! \cdots p!$ for any arbitrary $\mathbf{A}_n \mathbf{B}_m \cdots \mathbf{X}_p$ molecule. The number of coefficients
in each representation can be obtained explicitly using the Molien series given below.

Recently this approach was implemented by Xie and Bowman in C++ and successfully applied to obtain a new PES of H_3O^+ [7].

2.2. Invariant Polynomials

The second approach, based on the invariant polynomial theory, is mathematically more elegant and leads to a very compact expression that is more efficient to evaluate compared with the first one. We refer to Ref. [8] for a statement of the invariant polynomial theory as well as for a proof of the theory, which will not be given here.

The theory of invariant polynomial says that the function like Equation 2.3 has a representation in terms of primary and secondary invariants as follows,

$$V(\mathbf{y}) = \sum_{d=0}^{M} C_{\alpha\beta}\, h_\alpha(\mathbf{p}(\mathbf{y}))\, q_\beta(\mathbf{y}); \quad (d = \deg(h_\alpha) + \deg(q_\beta)), \qquad (2.4a)$$

$$h_\alpha(\mathbf{p}(\mathbf{y})) = p_1(\mathbf{y})^{n_1} p_2(\mathbf{y})^{n_2} \cdots p_K(\mathbf{y})^{n_K}; \ (K = N(N-1)/2; \ \deg(h_\alpha) = \sum_{i=1}^{K} n_i \deg(p_i)),$$
$$(2.4b)$$

where $\mathbf{p}(\mathbf{y}) = \{p_i(y)\}$ denotes the primary invariant polynomials and $\{q_\beta(\mathbf{y})\}$ the secondary invariant polynomials, and h_α is an arbitrary polynomial of the primary invariants given as Equation 2.4b. The summation is terminated whenever the total degree d exceeds the maximum value M.

Finding the primary and secondary invariant polynomials is non-trivial and thus will not be discussed here. We used computational algebra softwares such as MAGMA[9, 10] to generate these polynomials. The number of primary invariant polynomials is equal to the number of Morse variables, $i.e.$, the number of internuclear distances,

$N(N-1)/2$ for an N-atom system. While the number of secondary polynomials is not easily expressed in terms of the number of variables or the order of the symmetry group, and thus is not easy to compute. Molien series can be used to calculate the total number of invariant polynomials at a given maximum degree M. This series is the power series defined by

$$\mathbf{M}(t) = \left(\sum_{e_\beta \leq M} t^{e_\beta} \right) \prod_{i=1}^{K} \frac{1}{1 - t^{d_i}}; \quad (d_i = \deg(p_i(\mathbf{y})); \; e_\beta = \deg(q_\beta)) \qquad (2.5)$$

where p_i has degree d_i and q_β had degree e_β.

2.3. Remarks

The invariant basis functions generated by the two approaches are unsurprisingly numerically equivalent, but with different mathematical expressions. In the second approach, based on the invariant polynomial theory, each basis function can be perfectly factorized as a single product of one secondary invariant polynomial and a monomial of primary invariant polynomials of a certain degree. Such elegant factorization gains the maximum efficiency in terms of single-processor evaluation of the basis functions. The number of float point multiplications per basis evaluation is bounded by the total number of basis functions multiplied by the maximum total degree. One the other hand, the symmetrized monomial basis is completely unfactorized. The straightforward evaluation of such basis results in the low bound in terms of the efficiency. The cost of such evaluation is bounded by the total number of basis functions multiplied by the product of the maximum total degree and the total number of symmetry groups. Clearly, we see a huge difference between the two upper bounds of the computational cost.

The pay-off of the invariant polynomials being perfectly factorized is the difficulty in deriving the analytical expression of the gradient, which is used very often in many molecular simulation algorithms, e.g. the molecular dynamics calculation. Computing the numerical gradient using a two-point central difference formula would be much expensive than the potential evaluation by a factor of twice the dimension. By contrast, it is trivial to obtain analytical gradient for the symmetrized monomials.

To improve the efficiency of the evaluation of symmetrized monomial basis, Xie et. al. developed a systematic way to factorize as many as possible the polynomial bases into products of two lower order polynomials possibly with subtracting a small number of same-order polynomials [7]. In some cases, the basis generated by the monomial symmetrization approach runs nearly as fast as that obtained by invariant polynomial theory.

2.4. Dipole Moment

The dipole moment surface (DMS) cannot be represented solely in terms of the internuclear distances because the dipole moment is a vector quantity, and the fit ultimately depends on the user's choice of the Cartesian coordinate system. Thus we need to have a slightly different expression for the dipole in terms of invariant polynomials. First, we represent the dipole moment $\vec{\mu}$ as a product of effective charges and Cartesian coordinates:

$$\vec{\mu}(\mathbf{y}) = \sum_i f_i(\mathbf{y}(\mathbf{X})) \, \vec{x}_i \tag{2.6}$$

where $\mathbf{X}$ denotes the Cartesian coordinates of the molecule, $\mathbf{y}(\mathbf{X})$ are again the Morse variables at the configuration $\mathbf{X}$, $f_i(\mathbf{y}(\mathbf{X}))$ is the effective charges on the ith atom (this effective charge ultimately depends on $\mathbf{X}$) and $\vec{x}_i$ is the Cartesian coordinates of the

i^{th} atom. Now since effective charges are scalar quantities, we can apply exactly the same approach to fit the effective charge $f_i(\mathbf{y})$ individually as we do for the PES.

It appears that the expansion of the dipole moment is essentially the same as that of the potential. The caveat is that not only the single effective charge should be invariant with respect to the permutation of like atom as the potential does, but also the effective charges of like atoms should be covariant to permutations. By "covariant" we mean that if the configuration $\mathbf{X}$ is transformed into $\mathbf{X}'$ by interchange of identical nuclei i and j, then the pair of effective charges $(f_i(\mathbf{y}(\mathbf{X})), f_j(\mathbf{y}(\mathbf{X})))$ is equal to the pair $f_j(\mathbf{y}(\mathbf{X}')), f_i(\mathbf{y}(\mathbf{X}')))$. So far, the covariant property has not yet been incorporated explicitly into the fitting basis, but rather we used a somewhat indirect and not quite optimal approach. Details can be found elsewhere [6].

2.5. Practical Procedure

Once we have the invariant polynomial basis functions implemented, we often use a two-step procedure to construct a PES and/or a DMS. It is worth noting that this procedure is developed solely based on our experience so that alternative means may as well be appropriate.

STEP 1: INITIAL SAMPLING OF THE CONFIGURATION SPACE. We often start with *ab initio* molecular dynamics (AIMD, also called direct molecular dynamics) calculations using some low-level electronic structure method, such as the density functional theory (DFT), and a small basis, e.g., VDZ. The AIMD calculations are usually done at several total energies to ensure the AIMD trajectories are walking through a large range of the configuration space. We use the Molpro program package [11] almost exclusively, and for the case of DFT methods we thereby obtain analytical gradients and also a dipole and quadrupole moment. Once we have an initial sample of geome-

tries, we then solve the electronic Schrödinger equation at those geometries using a high-level method and do a linear least-squares fit to determine the coefficients of the invariant basis functions. Hence we obtain the preliminary PES.

Step 2: Iterative improvement of a fit. In this step, we will work on the improvement of the initial fit, which is focus on three aspects. In the first place, we will search on the initial PES for stationary configurations, and additional configurations can then be obtained for example by applying random displacements of the stationary configurations. The *ab initio* energies at those new configurations will be calculated using the high-level method and added to the dataset. Furthermore, we always perform molecular dynamics calculations and/or diffusion Monte Carlo calculations of the ground state wave-function on the preliminary PES in order to find any badly-behaved regions on the PES due to the insufficient sampling. Additional configurations in the vicinity of such regions will also be added to the original dataset. Finally, we will remove near-duplicate configurations from the incremental of the dataset. A new fit is then done and the process proceeds iteratively until a satisfactory PES is obtained.

2.6. Summary

The approaches just mentioned have been used to obtain a number of PESs that are discussed in detail in this thesis, and Table 2.1 shows a summary of basis information about potential energy surfaces Further details can be found in the referred chapters as well as the cited references.

Table 2.1. A summary of a series of potential energy surfaces of which applications will be presented in this work.

Molecule	Maximum degree	Many-body expansion	# of total coefficients	# of *ab initio* energies	Chapter
$(H_2O)_2$ [12–14]	7	Yes	5 227	30 082	3
$(H_2O)_3$	5	Yes	2 008	12 540	3
3-body of $(H_2O)_3$	5	Yes	2 008	30 000	3
$H_4C_3O_2$ (Malonaldehyde)	4	Yes	1 633	11 147	6
H_5^+ [15]	5	Yes	352	105 888	7
CH_3	8	Yes	744	42 186	10
CH_3^+	8	Yes	744	17 812	10

Chapter 3.

Full-dimensional PES and DMS for Water

The central importance of water to life has made its study intense and widespread for many years. Experimental and theoretical molecular-based research has, not surprisingly, focused on various spectroscopic probes of water and water clusters. As with isolated molecules, the "game plan" for accurate computational modeling of large clusters of water monomers requires both accurate potentials and dynamical (or statistical mechanical) treatments of nuclear motion. Both aspects are focused on in this thesis. Specifically, in this chapter we report the development of *ab initio*, full-dimensional flexible, potentials that describe 1, 2- and 3-body interactions of water monomers. The nuclear dynamics is then focused on, by presenting anharmonic quantum calculations of intramolecular vibrational energies of the water dimer, trimer, hexamer and decamer in Chapter 8. The focus there will be on the local-mode model for the OH-stretches and a new local-monomer model that describes stretches and bends, and tests of both models.

After a brief introduction to the existed potentials for water, we will describe a step-by-step approach to establish an accurate model for water is to build up from the monomer to dimer to the trimer. In Section 3.2, we review dimer potentials that we will use to describe 1 and 2-body interactions of monomers. Following that, we present potentials of the water trimer based on two different *ab initio* methods. In the final section, the full-dimensional potential for water is then built up from a dimer potential and the intrinsic 3-body potential given the validity of many-body expansion of water potential.

3.1. Overview

There are numerous potentials for water. Most of these are for rigid-monomers with parameters that were determined by optimization with experimental properties, based largely on classical treatments of the nuclear motion. Examples of such properties include radial distribution functions, the heat of vaporization, the infrared (IR) spectrum, the self-diffusion constant, etc. The earliest of these potentials were simple point-charge models. More recently such models have been extended to include many-body polarization effects [16]. A review of many of these potentials can be found in the recent Frontiers Article by Szalewicz et al. [17] and also in a recent papers by Fanourgakis and Xantheas [18] and Jordan and co-workers [19].

The use of classical simulations to optimize model potentials is clearly motivated, if not necessitated, by the great difficulty in doing quantum simulations of dynamical and statistical properties. Nevertheless, there is now substantial evidence that quantum effects are significant for at least some properties of water. This is not surprising given the light H-atom mass. Thus, there has been substantial research

recently in developing approximate-quantum methods for the simulation of properties of water [20].

Clearly to fully describe the properties of water one needs to go beyond the rigid-monomer model and a review of such "flexible" potentials has been given in Ref. [18]. Of the various flexible potentials, arguably the ones developed by Xantheas and coworkers are the most realistic. The most widely used version is denoted TTM3-F [18], which stands for Thole-Type-Model (version 3)-Flexible. This potential is, like rigid-monomer ones, based on a physically-motivated form, i.e.

$$U = U_{mon} + U_{vdW} + U_{elec} + U_{ind}, \tag{3.1}$$

where U_{mon} is the sum of flexible, monomer potentials, U_{vdW} is the "van der Waals" interactions, given by a sum of two body terms

$$V_{vdW}(R_{ij}) = \sum_{i \in \text{``}O\text{''}} \sum_{i \neq j \in \text{``}O\text{''}} \frac{\varepsilon}{1 - 6/\lambda} \left\{ \frac{6}{\lambda} \exp\left(\lambda \left[1 - \frac{R_{ij}}{\sigma}\right]\right) - \left(\frac{\sigma}{R_{ij}}\right)^6 \right\}, \tag{3.2}$$

and electrostatic and induced interactions are given by electrostatic and polarization terms

$$U_{\text{elec}} + U_{\text{ind}} = \sum_i \sum_{i<j} \frac{q_i q_j}{4\pi\epsilon_0} \Phi^f(r_{ij}) - \frac{1}{2} \sum_i \sum_{j \neq i} \mathbf{D}_i \bullet \mathbf{E}_{ij} \tag{3.3}$$

where the terms are self-explanatory. The parameters appearing in these expressions (but not the monomer potential) were determined by fitting to limited *ab initio* energies and empirical optimization. For more details see Ref. [18] and references cited therein. The main purpose in showing these equations is to contrast them with the strictly numerical approach we have taken and which we describe in the next section.

Since the TTM3-F potential is quite simple in form and well-grounded in both the physical form and optimization, it is widely used, notably recently in approximate-quantum calculations of the IR and Raman spectra of water [20, 21]. Recently, there have been a number of tests of this potential, including by us, and we give those below along with some new ones. Earlier Bukowski et al. pointed out large errors for the vibration-rotation tunneling splittings of the water dimer using a rigid-monomer version of the TTM3-F potential, indicating that the H-bond rearrangement barriers for the dimer are not accurately given by this potential.

The alternative to an empirical or semi-empirical potential is a fully *ab initio* one. This is of course a daunting task, as emphasized recently by Szalewicz et al. [17], even if one can be based on two and three-body interactions. As these authors noted, by making the rigid- monomer approximation, the task is greatly simplified, and indeed an accurate *ab initio*-based rigid-monomer water potential has been reported by Szalewicz and van der Avoird and co-workers[22–25]. This potential, termed "CC-pol", is based on fitting *ab initio* energies for the dimer and including polarization interactions as well as a three-body interaction obtained using symmetry-adapted perturbation theory. We do not review this potential in detail here because it has been reviewed very recently [17], and secondly because it is for rigid-monomers, and our focus is on flexible potentials.

3.2. The Water Dimer $(H_2O)_2$

Three generations of the dimer potential now exist. The second generation potential, denoted HBB1 [13], is a fit to a larger data set of CCSD(T)/aug-cc-pVTZ energies and was used in quantum calculations of the vibration-rotation tunneling splittings of $(H_2O)_2$ [13, 26] and $(D_2O)_2$ [13]. The results are in excellent agreement with ex-

periment [27, 28] and this is an indication of the accuracy of the barriers to H-bond isomerizations for HBB1. The flexible HBB1 potential was used very recently in new calculations of the vibration-rotation tunneling splittings and the vibrational energies of the OH-stretches by Leforestier et al. [26]. They reported a significant improvement in one particular tunneling splitting, which was ascribed to the importance of flexibility of this potential.

Leforestier et al. also noted that the D_e for the water dimer is underestimated slightly by HBB1. This was noted by us previously [12] and ascribed to the well known basis set superposition error (BSSE) in the dimer [12, 29, 30] water clusters [31]. An effective correction to BSSE was implemented in the latest version of the HBB potential, denoted HBB2 [14]. This potential has a highly accurate D_e of 4.98 kcal/mol and is currently the most accurate flexible dimer potential.

3.2.1. Invariant polynomial basis

All three dimer potentials employed the same fitting procedure in terms of permutationally invariant polynomials in the Morse variables. The representation in terms of primary and secondary invariant given in Equation 2.4a were generally good; however, some regions where nuclei are close together were not well behaved and so another form for the fit was developed that is much better behaved in these regions. It is given by

$$V = p(\mathbf{x}) + \sum_{i<j} q_{ij}(x) y_{ij}. \tag{3.4}$$

where $p(\mathbf{x})$ is the main polynomial in terms of the 15 Morse variables $x_{ij} = \exp(-r_{ij}/3)$, similar to what is given in Equation 2.4a, and $q_{ij}(x)$ are the two-body short-range polynomials, corresponding to the HH, HO, and OO pairs, in terms of $y_{ij} = \exp(-r_{ij})/r_{ij}$,

and r_{ij} is the internuclear distance between the ith and j^{th} atom. The polynomial p is of total degree 7 and q is a quartic/cubic?. The expansion coefficients are determined by a weighted least squares fit to the ab initio data, and the weight of a data point with energy E relative to the global minimum was $(E_0/(E_0+E))^2$ with E_0 set to 0.01 hartree. In total, there are 5 227 terms in the expression for the PES.

3.2.2. Sampling and ab initio calculations

The first generation of the dimer potential, HBB0 [12], is a fit to roughly 20 000 *ab initio* energies, obtained at the CCSD(T) level of theory with an aug-cc-pVTZ basis. The configuration of these 20 000 data was described briefly as follows. First, fourteen OO distances were selected from 4 to 100 bohr, with eight distances between 4 and 6 bohr, four between 8 and 15 bohr, and finally one at 50 bohr and one at 100 bohr. At each OO distance, between 300 and 2000 monomer geometries were selected for a total of 15 000 configurations. Roughly 3 000 additional data points were generated at configurations where the energy is less than 2 000 cm^{-1} (relative to the minimum on the fit) and then 1 800 additional energies were done to yield a PES that gave a stable quantum diffusion Monte Carlo (DMC) zero-point energy (ZPE) in full dimensionality. The final data set for this previous PES consisted of 19 805 energies.

In the second generation, HBB1, an additional 10 227 configurations were incorporated to improve the description of the potential at energies below 10 000 cm^{-1}. These additional energies were selected from a large set of geometries generated in vibrational configuration interaction and DMC calculations. The distribution of these energies is nearly uniform in the range of 0-10 000 cm^{-1}. The final enlarged data set includes 30 082 configurations.

Given the relatively weak binding of the water dimer basis-set- superposition-error (BSSE) is a concern. This was approximately corrected by the standard counterpoise (CP) method[32] at each geometry for both HBB0 and HBB1. Although the BSSE of both PESs has been roughly counted by the CP correction, D_e for these PESs equals 19.9 kJ/mol (4.76 kcal/mol), which is below the benchmark value of 20.99±0.34 kJ/mol [30]. Thus, we developed the third generation HBB2 that gives the correct D_e.

In principle to obtain a PES with the benchmark value of D_e a fit should be done to the benchmark electronic energies. However, owing to the prohibitive cost in computer time to do that (at least for us) we proceeded in a practical way by fitting a slightly modified set of electronic energies given by

$$E' = E_{\mathrm{UC}} + \alpha(E_{\mathrm{CP}} - E_{\mathrm{UC}}) \tag{3.5}$$

where E_{UC} are the uncorrected electronic energies and E_{CP} are the counterpoise corrected ones and where α is adjusted to give the benchmark D_e (in the present case, $\alpha = 0.52$. We note that the CP correction is zero in the separated monomer limit (because in that limit the basis-set superposition error is zero) so it was trivial to determine α by simply comparing the two energies at the global minimum. Doing this we determined α and Equation 3.5 was applied to the enlarged data set of 30 000 electronic energies. HBB2 was then fit to these 30 000 new energies E' distributed as described above. We do note that D_e for HBB2 equals 20.8 kJ/mol (4.98 kcal/mol) in excellent agreement with the benchmark value [30].

The fitting rms error of HBB1 and HBB2 are virtually identical. Broadly speaking, the fitting error is 11.7 cm^{-1} for configurations with energies below 10 000 cm^{-1}, 25.4 cm^{-1} for energies between 10 000 and 20 000 cm^{-1}, and 83.0 cm^{-1} for energies ranging from 20 000 to 40 000 cm^{-1}.

3.2.3. Dipole moment surface

The dipole moment was calculated at the MP2/aug-cc-pVTZ level at the same set of grid points used for the energies. The fit was done as described in detail previously in Chapter 2. Total fitting rms errors of the DMS using the enlarged data set along x-, y-, and z-dipole components are 0.016, 0.009, and 0.009 a.u., respectively. Comparing to the early version of DMS using the smaller set of data, the fitting accuracy is improved by 20%. The DMS dissociates correctly to the monomer DMS. The values of the MP2-based DMS at the $(H_2O)_2$ global minimum and the H_2O monomer equilibrium geometry are 1.02 and 0.729 a.u., respectively, slightly smaller than the benchmark values of 1.06 and 0.757 a.u. of Tschumper *et al.* [30]

3.3. The Water Trimer $(H_2O)_3$

3.3.1. ACPF-based trimer PES

This early version of trimer PES is a fit to $36\,992$ *ab initio* energies obtained using the averaged coupled-fair functional (ACPF) method [33, 34] using the Dunning cc-pVTZ basis [35] as implemented in the MOLPRO code suite [11]. The energies are for a scattered set of configurations described below. As in our previous work, this trimer PES is represented as an expansion in functions of the complete set of internuclear distances. The basis for the least-squares approximation is made up of permutation-ally invariant polynomials of Morse-like functions, $y(i,j) = \exp(-r(i,j)/\lambda)$, where λ was fixed at 1.6 bohr and $r(i,j)$ is the internuclear distance of atoms i and j. In this application we used a many-body expansion containing 2-atom, 3-atom and 4-atom terms in variables $y(i,j)$ plus a single polynomial of, in principle, all transformed internuclear distances. The polynomials for the various 2-atom terms (H-H, H-O and

O-O) are of maximum degree 8, those for the 3-atom terms of maximum degree 7, those of the 4-atom terms of maximum degree 5, and the global term is of maximum degree 5. The total number of free coefficients in the expansion is $2\,008$. We use the complete molecular symmetry group, of degree 6!3! ($=4\,320$), to define the space of invariant polynomials, and as in our earlier work the MAGMA computer algebra system [9, 10] was employed to help generate the basis.

The sampling of the configuration space and the construction of the PES were done iteratively, alternating between molecular dynamics calculations on a tentative PES, sampling from those trajectories, calculating further *ab initio* energies, and creating a new surface. These molecular dynamics calculations were done at a wide range of energies, from about 0.01 hartree up to 0.2 hartree and more. For this sampling purpose it was helpful to add an artificial term to the fitted potential at large distances to induce reflection and prevent complete break-up. The low-energy sampling runs ensure good coverage of the region of configuration space near the global minimum (the ring-like structures) whereas the high-energy runs are aimed at good global coverage.

The PES is a weighted least squares fit to the *ab initio* energies, where the weight of energy $E(i)$ is given by $w(i) = d/(d + E(i) - E_{\min})$ in which $E_{\min}$ is the global minimum energy and $d = 0.1$ hartree. Relative to the global minimum $12\,153$ energies are less than 0.1 hartree (2.72 eV), $17\,745$ are between 0.1 and 0.2 hartree, and the remainder are above 0.2 (5.44 eV) hartree. Two fits to these data were done and for the one we focus on here the rms error for the subset of configurations with energy less than 0.1 hartree is 8.5e-4 hartree (0.023 eV). A lower order, and hence more efficient, fit was also done for use in testing convergence of vibrational calculations, which are described next. This other PES has an rms fitting error of 1.5e-3 hartree but has roughly half the number of terms as the PES we report here.

The dipole moment was also calculated and fit in a permutationally invariant manner similar to the one for the above dimer surface. We represent it as the dipole due to a system of effective charges at the positions of the nuclei. These effective charges are scalar functions of the configuration and are covariant under the molecular permutation symmetry group. We employ a many-body expansion truncated at the 4-atom level, based on polynomials of the same variables, the $y(i,j)$, used for the PES. The maximum polynomial degree is 8 for the 2-atom terms, 7 for the 3-atom terms, and 5 for the 4-atom terms. There are $1\,889$ free coefficients in this expansion.

3.3.2. MP2-based trimer PES

This MP2-based PES for the water trimer is a fit to $12\,540$ *ab initio* energies obtained using MP2 method with the aug-cc-pVTZ basis as implemented in the MOLPRO package.[11] Among the full set of configurations for the *ab initio* calculations, $10\,540$ configurations are concentrated near the global minimum, and the rest $2\,000$ configurations are from the fragment configuration space, namely an monomer fragment and an dimer fragment placed far apart. As one can see in the energy distribution of the data set shown in Figure 3.1, we paid much of our attention to those regions no so high in energy. Most of the energies are below 600 kJ/mol relative to the global minimum. As in our previous work, the new trimer PES is represented as a linear combination of functions of the complete set of internuclear distances. The basis for the least-squares approximation is made up of permutationally invariant polynomials of Morse-like functions: $y(i,j) = \exp(-r(i,j)/\lambda)$ where λ was fixed at 2.0 bohr and $r(i,j)$ is the internuclear distance of atoms i and j. Except for the value of λ, we used the same polynomial basis here as for the ACPF-based trimer PES, and we refer to Section 3.3.1 for the remaining technical details on fitting.
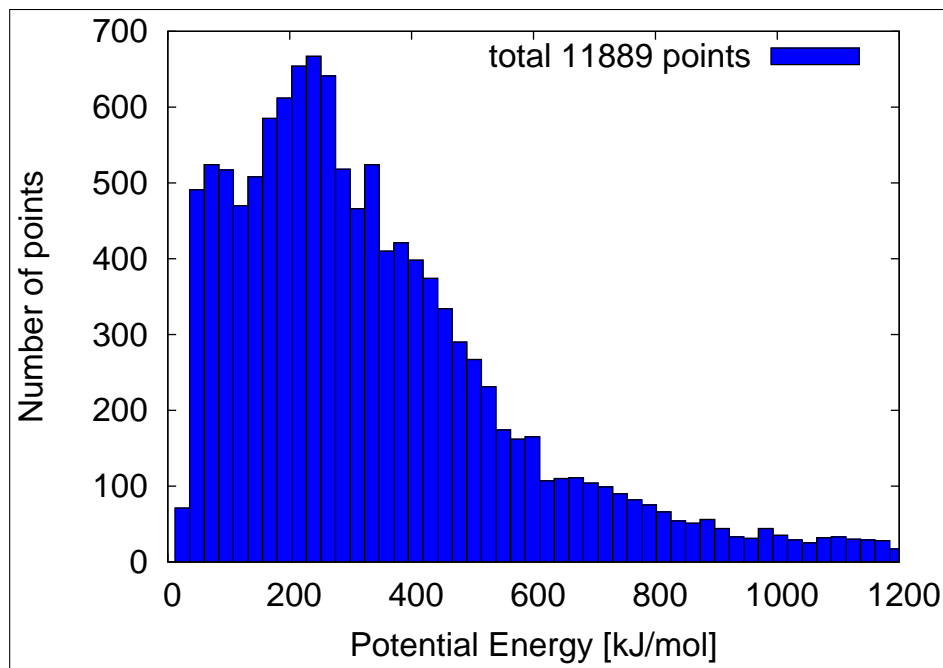
Figure 3.1. Distribution of *ab initio* energies vs the energy in units of kJ/mol relative to the global minimum below 1 200 kJ/mol. An additional 651 energies above 1 200 kJ/mol were included in the fit.

The RMS fitting error is 1.7 kJ/mol for the subset of 5 716 configurations with energy below 262 kJ/mol measured from the global minimum. For 4 245 energies between 262 to 525 kJ/mol, the RMS error rises to 3.9 kJ/mol and 8.1 kJ/mol for 2 037 energies ranging from 525 to 1 313 kJ/mol.

The dipole moment was also calculated at the same level of theory at the same set of configurations and fitted in a permutationally invariant manner exactly the same as the ACPF-based trimer DMS describe in Section 3.3.1.

3.4. Water Clusters $(H_2O)_n$

3.4.1. Many-body expansion

As noted already, the *ab initio* potential we have developed is based on 2-body and 3-body potentials and so it is important to review the evidence that this representation is accurate for large water clusters. Fortunately, there have been a number of careful studies of the mangy-body decomposition of the electronic energies for a variety of water clusters. In particular, there have been several independent *ab initio* analyses for the water hexamer [17, 19, 36, 37]. These have determined that the energy is dominated by 2-body terms (almost 80% of the energy) with intrinsic 3-body terms accounting for roughly 20% of the total energy and 4- and higher-body interactions being essentially negligible, i.e., of the order of 1%.

3.4.2. The intrinsic three-body potential

The three-body potential, denoted $V_{\text{3-body}}$, is defined as

$$V_{\text{3-body}}(1,2,3) = V_{\text{trimer}}(1,2,3) - V_{\text{dimer}}(1,2) - V_{\text{dimer}}(1,3) - V_{\text{dimer}}(2,3)$$
$$+ V_{\text{monomer}}(1) + V_{\text{monomer}}(2) + V_{\text{monomer}}(3), \quad (3.6)$$

where 1, 2, and 3 denote the collective Cartesian coordinates of monomer i, V_{trimer} is the electronic energy of three monomers at a given configuration, and V_{dimer} and V_{monomer} are the three dimer and monomer electronic energies, respectively. Each of these electronic energies was obtained using second order Møller-Plesset perturbation theory MP2 and the avtz basis set MP2/avtz.
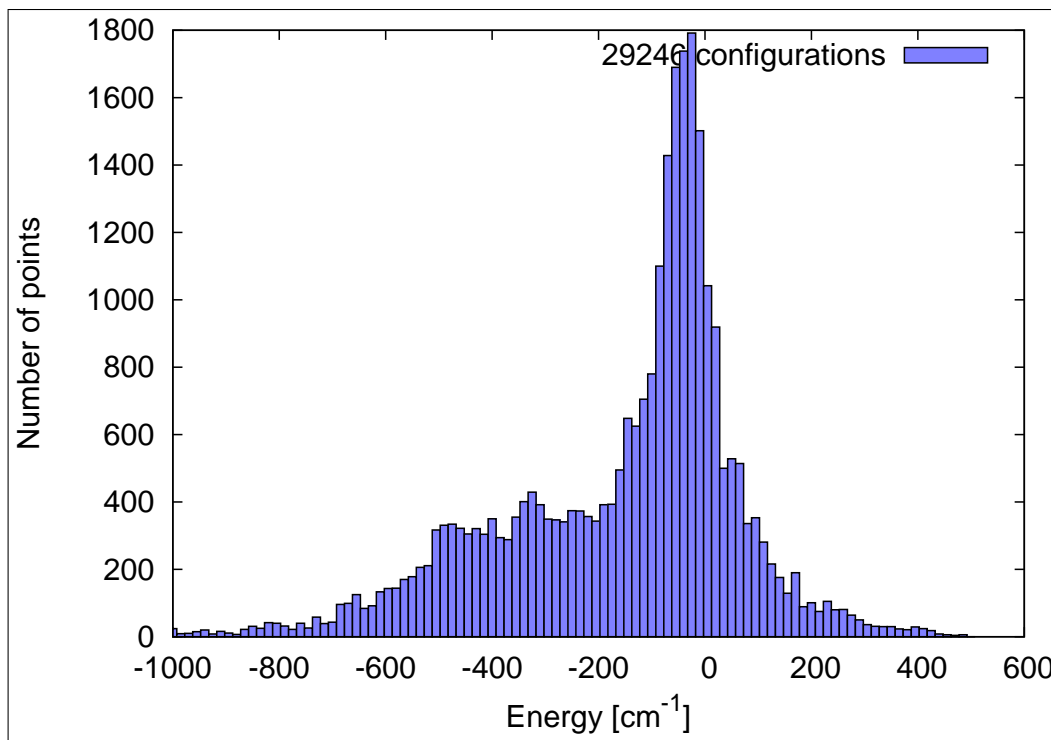
Figure 3.2. Distribution of the electronic three-body energies vs the energy in cm^{-1}.

The database of electronic energies consists of roughly 30 000 intrinsic three-body electronic energies. Roughly 6 000 configurations were concentrated in the region of the global minimum and stationary points of the water trimer as well as the fragment region of the dimer plus monomer. 21 000 three-body configurations were obtained from MP2/aug-cc-pVDZ direct-dynamics calculations of the water hexamer. The last minor portion of the data set of about 3 000 structures was selected from RHF/6-31G(d,p) optimized equilibrium geometries of water clusters $(H_2O)_n$, $n = 4-20$ taken from previous work [38].

Plots of the distribution of three-body energies, OO distances, and OOO angles are given in Figure 3.2-3.3, respectively. As seen the energies are concentrated in the range from -800 to 400 cm^{-1} and the OO distances in the range of 2-7 Å. This range of OO distances and energies is a reflection of where the three-body interaction is of greatest relevance to the overall water potential. This is essentially a result of
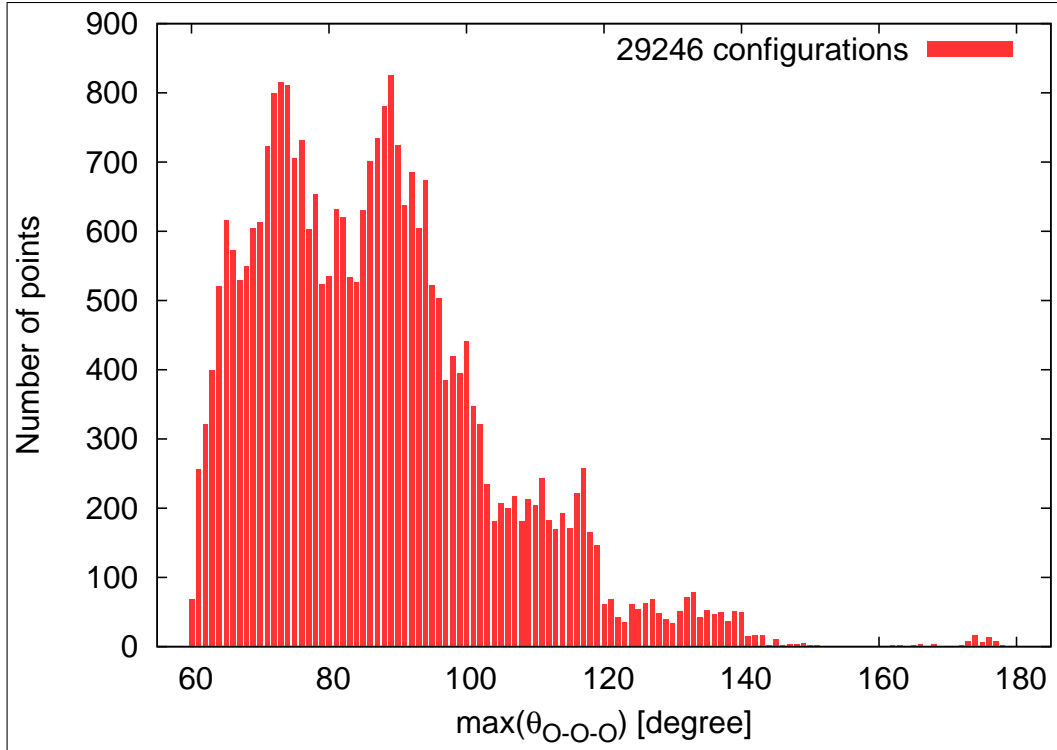
Figure 3.3. Distribution of the maximum OOO angle for the three H_2O monomers over configurations for the calculation of the three-body energies.

the dominance of the two-body potential, which has already been noted and will be shown explicitly in Figure reffig:water-23b-cuts.

The three-body electronic energies were fitted using methods developed in our group that use permutationally invariant polynomials that are functions of all the internuclear distances, $r(i, j)$, transformed to Morse variables, $y(i, j) = \exp(-r(i, j)/\lambda)$, in a manner that is invariant under the complete molecular permutation symmetry group, which in the present case is of the size 6!3!=4320. The value of the Morse variable range parameter λ was taken as 2.0 bohr. Our experience with fitting roughly 20 potentials indicates that the precision of the fits is largely insensitive to the precise value of λ provided it is in the range of 1.5-3 bohr; a typical value is 2.0 bohr, which is the choice here. In the present demanding application, the representation is a sum of two-atom, three-atom, four-atom, and one full nine-atom terms, with all
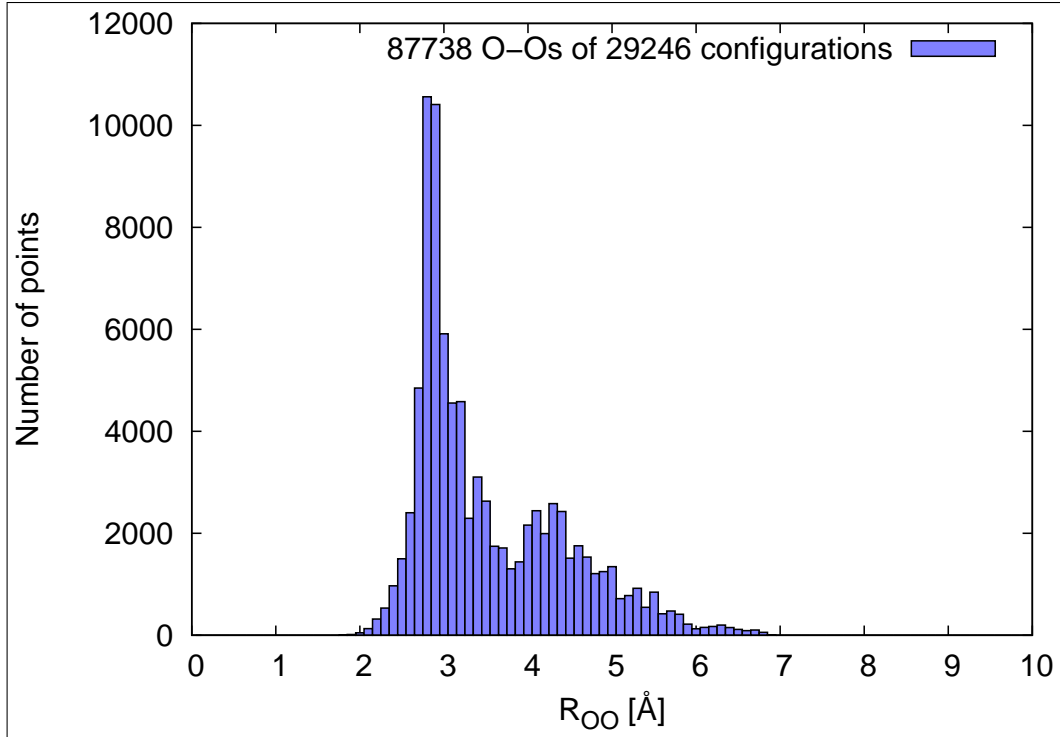
Figure 3.4. Distribution of OO distances for the three H_2O monomer configurations for the calculation of the three-body energies.

free coefficients fitted simultaneously in a standard least-squares optimization. There are three two-atom terms, corresponding to HH, HO, and OO pairs, four three-atom terms (HHH, HHO, HOO, and OOO), four fouratom terms (HHHH, HHHO, HHOO, HOOO) and a single nine-atom term. Each term is of the form of a polynomial in Morse variables $p(y)$ multiplied by a damping function of the internuclear distances, which enforces the physical boundary condition that $V_{3\text{-body}}$ vanishes as any monomer is removed from the trimer configuration. The polynomial $p(y)$ is a function of $k(k-1)/2$ variables for the k-atom terms and is expanded on a basis of permutationally invariant polynomials following procedures of computational invariant theory and the MAGMA computer algebra system [9,10]. The damping function
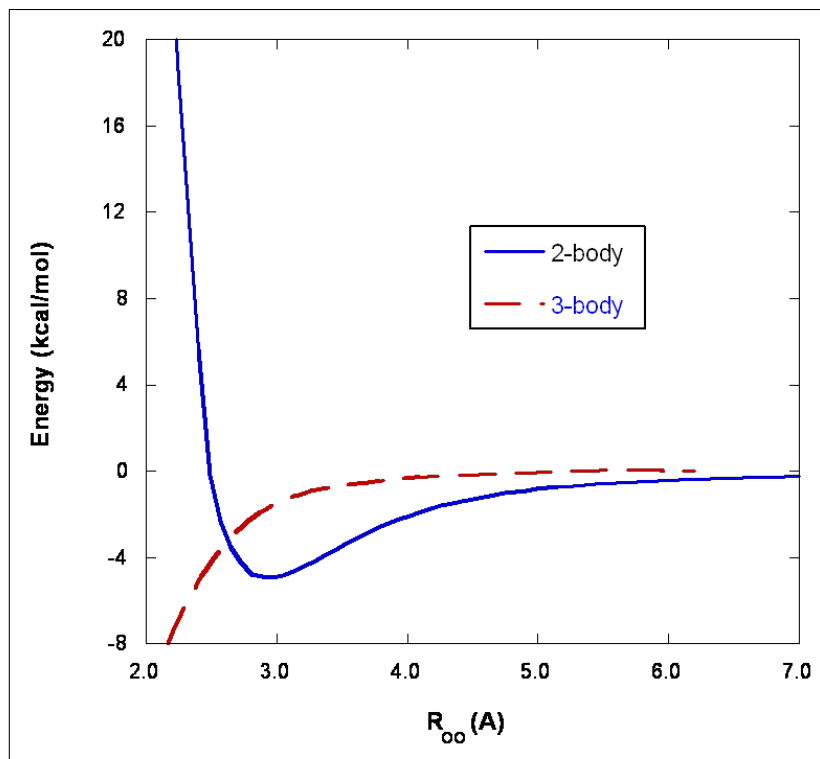
Figure 3.5. Potential cuts of two- and three-body potentials of water as a function of the OO distance. For the two-body potential the cut is from the HBB2 potential for fixed monomer geometries corresponding to the dimer global minimum. The three-body potential cut is for the removal of one monomer of the water trimer at a fixed orientation and geometry corresponding to the trimer global minimum.

$g(\mathbf{r})$ is expressed in terms of s,

$$s = \left(\frac{2}{k(k-1)} \sum_{i<j} r(i,j)^2 \right)^{\frac{1}{2}}, \tag{3.7}$$

the root mean square internuclear distance within the is given by $g(\mathbf{r}) = (\max(0,\ 1 - s/a))^3$ and the parameter a equals 8.0 bohrs for the two-, three-, four-, and nine-atom terms. The least-squares system has $2\,008$ unknowns (and thus the fit has a very modest $2\,008$ terms) and the rms fitting error over the entire data set is 24 cm^{-1}.

Figure 3.5 shows plots of one-dimensional cuts, described in detail in the caption, of the two-body dimer and intrinsic three-body potentials as a function of the OO

distance. As seen, the former accounts for the major monomer-monomer binding and the latter effectively adds binding over the range of OO shown. The three-body cut is clearly shorter range than the two-body one as expected. Also at OO distances shorter than 2.5 Å the two-body potential is highly repulsive and much larger in magnitude than the three-body potential. Thus from this plot it is clear that the range of the three-body potential of relevance to energies of interest for a water potential is roughly 2.5-6.0 Å. As expected from simple electrostatic arguments, the long-range behavior of the two- and three-body potentials is $\mathcal{O}(R^{-3})$ and $\mathcal{O}(R^{-6})$, respectively.

3.4.3. Water PES and DMS

With the monomer, two- and three-body potentials in hand, the general water potential can be expressed as the sum of one- and two-body potentials and, more accurately, by that sum plus the three-body potential. As usual we assume that the identity of monomers is unambiguous. These potentials, PES(1,2) and PES(1,2,3), are given, respectively by

$$\text{PES}(1,2) = \sum_{i=1}^{N} V_{\text{monomer}}(i) + \sum_{i<j}^{N} V_{\text{2-body}}(i,j), \qquad (3.8)$$

and

$$\text{PES}(1,2,3) = \sum_{i=1}^{N} V_{\text{monomer}}(i) + \sum_{i<j}^{N} V_{\text{2-body}}(i,j) + \sum_{i<j<k}^{N} V_{\text{3-body}}(i,j,k), \qquad (3.9)$$

where N is the number of monomers.

In a similar fashion, a flexible DMS for N-water clusters with only one- and two-body interactions can be constructed from the flexible DMS of the water dimer.

Conceptually, DMS(1,2) can be expressed as

$$\text{DMS}(1,2) = \sum_{i=1}^{N} \vec{\mu}_{\text{monomer}}(i) + \sum_{i<j}^{N} \vec{\mu}_{2\text{-}body}(i,j), \qquad (3.10)$$

where $\vec{\mu}_{\text{monomer}}$ denotes the separated monomer dipole moment, and $\vec{\mu}_{2\text{-}body}$ represents the intrinsic two-body dipole moment. However, as seen in Chapter 2 due to the vector property of the dipole moment we need to have a slight different expression for the dipole in terms of the invariant polynomials, where the dipole moment is a product of effective charges located at the atomic positions and Cartesian coordinates. Therefore, the many-body dipole moment is actually a product of many-body effective charges and Cartesian coordinates.

Here we test the predictive accuracy of the one- and two-body DMSs, denoted DMS(1) and DMS(1,2), respectively. The accuracy of each representation is tested for the water hexamer at the minimum of the prism configuration by comparisons with calculations of the dipole moment at the LCCSD(T)/haVTZ optimized geometry using both MP2/aVTZ and LCCSD(T)/haVTZ calculations (the LCCSD(T) dipole moment was obtained using the finite difference approximation). In addition the MP2/aVTZ dipole moment was decomposed into one-body and two-body contributions. The results of these dipole moment calculations are given in Table 3.1. Thus the flexible DMS(1,2) is very accurate for this test. Using DMS(1) produces results that are of good although less accuracy than the results shown here for DMS(1,2).

3.5. Tests

In order to assess the accuracy of the potentials for water clusters, we present below test results of the water dimer, trimer, and hexamer, including the energy minimiza-

Table 3.1. Dipole moment components of the water hexamer prism minimum (atomic units).

MP2/aVTZ			LCCSD(T)/haVTZ	DMS	
Full	1-body	1,2-body	Full	1-body	1,2-body
-0.921	-0.827	-0.94	-0.921	-0.826	-0.949
0.422	0.409	0.428	0.422	0.409	0.425
0.147	0.117	0.155	0.147	0.12	0.141

tion of various stationary points as well as their energies and harmonic frequencies. Good agreement with benchmark calculations has been found for the potentials mentioned above. Further analysis along with results of vibrational calculations will be present in Chapter 8.

3.5.1. Structures and energetics
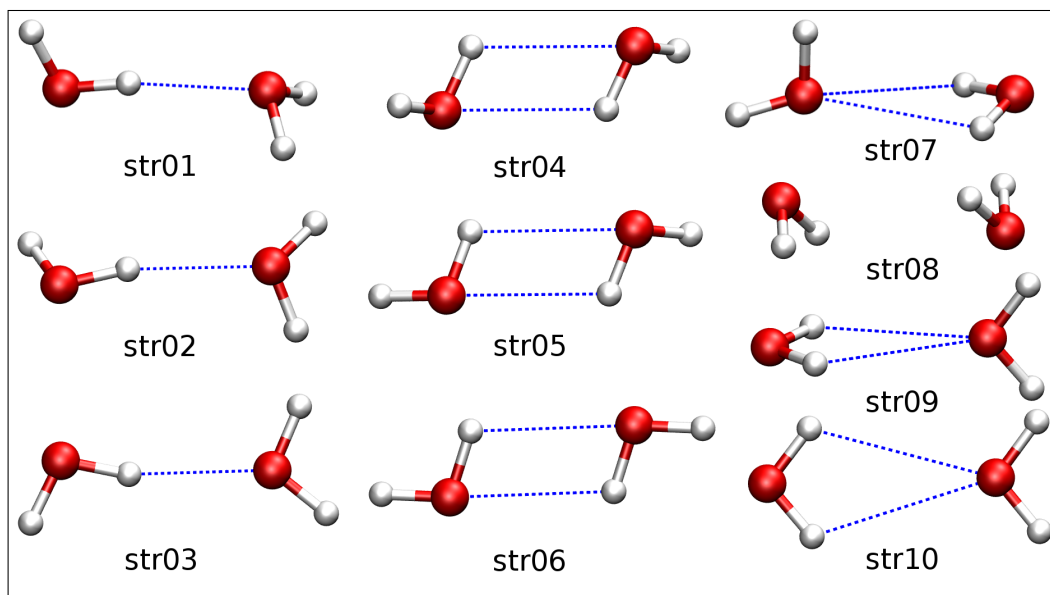
Figure 3.6. Low-lying stationary point structures of the water dimer. str01 is the global minimum.

Ten low-lying stationary points were located on HBB1 and HBB2. The geometries of the HHB2 stationary points are virtually identical to those of HBB1; these
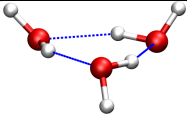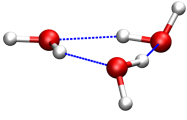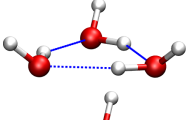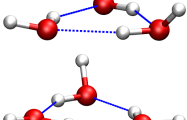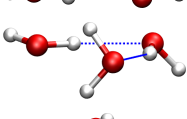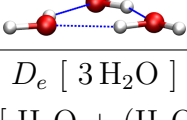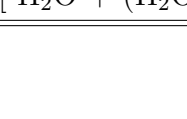
are shown in Figure. The energies of these stationary points, relative to the global minimum, as well as their counterparts on HBB1, are presented in Table 3.2. The energies of HBB2 are 4-8% higher than those of HBB1 except for stationary point 2 where the difference is 13%.

Table 3.2. Relative energies (cm^{-1}) of ten stationary points on indicated PES, ordering as indicated in Figure 3.6.

Stationary point No.	Symmetry	HBB1	HBB2
1(Global minimum)	C_s	0.0	0.0
2	C_1	164.1	185.3
3	C_s	196.7	210.2
4	C_i	244.7	260.7
5	C_2	328.6	354.4
6	C_{2h}	347.0	375.5
7	C_s	601.4	640.9
8	C_{2h}	1176.4	1230.4
9	C_{2v}	588.9	629.2
10	C_{2v}	897.1	946.1

The second test of these potentials is to the water trimer. Table 3.3 shows a comparison of the PES energies of the global minimum, which has the three free OH moieties in the "up-up-down" conformation denoted "uud", a higher energy local minimum, denoted "uuu", and five additional configurations which all correspond to saddle points. The electronic dissociation energies De to the fragments indicated are also compared with benchmark single-point CCSD(T) calculations with an extrapolation to the complete basis set (CBS) limit [39]. Very good agreement is seen with the benchmark results for both PESs for the relative energies; however, for the D_e values PES(1,2,3) is clearly superior to PES(1,2); this is a direct indication of the additional binding due to the three-body potential.

Table 3.3. Energies (kcal/mol) of six low-lying stationary points of the water trimer and D_e.

Structure	PES(1,2)	PES(1,2,3)	CCSD(T)/CBS[a]
	0	0	0
	0.22	0.29	0.23
	0.7	0.82	0.76
	0.72	0.86	0.77
	0.78	0.99	0.78
	1.58	2.16	2.15
	1.11	1.47	1.25
D_e [$3\,H_2O$]	13.67	15.72	15.79
D_e [$H_2O + (H_2O)_2$]	8.69	10.74	10.79

[a] Ref. [39]

To further test the predictive accuracy of the present PESs a larger cluster must be considered; however, one where benchmark *ab initio* calculations are still feasible. For this purpose the water hexamer is a good choice. The hexamer has been termed the smallest drop of water or ice [40–42], owing to its fully three-dimensional structure with some isomers exhibiting two ringlike structures held together by H-bonds. There are numerous energetically low-lying isomers of the hexamer and recent calculations now point to the prism form (shown in Figure 3.7) as being the lowest energy isomer [37, 43, 44]. Dahlke et al. [37] performed MP2/haVTZ geometry optimizations and single-point CCSD(T)/haVTZ energy calculations at six MP2/haVTZ optimized minima, without correction for BSSE. Subsequently Bates and Tschumper [43] reported CCSD(T)/CBS energies at these geometries and for two additional isomers
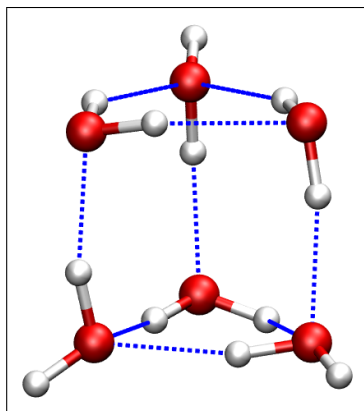
Figure 3.7. Global minimum of the water hexamer cluster.

related to the "book" and "boat" isomers. Santra et al. [44] reported diffusion Monte Carlo calculations of several isomers of the hexamer as well as the electronic dissociation energies. Harmonic zero-point energies for these isomers were also reported using density functional [37] and MP2/haVTZ [43] calculations; however, mode frequencies were not reported. So the comparison of the electronic dissociation energy to all monomers reported with these benchmark calculations shown in Table 3.4, clearly shows the high accuracy of PES(1,2,3) for this important property.

Table 3.4. Dissociation energy (D_e) of the water hexamer prism.

Source	D_e (kcal/mol)
PES(1,2)	39.5
PES(1,2,3)	45.8
CCSD(T)/CBS[a]	45.9
DMC[b]	45.9

[a] Ref. [45]; [b] Ref. [46].

3.5.2. Harmonic frequencies

The next sets of tests we consider are the normal mode analysis of the water dimer, trimer and hexamer. Table 3.5 contains these results for the dimer (see Figure 3.6

for the structure of the minimum) using a variety of *ab initio* methods and basis sets along with results from HBB2. The results there serve two purposes. One is to examine the accuracy of the local-coupled-cluster method (LCCSD(T))[45], which is much more efficient than the conventional coupled-cluster method and which will be applied to the hexamer. In addition to being more efficient, it has been shown that LCCSD(T) is largely free of BSSE, as demonstrated for small water clusters[47]. For the basis sets employed for the results in Table 3.5 BSSE is fairly small, nevertheless the standard counterpoise (CP) correction [32] was applied to the CCSD(T)/aVTZ results. As seen, there is very good agreement for all *ab initio* results, indicating that LCCSD(T) is reliable and accurate for the dimer. Second we see that HBB2 yields very accurate results for all frequencies.

Table 3.5. Harmonic frequencies (cm^{-1}) of the water dimer global minimum from indicated sources.

Mode	CP-CCSD(T)/ aVTZ	LCCSD(T)/ aVTZ	CCSD(T)/ aVQZ	LCCSD(T)/ aVQZ	HBB2 $\equiv$ PES(1,2)
1	125	117	130	119	126
2	141	139	146	138	141
3	146	143	152	152	149
4	179	167	186	179	181
5	345	325	354	334	351
6	600	577	619	592	610
7	1646	1651	1651	1654	1653
8	1666	1666	1671	1670	1673
9	3737	3745	3748	3765	3757
10	3806	3805	3825	3825	3827
11	3892	3896	3912	3912	3915
12	3912	3910	3931	3931	3934

Next consider the analogous study for the water trimer (the cyclic up-down-up global minimum), which contains the effect of 3-body interactions. These are shown

in Table 3.6, where we focus on the intramolecular modes. Again there is very good agreement between the CP-CCSD(T)/aVTZ and LCCSD(T)/aVTZ results, with the latter being slightly high relative to the former for the stretch modes. The results from PES(1,2,3) are also in very good agreement with the CP-CCSD(T)/aVTZ ones. Note, as with the dimer, the largest variation among results is for the H-bonded OH-stretches, which are very sensitive to geometry.

Table 3.6. Global minimum trimer harmonic frequencies (cm^{-1}) from indicated sources.

Mode	CP-CCSD(T)/ aVTZ	LCCSD(T)/ aVTZ	LCCSD(T)/ aVQZ	PES(1,2)	PES(1,2,3)
bend-1	1657	1657	1659	1653	1659
bend-2	1659	1660	1662	1657	1663
bend-3	1680	1680	1684	1674	1687
OH-1	3623	3660	3664	3721	3629
OH-2	3674	3700	3709	3738	3658
OH-3	3682	3707	3716	3745	3667
OH-4	3885	3891	3903	3889	3880
OH-5	3889	3894	3906	3893	3886
OH-6	3889	3895	3908	3894	3888

The frequencies of the lowest energy prism form of the water hexamer, depicted in Figure 3.7, are shown in Table 3.7. This cluster is already too large for us to perform CCSD(T)/aVTZ calculations and indeed such calculations have not been reported in the literature. We have done CCSD(T)/aVDZ and CP-CCSD(T)/aVDZ calculations and will report those results elsewhere; however, larger basis sets are beyond our computational resources and so we present LCCSD(T)/haVTZ results in this table as the benchmark values. We compare frequencies obtained with MP2/haVTZ method/basis by Bates and Tschumper[43] and from Density Functional Theory with the M06-2x functional and MG3S basis of Truhlar and coworkers [37]. Results from the 1,2,3-body potential PES(1,2,3) and PES(1,2) 1,2-body potential (HBB2) are also

given. Focusing first on the H-bonded OH stretches, we see that the MP2/haVTZ frequencies are roughly 40-200 cm^{-1} below the LCCSD(T)/haVTZ ones. The DFT results are generally more accurate than the MP2 ones with the glaring exception of the lowest frequency OH-stretch, which is low by roughly 230 cm^{-1}. PES(1,2) and PES(1,2,3) frequencies are much closer to the LCCSD(T) ones, especially for the strongly H-bonded OH-stretches. There are some variations in the comparisons for the H-bonded stretches that may be traceable to some overestimation of these stretches in the local method that were seen for the water trimer in Table 3.6.

Table 3.7. Hexamer prism intramolecular harmonic frequencies (cm^{-1}) from indicated sources.

Mode	DFT[a]	MP2[b]	PES(1,2)	PES(1,2,3)	LCCSD(T)
bend-1	1632	1644	1652	1661	1667
bend-2	1642	1656	1660	1674	1674
bend-3	1654	1664	1671	1683	1683
bend-4	1672	1681	1699	1687	1693
bend-5	1706	1696	1708	1736	1708
bend-6	1721	1715	1717	1751	1723
OH-1	3184	3205	3678	3444	3413
OH-2	3506	3452	3695	3524	3572
OH-3	3623	3549	3715	3608	3647
OH-4	3641	3573	3733	3613	3658
OH-5	3769	3688	3748	3636	3729
OH-6	3778	3705	3761	3692	3747
OH-7	3816	3769	3801	3735	3801
OH-8	3841	3785	3817	3768	3815
OH-9	3859	3811	3836	3817	3830
OH-10	3950	3890	3878	3826	3879
OH-11	3954	3893	3883	3853	3880
OH-12	3956	3895	3891	3871	3883

[a] Ref. [37]; [b] Ref. [43].

Part II.

Full-dimensional Quantum

Approaches

Chapter 4.

Diffusion Monte Carlo

In the next two chapters, we will introduce two full-dimensional quantum approaches that we've been using extensively to solve the time-independent nuclear Schrödinger equation. Both techniques are designed to provide numerically "exact" solutions efficiently on an accurate full-dimensional *ab initio* potential energy surface. The accuracy of the results as well as the efficiency depend largely on the quality of the potential energy surface (PES) used. One such method, named "Diffusion Monte Carlo (DMC)", employs Monte Carlo simulation of diffusion/stochastic process in imaginary time to approach the solution to the time independent Schrödinger equation. It was first used by Anderson[48, 49] to perform electronic-structure calculations of small molecules such as H_3^+, before being widely applied to solve the nuclear motion. In our research, the DMC calculation has been largely used to obtain the properties of the ground vibrational state, e.g. the zero-point energy (ZPE) as well as the ground state wave-function, and the vibrational energies of some excited states.

Starting with a transformation of the Schrödinger equation from real time to imaginary time, its DMC solution can be easily understood in two different ways. One can consider it as solving the diffusion-reaction equation, an ordinary differential

equation, by employing stochastic calculus. The other way to think about the DMC method is as multi-dimensional Monte Carlo integration of Feynman path integral solution of the time-dependent Schrödinger equation, by which the wave-function can be expressed as a product of an infinite number of multi-dimensional integrals. Both formulations are explained in detail in Section 4.1, along with description of the *fixed-node* approximation as a successful attempt to solve excited vibrational states. Algorithm of the DMC method as well as a number of schemes of its parallelization are given in Section 4.2. In the final section, we address a few statistical concerns about interpreting the DMC results.

4.1. Theory

4.1.1. Asymptotic behavior

For illustration purpose, let us consider a single particle of mass m which moves along the x-axis in a potential $V(x)$. Its wave-function $\Psi(x, t)$ is governed by the time-dependent Schrödinger equation,

$$i\hbar \frac{\partial \Psi}{\partial t} = -\frac{\hbar^2}{2m} \frac{\partial^2 \Psi}{\partial x^2} + V(x)\Psi. \tag{4.1}$$

Assuming that $V(x) \to +\infty$ as $x \to \pm\infty$, the formal solution of Equation 4.1 can be written as a series expansion in terms of eigenfunctions $\phi_n(x)$ the one-dimensional Hamiltonian, i.e. the stationary state solutions, and corresponding eigenvalues E_n as follows,

$$\Psi(x, t) = \sum_{n=0}^{\infty} c_n \, \phi_n(x) \, e^{-\frac{i}{\hbar} E_n t}. \tag{4.2}$$

The coefficients c_n in the expansion can be determined by

$$c_n = \int_{-\infty}^{\infty} dx\, \phi_n(x) \Psi(x, 0); \quad \text{for } n = 0, 1, 2, \cdots. \tag{4.3}$$

Next, we introduce a trivial but methodological crucial shift of the energy scale E_{ref} by replacing $V(x)$ with $V(x) - E_{\text{ref}}$. Equation 4.1-4.2 then read

$$i\hbar \frac{\partial \Psi}{\partial t} = -\frac{\hbar^2}{2m} \frac{\partial^2 \Psi}{\partial x^2} + \left[V(x) - E_{\text{ref}} \right] \Psi, \tag{4.4}$$

and

$$\Psi(x, t) = \sum_{n=0}^{\infty} c_n\, \phi_n(x)\, e^{-i\frac{E_n - E_{\text{ref}}}{\hbar} t}. \tag{4.5}$$

Last, a transformation to imaginary time τ, defined as it covert the shifted Equations 4.4-4.5 to

$$\hbar \frac{\partial \Psi}{\partial \tau} = \frac{\hbar^2}{2m} \frac{\partial^2 \Psi}{\partial x^2} - \left[V(x) - E_{\text{ref}} \right] \Psi, \tag{4.6}$$

and

$$\Psi(x, \tau) = \sum_{n=0}^{\infty} c_n\, \phi_n(x)\, e^{-\frac{E_n - E_{\text{ref}}}{\hbar} \tau}. \tag{4.7}$$

One can infers from Equation 4.7 the following asymptotic behavior of the wave-function $\Psi(x, \tau)$ for $\tau \to \infty$:

- if $E_{\text{ref}} > E_0$, $\lim_{\tau \to \infty} \Psi(x, \tau) = \infty$, i.e. the wave-function diverges exponentially fast;

- if $E_{\text{ref}} < E_0$, $\lim_{\tau \to \infty} \Psi(x, \tau) = 0$, i.e. the wave-function vanishes exponentially fast;

- if $E_{\text{ref}} = E_0$, $\lim_{\tau \to \infty} \Psi(x, \tau) = c_0 \phi_0(x)$, i.e. the wave-function converges to the ground state wave-function.

This behavior provides the basis of the DMC method. Given $E_{\text{ref}} = E_0$, the wave-function $\Psi(x, \tau)$ will eventually converge to the ground state wave-function $\phi(x)$ after sufficiently long time propagation. It does not depend on the choice of the initial wave-function $\Psi(x, 0)$ as long as the there is a numerically significant overlap between $\Psi(x, 0)$ and $\phi_0(x)$, i.e. as long as c_0 is not too small.

4.1.2. Diffusion-reaction process

The DMC process can be formulated by realizing the similarity between Equation 4.6 and the following diffusion-reaction equation,

$$\frac{\partial C}{\partial t} = D \frac{\partial^2 C}{\partial x^2} - kC, \tag{4.8}$$

letting $D = \frac{\hbar}{2m}$ and $k = (V(x) - E_{\text{ref}})/\hbar$. First part of Equation 4.8,

$$\frac{\partial C}{\partial t} = D \frac{\partial^2 C}{\partial x^2}, \tag{4.9}$$

is the celebrated Einstein diffusion equation which describes microscopic transport of material and heat. The central limit theorem says that for a sufficiently long time the motion of a Brownian particle is described very well by a diffusion process. The trajectory of the Brownian particle, $x(t)$, also called the Wiener process, is not at all deterministic, but rather probabilistic such that the increment $x(t) - x(t_0)$ is Gaussian with mean 0 and variance $2D(t - t_0)$ for any $0 \mathrel{<=} t_0 < t$, and increments for nonover-

lapping time intervals are independent. The Wiener process $x(t)$ is characterized by the probability distribution

$$
P(x, t | x_0, t_0) = \frac{1}{\sqrt{4\pi D(t - t_0)}} \exp\left[-\frac{(x - x_0)^2}{4D(t - t_0)}\right] \tag{4.10}
$$

$$
= \left(\frac{m}{2\pi\hbar(t - t_0)}\right)^{\frac{1}{2}} \exp\left[-\frac{m(x - x_0)^2}{2\hbar(t - t_0)}\right]. \tag{4.11}
$$

It can be shown that the the probability distribution $P(x, t | x_0, t_0)$ is the fundamental solution of Equation 4.9. The second part of Equation 4.8,

$$
\frac{\partial C}{\partial t} = -kC, \tag{4.12}
$$

is simply a first-order rate equation that describes the decrease (positive k) or increase (negative k) of the concentration C. The solution reads,

$$
\frac{C(x, t)}{C(x_0, t_0)} = \exp(-k(t - t_0)) \tag{4.13}
$$

$$
= \exp\left[-\frac{(V(x) - E_{\text{ref}})(t - t_0)}{\hbar}\right]. \tag{4.14}
$$

Based on the above solutions and the equivalence of $\Psi(x, \tau)$ and $C(x, t)$, the procedure to solve the imaginary-time Schrödinger equation can be considered as a random-walk game for particles which are subject to disappearance (or multiplication) with a probability given by Equation 4.13. It is worth noting that since $C(x, t)$ is a probability distribution, the wave-function $\Psi(x, \tau)$ should be positive definite, a constraint that limits the applicability of the suggested method. Thus, this method can be used directly to solve the nodeless ground state wave-function of Bosons, e.g. nuclei; however its application to the wave-function that changes sign requires additional constraint.

The random-walk game for solving the Schrödinger equation in one dimension may thus be envisioned as follows: An initial collection of random walkers is distributed on a line. Time is advanced one step $\Delta\tau$ and each walker is moved right or left at random one step $\Delta x = \sqrt{2\hbar\Delta\tau/m}$. Then each walker gives birth to a new walker of the same position with a probability $P_b = \exp[-(V(x+\Delta x) - E_{\text{ref}})\Delta\tau/\hbar] - 1$ if $V(x+\Delta x) > E_{\text{ref}}$ or disappears with a probability $P_d = \exp[(V(x+\Delta x) - E_{\text{ref}})\Delta\tau/\hbar]$ if $V(x+\Delta x) < E_{\text{ref}}$. E_{ref} is then adjusted according to the $\langle V \rangle$ of all existed random walkers. Time is advanced another step and the process is repeated until convergence of E_{ref} is achieved.

4.1.3. Path integral formalism

A second formulation of the DMC method arises from the famous Feynman path integral solution of the time-dependent Schrödinger equation. The solution of Equation 4.6 can be written as

$$\Psi(x,\tau) = \int_{-\infty}^{+\infty} dx_0\, K(x,\tau|x_0,0)\Psi(x_0,0), \tag{4.15}$$

where the propagator $K(x,\tau|x_0,0)$ is express in terms of the path integral [50], modified by the replacement $t = -i\tau$,

$$K(x,\tau|x_0,0) = \lim_{N\to\infty} \int_{-\infty}^{\infty} dx_1 \cdots \int_{-\infty}^{\infty} dx_{N-1} \left(\frac{m}{2\pi\hbar\Delta\tau}\right)^{\frac{N}{2}} \times$$
$$\exp\left\{-\frac{\Delta\tau}{\hbar}\sum_{j=1}^{N}\left[\frac{m}{2\Delta\tau^2}(x_j - x_{j-1})^2 + V(x_j) - E_{\text{ref}}\right]\right\}, \tag{4.16}$$

where $\Delta\tau = \tau/N$ is a small time step and let $x_N \equiv x$. More concisely, the wavefunction $\Psi(x, \tau)$ can be rewritten as

$$\Psi(x, \tau) = \lim_{N \to \infty} \int_{-\infty}^{\infty} \left(\prod_{j=0}^{N-1} dx_j \right) \prod_{n=1}^{N} W(x_n) \times P(x_n, x_{n-1}) \Psi(x_0, 0), \qquad (4.17)$$

where we define

$$P(x_n, x_{n-1}) = \left(\frac{m}{2\pi\hbar\Delta\tau} \right)^{\frac{1}{2}} \exp\left[-\frac{m(x_j - x_{j-1})^2}{2\hbar\Delta\tau} \right], \qquad (4.18a)$$

$$W(x_n) = \exp\left[-\frac{[V(x_j) - E_{\text{ref}}]\Delta\tau}{\hbar} \right]. \qquad (4.18b)$$

We note that Equations 4.18 are exactly the same as Equation 4.11 and 4.14, which are derived from diffusion-reaction process. Therefore, the same DMC procedure holds. Details about this formalism can be found elsewhere [51].

4.2. Implementation

4.2.1. Hamiltonian in different coordinates

The DMC method can be easily extended to quantum systems with more than one degree of freedom. The exact nuclear Hamiltonian for a N-atom system in Cartesian coordinates reads

$$\hat{H} = -\sum_{i=1}^{N} \frac{\hbar^2}{2m_i} \nabla_i^2 + V(\mathbf{R}), \qquad (4.19)$$

where $\mathbf{R}$ is the Cartesian coordinates of the N-atom system. The DMC simulation can also be done in saddle-point, mass-scaled normal coordinates $\mathbf{Q}$ using an approximate

Hamiltonian,

$$\hat{H} = -\frac{\hbar^2}{2} \sum_{i=1} \frac{\partial^2}{\partial Q_i^2} + V(\mathbf{Q}), \tag{4.20}$$

where the vibrational angular momentum coupling terms are neglected, as long as the set of normal mode coordinates serves a valid expansion of the wave-function, i.e. it must be able to describe any possible exchange in the DMC simulation. In this case, the DMC algorithm for quantum systems in Cartesian coordinates is essentially equivalent to that in normal coordinates.

4.2.2. Fixed-node approximation

The DMC method discussed so far rely on resemblance between the wave-function and the probability distribution which by definition is positive and definite. The method is therefore only applicable to approach the nodeless wave-functions so far. Wave-functions for excited state atomic and for system containing electrons of the same spin contain nodes on which $\Psi = 0$; there are spacial regions of positive and negative sign. An obvious thought of the extension to these states will be doing the DMC simulation within a single region that does not change sign. The realization of such confinement is termed the "fixed-node" approximation, which was first proposed by Anderson [49] for the nodal problem. This approximation is variational: the fixed-node DMC energy is an upper bound to the exact solution.

As implied by name, knowledge of the nodal surface is prerequisite to employing the "fixed-node" approximation. Examples of constructing the nodal surface can be found in Section 6.3 and 7.4. Ideally, provided the position of the node, one can apply the nodal constraint by removing any random walkers that cross the node. However, it is not quite true due to the use of finite time step, $\Delta\tau$. For a random walker located

near a node and found on the allowed side of the node at both the beginning and end of a time step, there is possibility that the walker may have crossed and recrossed the node in the interval of the time step. In the limit of small $\Delta\tau$ this possibility becomes negligible, but for finite step sizes the failure to eliminate random walkers subject to disappearance if their complete paths were determined may cause an applicable error. On this account, Anderson introduced a correction based on the probability of crossing and recrossing the node [49], expressed as

$$P_{\text{recross}} = \exp\left(-\frac{2m\,r'\,r''}{\hbar\Delta\tau}\right), \qquad (4.21)$$

where r' and r'' represent the shortest distances to the nodal surface at the beginning and the end of the time step. We can see that consistently the recross probability will be small as one use a small $\Delta\tau$ and greater than 1 when walkers do cross. Moreover, the shorter the distances to the node the greater the recross probability. Also the probability is smaller for heavier walker as expected. In principle DMC calculations on both sides of the node should give numerically the same solution, thus they serve as a good indicator of the accuracy of the node definition.

4.2.3. Algorithm

The standard DMC algorithm designed particularly for solving the M-dimensional wave-function of nuclei is given below:

1. INITIALIZE a collection of N_0 walkers distributed according to the initial wave-function $\Psi(\mathbf{R}, 0)$, which we often choose as a *Dirac δ*-function

$$\Psi(\mathbf{R}, 0) = \delta(\mathbf{R} - \mathbf{R}^{(0)}). \qquad (4.22)$$

The amplitude of the target wave-function is expected to be large at $\mathbf{R}^{(0)}$. Hence, the initial distribution (Equation 4.22) is obtained by simply duplicating the configuration $\mathbf{R}^{(0)}$ for N_0 walkers. This step also includes initialization of the time step size $\Delta\tau$, a so-called "feedback" parameter α, which is practically chosen to be $\hbar/\Delta$, the number of time steps T_0 needed for equilibrating the quantum system, and the total propagation time steps T.

Apparently, any systematic errors due to the finite discretization in time space of the standard DMC method can be systematically reduced by decreasing $\Delta\tau$. However, a smaller $\Delta\tau$ actually increases the needed computer time to converge the wave-function by rendering the successive generations of random walkers more correlated such that the simulation takes longer to completely sample the configuration space. Hence, Δ is always chosen short enough to keep the systematic error small but without increasing too much statistical error (see more in Section 4.4) due to the increased correlation between the successive distributions of random walkers.

In real simulation, firstly the T_0 steps of DMC propagation is performed to obtain a distribution of random walkers that closely represents the target wave-function. After that, additional $T - T_0$ DMC steps are run for the sake of reducing statistical errors.

2. PROPAGATION *for i:=1 to T*

   a) GAUSSIAN RANDOM WALK: for every $j \leq N_{i-1}$, generate a vector of M standard Gaussian random numbers with zero mean and a variance equal to one, $\vec{\rho}$, and then obtain a new configuration of jth random walker according to

$$\mathbf{R}_{\mathbf{j}}^{(\mathbf{i})} = \mathbf{R}_{\mathbf{j}}^{(\mathbf{i-1})} + \vec{\sigma} \cdot \vec{\rho}, \tag{4.23}$$

where $\vec{\sigma} = \sqrt{\hbar\Delta\tau/\vec{m}}$, and $\vec{m}$ is a collection of M masses corresponding to the M-dimension configuration $\mathbf{R}$.

b) BIRTH-DEATH PROCESS: for every $j \leq N_{i-1}$,

    i. when there is a node, remove j^{th} walker if the walker crosses the node; if not, eliminate the walker if the recross probability defined by Equation 4.21 for j^{th} walker is greater than a random number selected in the closed interval $[0, 1]$. If this random walker is killed then process to the next random walker, else move to the following step.

    ii. compute the weight of the new configuration $\mathbf{R_j^{(i)}}$

$$W(\mathbf{R_j^{(i)}}) = \exp\left[-\frac{[V(\mathbf{R_j^{(i)}}) - E_{\text{ref}}]\Delta\tau}{\hbar}\right], \tag{4.24}$$

and an integer $m = \min\left(\text{int}[W(\mathbf{R_j^{(i)}}) + u], 3\right)$, where $\text{int}[x]$ denotes the integer part of x and u represents a random number uniformly distributed in the closed interval $[0, 1]$. In case $m = 0$ the jth walker is removed and this is referred to as a "death" of a random walker. In case of $m = 1$, the new configuration of jth walker is accepted and then the next process continues. In case $m = 2, 3$ one simply add $m - 1$ number of random walkers of exactly the same configuration $\mathbf{R_j^{(i)}}$ into the ensemble and this is referred to as the "birth" of random walkers. [The limitation on the birth rate of the random walkers, i.e. three in this algorithm, is initially designed to avoid numerical instability; however in the real simulation of nuclear motions m is rarely greater than 2.]

c) SMALLCAPS COUNT the total number of random walkers N_i after the birth-death process and update the reference energy E_{ref} as

$$E_{\text{ref}} = \overline{V} - \alpha \frac{N_i - N_0}{N_0}. \qquad (4.25)$$

where $\overline{V}$ represents the mean potential energy of all of the random walkers at i^{th} step and α is the "feedback" parameter. [Generally the value of α is chosen to be the inverse of the time step. Practically the larger the α the greater the fluctuation in E_{ref} and N, and the smaller unwanted correlations between the successive distributions of random walkers.] We are now all set for the next DMC step.

d) ACCUMULATE $\langle E \rangle$ if $i > T_0$ according to

$$\langle E \rangle_i = \frac{(i - T_0 - 1)\langle E \rangle_{i-1} + E_{\text{ref}}}{i - T_0}, \qquad (4.26)$$

3. FINAL value of $\langle E \rangle$ after T DMC steps serves as a valid estimator of the eigenvalue of the target quantum state of nuclei.

A Pseudocode of the above sequential algorithm of DMC is shown in Figure 4.1.

4.3. Parallelization of DMC

4.3.1. OpenMP

As seen, the DMC algorithm shown in Section 4.2.3 is naturally parallelizable, especially for a shared-memory machine, where all the processors access one global memory. An example of shared-memory parallelization of DMC algorithm imple-

```
call dmc_init();
do i_step = 1, n_step
    ! propagate
    do i_walker = 1, n_walker
        call random_number( i_disp )
        call displacement( i_geom, i_disp );
        call potential( i_pot, i_geom );
        call weight( i_weight, i_pot,v_ref );
        call branch( i_weight );
    end do

    ! update reference energy
    call average( v_ref );

    ! accumulate
    if ( i_step > equilibrium_step ) then
        call accumulate( v_sum, v_ref );
    end if
end do
zpe = v_sum / ( n_step - equilibrium_step );
```

Figure 4.1. Diffusion Monte Carlo: a sequential pseudocode.

mented with the use of "OpenMP", an application programming interface (API) for writing multithreaded applications, is shown in Figure 4.2. As seen, not much modification is needed to move from the sequential code to a OpenMP code. All we need to do is to identify the part of the sequential code that can be executed safely in parallel without interrupting each other and writing on the same memory address. Then put the parallelizable part of the code into parallel executing blocks and the remaining into the single-thread/sequential blocks.

4.3.2. MPI

The parallelization scheme of DMC will be a bit more complicated with a message-passing model, where processes are distributed to separated address spaces and communication among processes is required. The MPI is the most popular standard for

```
call dmc_init();
call omp_set_num_threads(nprocs);
!$omp parallel
do i_step = 1, n_step
!$omp single
   do i_walker = 1, n_walker
      call random_number( i_disp )
      call displacement( i_geom, i_disp );
   end do
!$omp end single
!$omp do
   do i_walker = 1, n_walker
      call potential( i_pot, i_geom );
      call weight( i_weight, i_pot,v_ref );
   end do
!$omp end do
!$omp single
   do i_walker = 1, n_walker
      call branch( i_weight );
   end do
   call average( v_ref );
   if ( i_step > equilibrium_step ) then
      call accumulate( v_sum, v_ref );
   end if
!$omp end single
end do
!$omp end parallel
zpe = v_sum / ( n_step - equilibrium_step );
```

Figure 4.2. Diffusion Monte Carlo: a parallel pseudocode for a shared-memory machine.

message-passing model. MPI program can be running on either distributed memory system or shared-memory system.

In a simple MPI implementation of DMC shown in Figure 4.3, the walkers are evenly distributed among the computing processors. Within each processor, the algorithm is exactly the same as the sequential one. By the end of each time step, the average potential of walkers as well as the number of walkers still alive in every processors need to be passing around, so as to update the reference energy for the

next time step. In addition, a parallel random number generator is necessary in such application.

```
#include "mpi.h"

MPI_Init(&argc, &argv);
MPI_Comm_size(MPI_COMM_WORLD,&nprocs);
MPI_Comm_rank(MPI_COMM_WORLD,&myid);
if ( myid == master ) then
   dmc_init();
   MPI_Bcast( ... );
else
   MPI_Bcast( ... );
end if
local_n_walker = n_walker / nprocs;
do i_step = 1, n_step
   ! propagate
   do i_walker = 1, local_n_walker
      random_number( i_disp )
      displacement( i_geom, i_disp );
      potential( i_pot, i_geom );
      weight( i_weight, i_pot,v_ref );
      branch( i_weight );
   end do
   MPI_Allreduce( v_tot, n_tot );
   average( v_ref );
   if ( myid == master ) then
      if ( i_step > equilibrium_step ) then
         accumulate( v_sum, v_ref );
      end if
   end if
end do
zpe = v_sum / ( n_step - equilibrium_step );
MPI_Finalize();
```

Figure 4.3. Diffusion Monte Carlo: a parallel pseudocode using the message-passing model.

However, this simple modification would result in a low parallel efficiency when the number of processors used grows or the number of random walkers is very limited. In both cases, the calculation would become poorly load balanced as the calculation progressed. The birth-death processes would result in some processors having more

walkers than others; at the end of each time step many processors would have to wait whilst others propagate their remaining walkers. A load balanced DMC algorithm requires the even distribution walkers over all processors, and this is accomplished by redistributing the walkers in a certain way. The trade-off of this load balanced algorithm is the increase of communication among processors.

4.4. Statistics Analysis

Two methods[52–54] can be applied to determine the statistical uncertainty of the DMC energies. One reasonable estimator for the variance of the mean, $\tilde{\sigma}_{\overline{\mathcal{O}}}^2$, for correlated data is to multiply the expression for uncorrelated data by the autocorrelation time κ as in the following formula,

$$\tilde{\sigma}_{\overline{\mathcal{O}}}^2 = \sigma_{\overline{\mathcal{O}}}^2 \kappa. \tag{4.27}$$

Here κ in discrete space is defined as the sum of normalized discrete autocorrelation functions,[54]

$$\kappa = 1 + 2 \sum_{k=1}^{T} C(k), \tag{4.28}$$

where T is a cut-off parameter in the sum, and the normalized autocorrelation function $C(k)$ as a function of time step k reads

$$C(k) \approx \frac{\sum_{i=1}^{N-k} (\mathcal{O}_i - \overline{\mathcal{O}})(\mathcal{O}_{i+k} - \overline{\mathcal{O}})}{\sum_{i=1}^{N} (\mathcal{O}_i - \overline{\mathcal{O}})^2}. \tag{4.29}$$

A typical choice of T is approximately three times the value of the autocorrelation time, and this time can be determined by an iterative approach. The other approach is termed the blocking method; this involves repeated averaging of data in blocks

longer than the correlation time until it is uncorrelated, i.e. the variance of the mean of the block averages remains approximately constant. The "converged" variance also serves a fair estimator for the square of the statistical uncertainty.

Chapter 5.

MULTIMODE

Having said that the diffusion Monte Carlo (DMC) is such a wonderful method to solve the nuclear Schrödinger equation in full dimensionality that scales almost nearly with the size of the system, its application is largely limited to the ground vibrational state and a small number of low-lying excited states. In this chapter, we will focus on another full-dimensional quantum approach towards "exact" solutions of Schrödinger equation, the so-called variational methods, that could obtain a large range of vibrational states simultaneously, though they are generally much more computationally intensive than DMC calculations.

The general procedure of variational calculations involves selecting coordinates appropriate for the system of interest, e.g. internal coordinates and normal coordinates are two common choices. Next choose basis functions for each coordinate and expand the full wave-function in terms of those basis functions in a certain way, e.g. direct product forms. The variational best energies and wave-functions is therefore the solutions of a generalized eigenvalue problem in a given basis:

$$\det \left(\mathbf{H} - \mathbf{E}\mathbf{S} \right) = 0, \tag{5.1}$$

where $\mathbf{H}$ is the full ro-vibrational Hamiltonian matrix whose element given by $H_{lm} = \langle l|\hat{H}|m\rangle$, and $\mathbf{S}$ is the overlap integral of the basis functions defined by $S_{lm} = \langle l|m\rangle$. If the given basis is orthogonal, the $\mathbf{S}$ becomes nothing but the identify matrix $\mathbf{S} \equiv \mathbf{I}$, and the Equation 5.1 is simplified as a standard eigenvalue problem, $\det(\mathbf{H} - \mathbf{EI}) = 0$. All of the variational calculations presented in this thesis are performed using a variational code MULTIMODE [55, 56], which is based on the well-known Watson Hamiltonian in normal coordinates. Armed with a n-mode representation of the full potential, the code MULTIMODE has been widely applied to a variety of fairly large molecular systems, including solving a nine-atom system, malonaldehyde, in full dimensionality (see Chapter 6).

In this chapter, we will describe fundamentals of the theory and numerical methods used in the code MULTIMODE, including the Watson Hamiltonian in Section 5.1, basis functions in Section 5.2, and two types of variational calculations in Section 5.4. Following that, we briefly highlight a number of features of this code. More details can be found in Ref. [55].

5.1. Watson Hamiltonian

Dealing with a nonlinear polyatomic molecule, the code MULTIMODE employs the familiar Watson Hamiltonian [57], which is given in the normal coordinates $\mathbf{Q}$ by

$$\hat{H} = \frac{1}{2}\sum_{\alpha\beta}\left(\hat{J}_\alpha - \hat{\pi}_\alpha\right)\mu_{\alpha\beta}\left(\hat{J}_\beta - \hat{\pi}_\beta\right) - \frac{1}{2}\sum_k^N \frac{\partial^2}{\partial Q_k^2} - \frac{1}{8}\sum_\alpha \mu_{\alpha\alpha} + V(\mathbf{Q}). \qquad (5.2)$$

where subscripts α and β refer to the x, y and z components of Cartesian coordinates, $\hat{J}_\alpha$ and $\hat{\pi}_\alpha$ is the Cartesian component of the total and vibrational angular momenta respectively, $\mu_{\alpha\beta}$ is the inverse effective moment of inertia tensor and V is the full

potential in terms of the N normal coordinates denoted collectively in this equation by $\mathbf{Q}$. This expression can be further simplified for a nonrotating molecule with $J = 0$ as

$$
\begin{aligned}
\hat{H} &= \frac{1}{2} \sum_{\alpha\beta} \mu_{\alpha\beta} \hat{\pi}_\alpha \hat{\pi}_\beta - \frac{1}{2} \sum_k^N \frac{\partial^2}{\partial Q_k^2} - \frac{1}{8} \sum_\alpha \mu_{\alpha\alpha} + V(\mathbf{Q}) && \text{(5.3a)} \\
&= T_c + T_v + T_w + V(\mathbf{Q}), && \text{(5.3b)}
\end{aligned}
$$

where the first term T_c is the vibration-rotation (Coriolis) coupling, the second term T_v is the pure vibration kinetic operator and the third T_w is the so-called Watson correction term [57]. In fact, Equation 5.3 is the basis of the part of the MULTIMODE code that we have been using extensively for related work presented in this thesis.

It is well known that the approach used in previous sections for nonlinear molecules is not applicable to linear systems as one of the moments of inertia will be zero.

5.2. Basis Functions and Quadrature

Between two common categories of variational procedures, one employing grid based methods and the other employing a finite basis representation, MULTIMODE chose the latter. Naturally following the choice of Watson Hamiltonian which is expressed in terms of normal coordinates, MULTIMODE uses the harmonic oscillator wave-functions as building blocks of its finite basis representation. The harmonic oscillator wave-function of Q_i used in MULTIMODE implementation is defined as

$$
\varphi_\nu(\overline{Q}_i) = N_\nu H_\nu(\overline{Q}_i) \exp\left(-\frac{1}{2}\overline{Q}_i^2\right), \tag{5.4}
$$

where

$$\overline{Q}_i = 2\pi(v_i/h)^{\frac{1}{2}}Q_i, \tag{5.5}$$

and $v_i = \sqrt{\lambda_i}/2\pi$ is the frequency of the ith normal mode, N_ν is a trivial normalization factor, and H_ν is the Hermite polynomial of degree ν. The first three polynomials are

$$H_0(x) = 1, \quad H_1(x) = 2x, \quad H_2(x) = 4x^2 - 2, \tag{5.6}$$

and the higher polynomials may be obtained from the recursion formula

$$H_{\nu+1}(x) - 2xH_\nu(x) + 2\nu H_{\nu-1}(x) = 0. \tag{5.7}$$

Clearly, the harmonic oscillator wave-functions are orthogonal and have analytical derivatives and integrals which makes them amenable for use in variational calculations.

5.3. n-Mode Representation of the Potential

As noted above, even eased by the use of Gauss-Hermite quadrature that the quadrature point is minimized in each dimension, one still need to deal with the exponential increase of the computational cost on the order of M^N, as the dimension of the integration grows. The full-dimensional potential is the major source of such integrations and it had been expanded as a Taylor series in the normal coordinates about the equilibrium geometry, and is truncated at a certain order (usually at fourth order).

The general form of the potential is

$$V(\mathbf{Q}) = \sum_{a,b,\cdots,c} \mathcal{F} Q_1^a Q_2^b \cdots Q_N^c. \tag{5.8}$$

This expression has the advantage of being analytically integrable, but the radius of convergence of the potential is uncertain. Additionally, the potential can become unphysical for large displacements, leading to possible numerical instability in variational calculations when the size of basis increased. Further, for larger molecules the numerical determination of a full multinomial expansion can be quite difficult and cumbersome. The key approximation in MULTIMODE is to represent the potential in a novel way that permits calculations for many-mode systems.

MULTIMODE incorporates the hierarchical n-mode representation (nMR) of the full potential in normal coordinates [58]:

$$V(Q_1, Q_2, \cdots, Q_N) \simeq \sum_i V_i^{(1)}(Q_i) + \sum_{i,j} V_{ij}^{(2)}(Q_i, Q_j) + \sum_{i,j,k} V_{ijk}^{(3)}(Q_i, Q_j, Q_k)$$
$$+ \sum_{i,j,k,l} V_{ijkl}^{(4)}(Q_i, Q_j, Q_k, Q_l) + \cdots + \sum_{i,j,k,l\cdots} V_{ijkl\cdots}^{(n)}(Q_i, Q_j, Q_k, Q_l, \cdots). \tag{5.9}$$

In this expression the one-mode representation of the potential contains only $V_i^{(1)}(Q_i)$ terms,

$$V_i^{(1)}(Q_i) = V(Q_1 = 0, \cdots, Q_{i-1} = 0, Q_i, Q_{i+1} = 0, \cdots, Q_N = 0), \tag{5.10}$$

that are cuts through the hyperspace of normal coordinates with just one coordinate varying at a time and others remain zero, and there are N of these terms for any N-mode system. Since the basis function we use is a direct product of orthogonal single mode harmonic wave-functions, the multidimensional basis integration over the one-mode representation of the potential turns out to be just single mode integration,

i.e. the integrations in those unchanged modes will be simple a delta function due to the orthogonality of the basis functions. The two-mode representation contains those one-mode terms plus the $V_{ij}^{(2)}(Q_i, Q_j)$ terms, expressed as

$$V_{ij}^{(2)}(Q_i, Q_j) = V(Q_1 = 0, \cdots, Q_i, Q_{i+1} = 0, \cdots, Q_j, Q_{j+1} = 0, \cdots, Q_N = 0)$$
$$- V_i^{(1)}(Q_i) - V_j^{(1)}(Q_j). \quad (5.11)$$

The remaining three-mode terms $V_{ijk}^{(3)}(Q_i, Q_j, Q_k)$, four-mode terms $V_{ijkl}^{(4)}(Q_i, Q_j, Q_k, Q_l)$, and up to n-mode terms $V_{ijkl\ldots}^{(n)}(Q_i, Q_j, Q_k, Q_l, \cdots)$ in the n-mode representation can be defined in the exactly same fashion.

Due to limited computational resources, this representation is usually truncated at the value of n between 3 and 5, say 4 for instance. Thus, the multidimensional basis integration over the potential can be written as a sum of all single mode integrations, two-mode integrations, three-mode integrations and four-mode integrations. The cost is then reduced to $\mathcal{O}(M^4)$ in this case.

Also, this representation of the potential affords a systematic approach to test and increase the accuracy of the n-mode representation of the potential. A test of the accuracy can be (and generally is) done by examining the convergence of eigenvalues of the variational calculation with respect to the level of mode coupling in terms of n here. The accuracy of the calculation will increase as n increases, and this can be increased as computational resources increase.

5.4. Variational Calculation

5.4.1. Vibrational self-consistent field theory

In the self-consistent field (SCF) approach [58–60], we first assume that the total wave-function for the quantum state $K = (k_1, k_2, \cdots, k_N)$ is expanded as a product of some normalized single-mode (modal) wave-functions $\psi^{(k_i)}(\overline{Q}_i)$,

$$\Phi_K = \prod_{i=1}^{3N-6} \psi^{(k_i)}(\overline{Q}_i), \tag{5.12}$$

where k_i represents the eigenstate of the ith modal function and $\overline{Q}_i$ is the scaled normal coordinates mentioned in Section 5.2. Now, we seek the variationally best form of the modal wave-functions $\psi^{(k_i)}(\overline{Q}_i)$. This is achieved by requiring that the expectation value of the Watson Hamiltonian ($J{=}0$) (5.3) of the state $|K\rangle$ be stationary with respect to small variation in each of the modals subject to the constraint that each modal be normalized. Mathematically, this general optimization problem with constraint can be solved by the method of Lagrange multipliers as follows:

$$\mathcal{L} = \langle \Phi_K | H | \Phi_k \rangle - \lambda(\langle \Phi_K | \Phi_K \rangle - 1); \tag{5.13a}$$

$$\delta\mathcal{L} = \delta\langle \Phi_K | H | \Phi_k \rangle - \lambda\delta\langle \Phi_K | \Phi_K \rangle = 0. \tag{5.13b}$$

The variational procedure mentioned above yields a set of coupled SCF equations which the modal wave-functions satisfy,

$$\left[\hat{T}_i + \left\langle \prod_{l\neq i}^{N} \psi^{(k_l)}(\overline{Q}_l) \,\Big|\, V(\mathbf{Q}) + \hat{T}_c \,\Big|\, \prod_{l\neq i}^{N} \psi^{k_l}(\overline{Q}_l) \right\rangle - \lambda_i \right] \psi^{(k_i)}(\overline{Q}_i) = 0 \tag{5.14}$$

where

$$\hat{T}_i \equiv -\frac{1}{2}\frac{\partial^2}{\partial Q_i^2}, \quad \hat{T}_c \equiv \frac{1}{2}\sum_{\alpha\beta}\mu_{\alpha\beta}\hat{\pi}_\alpha\hat{\pi}_\beta - \frac{1}{8}\sum_\alpha \mu_{\alpha\alpha}, \tag{5.15}$$

and the integration is over the coordinates of $N-1$ modals. These coupled equations are typically solved iteratively for each modal wave-function with a finite basis representation. The modal function $\psi^{(k_i)}(\overline{Q}_i)$ is expressed as linear summation of a finite set of basis functions multiplied by unknown coefficients

$$\psi^{(k_i)}(\overline{Q}_i) = \sum_{n_i}^{F_i} C_{n_i}^{(k_i)}\phi^{(n_i)}(\overline{Q}_i), \tag{5.16}$$

here F_i is the number of basis functions for the ith mode. The coefficients can then be determined by diagonalizing Hamiltonian matrix expanded on the finite basis.

The set of F_i basis functions $\{\phi^{(n_i)}(\overline{Q}_i) : n_i = 1, 2, \cdots, F_i\}$ could be as simple as a set of F_i harmonic oscillator basis wave-functions; however, to make the basis more compact in MULTIMODE implementation it is written as a linear sum of P_i harmonic oscillator basis wave-functions

$$\phi^{(n_i)}(\overline{Q}_i) = \sum_\nu^{P_i} c_\nu^{(n_i)}\varphi_\nu(\overline{Q}_i) = e^{-\frac{1}{2}\overline{Q}_i^2}\sum_\nu^{P_i} c_\nu^{(n_i)}H_\nu(\overline{Q}_i), \tag{5.17}$$

where the P_i number of coefficients $\{c_\nu^{(n_i)}\}$ are obtained by solving the following simple one-dimensional potential for the ith mode,

$$\left[-\frac{1}{2}\frac{d^2}{dQ_i^2} + V_i^{(1)}(Q_i) - \epsilon_i\right]\phi^{(n_i)}(\overline{Q}_i) = 0. \tag{5.18}$$

Usually we have $P_i \geq F_i$ and select the first F_i eigen-functions to form the contracted basis functions $\{\phi^{(n_i)}(\overline{Q}_i) : n_i = 1, 2, \cdots, F_i\}$.

The quality of basis functions is essential to variational calculations. Our experience tells that the harmonic frequency of the ith mode usually serves as a good value for v_i of the harmonic oscillator basis functions in Equation 5.5, unless the $V_i^{(1)}(Q_i)$ is very anharmonic, in which case the value of v_i would better be tuned to render a close resemblance between $\frac{1}{2}\overline{Q}_i^2$ and $V_i^{(1)}(Q_i)$. The convergence of solutions to these one-dimensional problems can be achieved by gradually increasing the number of harmonic oscillator wave-functions P_i.

Since the potential $V_i^{(1)}(Q_i)$ does not always have the analytical expression, the integral $\langle\phi^{(n_i)}|V_i^{(1)}|\phi^{(n_i')}\rangle$ is carried out numerically using Gaussian quadrature rule. The M-point Gauss-Hermite quadrature rule says

$$\int_{-\infty}^{\infty} f(x)e^{-x^2}\,dx = \sum_{I}^{M} w_I\,f(a_I) + \mathcal{O}\left(f^{(2M)}(\xi)\right), \qquad (5.19)$$

where the abscissas a_I are the roots of Hermite polynomial of order M, i.e. $H_M(a_I) = 0$, and the associated weights w_I are given by

$$w_I = \frac{2^{M-1}M!\sqrt{\pi}}{M^2[H_{M-1}(a_I)]^2}. \qquad (5.20)$$

As indicated, the last residual term in Equation 5.19 vanishes if the degree of $f(x)$ is less than $2M-1$. In other words, a function of degree up to $2M-1$ is integrated exactly by M quadrature points. Practically, the number of Gauss-Hermite quadrature points M_i in each dimensional is set to $P_i + 5$. Thus, the quadrature is exact when the $V_i^{(1)}(Q_i)$ can be represented by polynomials of degree less than 9; this is very often the case. Lastly, the number of contracted modal functions F_i largely depends on the energy of the eigenstates of interest, i.e. the higher the eigenstate in energy the larger F_i.

To further improve the efficiency of the multidimensional quadrature in the VSCF procedure, the Gaussian quadrature grids and weights are optimized with respect to the contracted basis functions $\{\phi^{(n_i)}(\overline{Q}_i) : n_i = 1, 2, \cdots, F_i\}$ through the diagonalization of the following matrix

$$\langle l|\overline{Q}_i|m\rangle = \int \phi^{(l)}(\overline{Q}_i)\,\overline{Q}_i\,\phi^{(m)}(\overline{Q}_i)\,d\overline{Q}_i; \quad l, m = 1, 2, \cdots, F_i. \qquad (5.21)$$

The optimized quadrature points are given as the eigenvalues of this matrix, whose eigenvectors are the products of the weights and optimized basis functions. These pints and weights are used to integrate all subsequent matrix elements which are established in the optimized function $\{\phi^{(n_i)}(\overline{Q}_i) : n_i = 1, 2, \cdots, F_i\}$.

5.4.2. Configuration interaction

As seen in Equation 5.14, in addition to the part of Hamiltonian that depends only on $\overline{Q}_i$ the VSCF equations include the coupling among the remaining modes as an effective potential averaged over all the remaining coordinates. The configuration interaction (CI) approaches as extensions to the VSCF calculations yields better accuracy by explicitly including correlation among modes, although being much more computationally intensive. Historically, there are two "CI" schemes [61], denoted by "VSCF+CI" and "virtual state CI (VCI)" respectively. The latter VCI scheme gains the popularity in most of our CI calculations due to its use of orthonormal basis functions, and therefore results in a standard eigenvalue problem. In the VCI scheme, the VSCF wave-function of one particular state, usually the ground state Φ_0 is solved, and then the VCI total wave-function is expanded in terms of the virtual states of

the given VSCF Hamiltonian,

$$\Psi = \sum_K D_K \tilde{\Phi}_K = \sum_K D_K \prod_{i=1}^{3N-6} \tilde{\psi}^{(k_i)}(\overline{Q}_i), \qquad (5.22)$$

where $\tilde{\psi}^{(k_i)}(\overline{Q}_i)$ come from the last VSCF iteration of ground state of each mode, and K is the index of tuples $(k_1, k_2, \cdots, k_N)$.

These CI schemes can result in very large Hamiltonian matrices and so a very flexible basis set selection method has been developed for the VCI scheme in MULTIMODE. The selection method divides the excitations into one-mode, two-mode, three-mode and four-mode excitations (even five-mode and six-mode in some cases) and limits the total number of quanta excited in the four classes of mode excitation. In addition, the maximum number of excitations in any mode can be further restricted. Another consideration in making this approach efficient is to make use of the symmetry when it is appropriate, so that the full Hamiltonian matrix is actually constituted of a number of diagonal blocks, and the off-diagonal blocks are certainly zero since they correspond to interactions between states belongs to different symmetries.

5.5. Infrared Intensity

The complete infrared spectrum involves the calculation of transition densities for all populated rovibrational states, and the value of J will depend on the Boltzmann population at a given temperature T. Moreover, in calculating the transition dipole matrix element, the dipole moment defined in the molecular-fixed coordinates must be related to the space-fixed axes via the Eular angles. Nevertheless, in the simplified MULTIMODE calculations for $J = 0$, we consider only the pure vibrational line

intensities [62]. For a complete calculation of rovibrational intensities, we shall refer to a pretty recent update of MULTIMODE in Ref. [63].

Once the vibrational states have been solved using either VSCF or VCI, provided with the dipole moment surface (DMS) the transition dipole matrix element given by

$$R_{\nu\nu'}^{\alpha} = \langle \Psi_\nu(\mathbf{Q})|\mu^\alpha(\mathbf{Q})|\Psi_{\nu'}(\mathbf{Q})\rangle, \tag{5.23}$$

where $\Psi_\nu(\mathbf{Q})$ and $\Psi_{\nu'}(\mathbf{Q})$ are vibrational wave-functions for vibrational state ν and ν' respectively, and $\mu^\alpha(\mathbf{Q})$ is the α component ($\alpha = x, y, z$) of the molecular-fixed dipole moment $\vec{\mu}$. In MULTIMODE, we have molecular-fixed axes which are the instantaneous principle (Eckart-frame) axes of the system by construction [57]. This coordinate system minimizes the interaction between vibration and rotation. As seen, the integration in Equation 5.23 is performed in the normal coordinates, and thus $\mu^\alpha(\mathbf{Q})$ is expressed using a similar n-mode representation as described above for the full potential.

Similar to case of the VCI calculations, there are also "zero" elements of the transition dipole matrix, corresponding to the symmetry forbidden transitions. Given the symmetry of each component of the dipole moment as well as the symmetry of each normal coordinates defined in the same molecular-fixed axes, the MULTIMODE will only evaluate the dipole matrix element according to the nonzero transitions.

Chapter 6.

Tunneling Splitting of Malonaldehyde
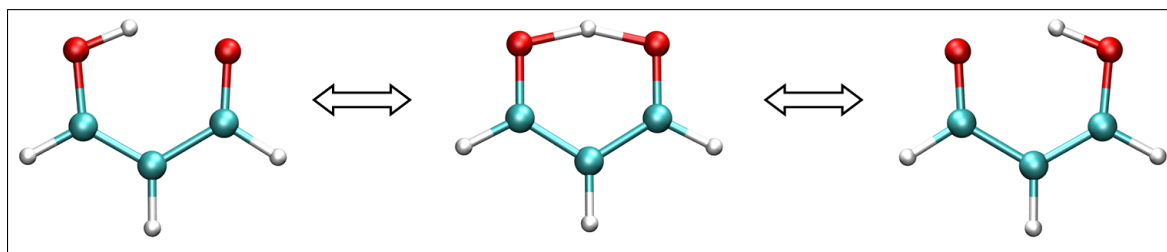
Figure 6.1. Global minimum structure (sides) and H-atom tunneling transition state structure (center) of Malonaldehyde.

In this chapter, we present full-dimensional quantum calculations of the ground vibrational state tunneling splitting of H-atom and D-atom transfer in malonaldehyde performed on a full-dimensional *ab initio* potential energy surface (PES). The two quantum approached, diffusion Monte Carlo method and vibrational configuration interaction calculations using the code MULTIMODE, have been discussed in detail in Chapter 4 and Chapter 5 respectively.

The PES is a fit to 11 147 near basis-set-limit frozen-core CCSD(T) electronic energies. This surface properly describes the invariance of the potential with respect to all permutations of identical atoms. The saddle-point barrier for the H-atom transfer on the PES is 4.1 kcal/mol, in excellent agreement with the reported *ab initio*

value. The tunneling splittings in full dimensionality are calculated using the unbiased "fixed-node" diffusion Monte Carlo (DMC) method in Cartesian and saddle-point normal coordinates. The ground-state tunneling splitting is found to be 21.6 cm^{-1} in Cartesian coordinates and 22.6 cm^{-1} in normal coordinates, with an uncertainty of 2-3 cm^{-1}. This splitting is also calculated based on a model which makes use of the exact single-well zero-point energy (ZPE) obtained with the MULTIMODE code and DMC ZPE and this calculation gives a tunneling splitting of 21-22 cm^{-1}. The corresponding computed splittings for the D-atom transfer are 3.0, 3.1, and 2-3 cm^{-1}. These calculated tunneling splittings agree with each other to within less than the standard uncertainties obtained with the DMC method used, which are between 2 and 3 cm^{-1}, and agree well with the experimental values of 21.6 and 2.9 =cm^{-1} for the H and D transfer, respectively.

Following a brief review of the importance and complexity of the tunneling calculations of H-transfer reaction of malonaldehyde in Section 6.1, a new PES based on very high level *ab initio* calculations are reported in Section 6.2. Results of full-dimensional calculations of the H and D-atom tunneling splittings from standard DMC calculations and MULTIMODE calculations are presented in Section 6.3. Lastly, we conclude this chapter with a summary and prospective.

6.1. Overview

The hydrogen-atom transfer in malonaldehyde is one of the most intensively studied intramolecular H-atom transfer processes in chemistry. This is an activated event that manifests itself spectroscopically as a splitting of the ground vibrational state of 21.58314 cm^{-1} for H-atom transfer [64, 65] and 2.915 cm^{-1} for D-atom transfer in the mono-deuterated malonaldehyde [66]. Part of the motivation and attraction in

considering malonaldehyde is that it is a fairly large molecule (21 vibrational degrees of freedom) and yet the H-atom transfer appears to be quite simple, i.e., a transfer between the two O atoms along a path connecting the two equivalent minima via a first order saddle point transition state all of which co-planar (see Figure 6.1). Thus the tunneling motion appears ideal for reduced dimensionality models, e.g., a reaction path model, which are used to model H-atom and proton-transfer in a wide variety of applications in chemistry and biochemistry.

Despite its apparent simplicity, the accurate calculation of the tunneling splitting in malonaldehyde has defied these reduced dimensionality models [67–70]. In some of these models the potential was obtained using *ab initio* methods that gave barrier heights in the range of 6-10 kcal/mol and the calculated tunneling splittings varied from roughly 60 cm^{-1} to values close to experiment. Even a fairly recent three-degree of freedom model for the H-atom transfer and an adiabatic treatment of the remaining 18 degrees of freedom reported by Thompson and co-workers[71], obtained a tunneling splitting of 21.8 cm^{-1}; however, with a saddle-point barrier height that is roughly 2.5 times the accurate value of 4.1 kcal/mol, according to high-level *ab initio* calculations reported here. A recent "direct-dynamics" semi-classical wavepacket calculation [72] using a reduced dimensionality tunneling path reported a tunneling splitting of 21 cm^{-1} in excellent agreement with experiment, with a (low) barrier of 2.3 kcal/mol; however, the authors argued that the relevant tunneling paths sampled other barriers of heights of roughly 12 kcal/mol. Very recent analysis [73] also shows the sensitivity of the splitting to the tunneling path, in particular the OO separation.

Clearly then this is a much more difficult problem than it appears at first glance. Recent theoretical work has been done in the full (21) dimensional vibrational space. Yagi *et al.*[74] reported a "Shepard interpolated" potential energy surface (PES) in full dimensionality using relatively low-level *ab initio* calculations, i.e., MP2/6-31G(d,p).

This PES has a barrier of 3.61 kcal/mol and was used in recent full-dimensional, semi-classical "instanton" calculations of the tunneling splitting by Mil'nikov *et al.*[75] The calculated H and D-atom splittings were 30.7 and 4.58 cm^{-1}, respectively. However, it was also noted that this PES has "... incorrect topology.. in the vicinity of the instanton"[75]. A more accurate *ab initio* treatment[75] was done along the instanton paths with the result that for the best estimate of the barrier height of 3.8 kcal/mol the tunneling splittings were calculated to be 21-22 and 3.0 cm^{-1}, in quite good agreement with experiment. A preliminary account of this more accurate *ab initio* instanton calculation appeared in 2003[76].

In the most recent report Viel *et al.*[77] reported "benchmark" Monte Carlo (MC) projection operator, imaginary time spectral evolution (POITSE) of the H and D-atom splitting using the Yagi *et al.* PES. The POITSE results were 25.7 ± 0.3 and 3.21 ± 0.09 cm^{-1} for H and D, respectively, which are 5 and 1.3 cm^{-1} lower than the instanton results and roughly roughly 20 percent larger than experiment for H-transfer but only 10 percent higher for D-transfer. This led Viel *et al.* to question the accuracy of the tunneling splittings obtained with the instanton method. Note that Multiconfiguration Time-Dependent Hartree calculations were also reported for the splittings in this paper.

An advantage of these POITSE calculations, which were performed in saddle-point normal coordinates with a projector given by the imaginary normal mode, is that statistical uncertainty is smaller than the one obtained in a standard Diffusion MC (DMC) calculation. However, in order to perform the POITSE calculations the vibrational angular momentum terms in the Hamiltonian were neglected, leading these calculations to have an unknown, but assumed very small, systematic error due to this approximation. Thus, while significant progress has been made quite recently in treating this "simple" H-atom transfer theoretically, the correct answer, obtained

with an exact treatment of the nuclear dynamics and using an accurate PES, has still eluded theory.

6.2. Potential Energy Surface

6.2.1. Ab initio method

First of all, our approaches require an accurate full-dimensional PES, which in turn depends on high-level electronic structure calculations. Thus, we started with benchmark frozen core CCSD(T)/aug-cc-pV5Z single point calculations at frozen core CCSD(T)/aug-cc-pVTZ optimized C_s and C_{2v} structures shown in Figure 6.1. The predicted barrier is 4.09 kcal/mol, 0.2 kcal/mol higher than that computed using an aug-cc-pVTZ basis, 0.5 kcal/mol higher than the MP2/6-31G(d,p) calculations used for the PES of Yagi and 1.2 kcal/mol higher than that predicted using density functional theory with the B3LYP functional. It is therefore clear that an accurate PES will only be obtained if the electronic structure method used is able to properly describe the effects of electron correlation. To compute the final, highly accurate potential energy points for the fitting procedure, we use the following additivity scheme to approach the basis set limit frozen core CCSD(T) energies:

$$E = E_{\text{HF}}/\text{A} + E_{\text{MP2}}^{\text{corr}}/\text{B} + \Delta E_{\text{CCSD(T)}-\text{MP2}}^{\text{corr}}/\text{C}, \qquad (6.1)$$

where A, B and C are basis sets. The HF calculations were performed with A = QZVPP,using the TURBOMOLE package [78]. The MP2 correlation energies were computed using the MP2-F12 method, as programmed in the RI-CC2 module of TURBOMOLE [79–81]. This method yields near basis set limit correlation energies by employing a combined orbital and geminal basis. The QZVPP basis was used

for the orbital basis and a linear combination of six Gaussians, fitted to an exponential [82] with exponent 1.4 a_0^{-1}, was used as the geminal correlation factor. The amplitudes for the germinal contributions were fixed according to the s and p cusp conditions [83]. The technical details of the RI-MP2-F12 calculations are: ansatz 2, approximation [84, 85]; CABS=aug-cc-pVTZ (Coulomb basis) [86, 87]; RI=aug-cc-pV5Z (Coulomb basis) [88]. The CCSD(T) calculations were performed using the MOL-PRO program [11], with C = aug′-cc-pVTZ [35, 89], where the prime indicates that only augmentation functions on the oxygen atoms are included.

The E_{HF}, $E_{\text{MP2}}^{\text{corr}}$ and $\Delta E_{\text{CCSD(T)}-\text{MP2}}^{\text{corr}}$ contributions to the barrier to hydrogen transfer for our method, computed at the aug-cc-pVTZ structures, are collected in Table 6.1 and are compared to CCSD(T)/aug-cc-pVXZ values with X = T, Q and 5. Each contribution to the barrier used for our surface is within 10 cm^{-1} of the basis set limit. The final deviation from the basis set limit frozen core CCSD(T) barrier is approximately 0.05 kcal/mol, which is almost certainly less than the error incurred by neglecting further correlation energy contributions and non-adiabatic and relativistic effects.

Table 6.1. HF and MP2 and ΔCCSD(T) correlation contributions to the barrier height of the H-atom transfer reaction (kcal/mol).

Basis	E_{HF}	E_{MP2}	$\Delta E_{\text{CCSD(T)}}^{corr}$	Total
aug-cc-pVTZ	9.17	-6.49[a]	1.21	3.89
aug-cc-pVQZ	9.34	-6.56	1.24	4.02
aug-cc-pV5Z	9.36	-6.50	1.23	4.09
E	9.37	-6.55	1.21	4.04[b]

[a] The MP2/aug-cc-pVTZ barrier is 2.68 kcal/mol and the MP2/6-31G(d,p) PES of Ref. [74] is 3.62 kcal/mol. [b] Energy from Eq.(6.1) in the text.

6.2.2. Fitting

On the basis of fitting procedure described in Chapter 2, the final full-dimensional malonaldehyde potential energy surface (PES) is a weighted least squares fit to 11 147 highly accurate *ab initio* energies obtained using the theory and basis decribed above at configurations concentrated in the vicinity of the hydrogen atom transfer reaction path. This small set of configurations was selected from a set of roughly 42 000 configurations used in preliminary DFT-based PESs. The smaller set of configurations was chosen to distribute the energies fairly uniformly, as shown in Figure 6.2, and to eliminate overlap of configurations with approximately the same energy. After some "experimentation" with the DFT-based PESs the small final set of configurations was determined for the high-level *ab initio* calculations.
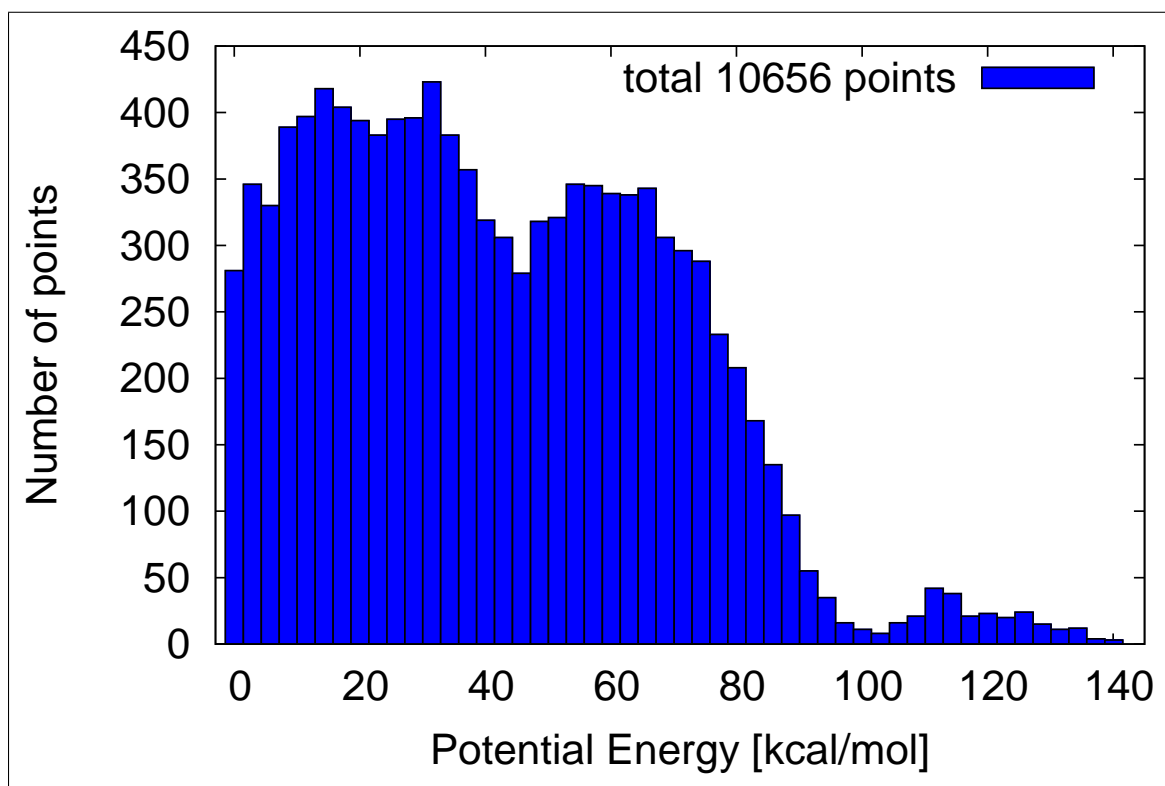
Figure 6.2. Distribution of *ab initio* energies vs the energy in units of kcal/mol relative to the global minimum below 143 kcal/mol. An additional 491 energies above 143 kcal/mol were included in the fit.

Some more details about the fitting basis functions. That is, the PES is represented using a many-body expansion of Morse-type invariant polynomials. The maximum degree of the two-body terms was set to 5, and 4 for the full nine-body terms. Thus, there are 1 597 free coefficients in the nine-body terms and 36 in the two-body terms, which together make a total of 1 633 free coefficients for the fitting basis. In addition, we used only for the two-body terms a cut-off function, $q(x) = (\max(0, 1 - x))^3$, that goes to 0 smoothly as the argument approaches 1. We let $x = r(i, j)/a$, where $r(i, j)$ is the internuclear distance between atom i and atom j, and the parameter a was fixed at 9 bohrs. The rms fitting error is 32 cm^{-1} (0.09 kcal/mol) for energies below 2000 cm^{-1} (5.7 kcal/mol) (relative to the global minimum) and grows to 211 cm^{-1} for energies up to 20 000 cm^{-1}.

The global minimum as well as the H-transfer saddle-point transition state were located on the potential energy surface. The comparison of the structures with experimental data [90] or present CCSD(T)/aug-cc-pVTZ and B3LYP/6-31+G(d) calculations is given in Table 6.2. As seen there is very good agreement between the PES and experimental values for the minimum and also between the PES and the CCSD(T) and DFT values at the minimum and the saddle point. The harmonic frequencies in ascending value and ZPE obtained from the potential energy surface, are reported in Table 6.3 along with results from present CCSD(T)/aug-cc-pVTZ and B3LYP/6-31+G(d) calculations. Again there is remarkably good agreement between the various levels of theory. The mean absolute deviation of the PES results from the CCSD(T)/aug-cc-pVTZ ones is 13.7 cm^{-1} for the minimum and 19.6 cm^{-1} for the TS. DFT performs surprisingly well for the frequencies considering the fact that the barrier height is too low by some 30%. We also note that the present DFT results agree well with the those reported previously by Barone and Adamo [91].

Table 6.2. Geometries of stationary points for malonaldehyde (Å and degree).

	MIN				TS		
	Expt.[a]	PES	CCSD(T)[b]	B3LYP[c]	PES	CCSD(T)[b]	B3LYP[c]
O=C	1.234	1.233	1.240	1.245	1.276	1.282	1.284
O−C	1.320	1.323	1.328	1.324			
C=C	1.348	1.359	1.363	1.368	1.398	1.400	1.402
C−C	1.454	1.445	1.445	1.440			
C_2-H_7	1.089	1.083	1.085	1.088	1.089	1.092	1.094
C_3-H_8	1.091	1.078	1.080	1.084	1.078	1.079	1.083
C_4-H_9	1.094	1.099	1.101	1.104			
O−H	0.969	0.985	0.993	1.002			
O···O	2.553(2.574)	2.588	2.587	2.607	2.362	2.364	2.378
O···H	1.68	1.708	1.694	1.720	1.205	1.205	1.216
O−C=C	124.5	124.3	124.2	124.4	121.7	121.7	121.7
C=C−C	119.4	119.7	119.6	120.0	116.1	116.1	116.4
C−C=O	123.0	123.3	123.3	123.4			
C−O−H	106.3	106.2	105.7	106.8	101.7	101.5	102.3
O−H···O	147.6(146.9)	146.5	147.5	145.3	157.0	157.6	155.7
$C=C-H_7$	122.3	122.0	122.4	122.6	121.1	121.4	121.6
$C=C-H_8$	—	120.1	120.0	119.8	121.9	122.0	121.8
$C-C-H_9$	117.6	117.5	117.6	117.7			

[a] From Ref. [90]; [b] frozen core aug-cc-pVTZ calculations; [c] 6-31+G(d) calculations

Table 6.3. Harmonic frequencies (cm^{-1}) and zero-point energies (ZPE) of the global minimum and the transition state from the potential energy surface and B3LYP/6-31+G(d) calculations.

Mode	PES MIN	PES TS	CCSD(T)/APVTZ MIN	CCSD(T)/APVTZ TS	B3LYP/6-31+G(d) MIN	B3LYP/6-31+G(d) TS
1	268.6	i1253.0	252.9	i1300.7	285.3	i1253.6
2	295.4	346.3	283.3	362.4	287.9	370.9
3	383.2	393.4	373.8	373.2	397.0	393.0
4	522.1	573.0	504.2	566.3	516.3	574.3
5	760.6	608.8	780.6	625.1	787.1	603.3
6	888.3	750.2	887.5	768.3	892.4	780.9
7	897.4	957.9	899.1	941.9	910.7	940.9
8	995.7	995.2	992.9	983.2	1005.8	983.9
9	998.0	998.2	1004.1	1044.4	1010.4	1043.0
10	1023.1	1073.8	1032.3	1064.0	1042.1	1065.3
11	1105.4	1101.4	1102.2	1101.0	1122.8	1119.0
12	1280.8	1322.0	1276.2	1303.9	1295.1	1263.7
13	1393.6	1340.4	1403.1	1327.2	1403.5	1339.4
14	1419.5	1405.1	1409.9	1366.8	1412.1	1377.0
15	1490.2	1472.5	1473.2	1499.8	1486.9	1511.9
16	1647.2	1617.7	1636.0	1630.4	1632.5	1622.3
17	1713.5	1620.1	1698.3	1637.4	1707.8	1646.3
18	3020.7	1893.7	3009.1	1887.8	3008.9	1859.3
19	3196.8	3126.9	3183.3	3111.5	3158.1	3124.4
20	3251.4	3141.4	3236.9	3112.2	3212.0	3124.6
21	3348.9	3227.5	3266.4	3252.2	3233.4	3251.0
H.O. ZPE	14950.2		14852.5		14904.0	

6.3. Tunneling Splitting Calculations

6.3.1. Calculations using DMC

In DMC calculations of the ground vibrational state, the full-dimensional wave functions were represented by an ensemble of roughly 10 000 equally weighted random walkers, which were propagated in both Cartesian space and saddle-point normal mode space. The vibrational energy was then calculated by averaging the reference energy, E_{ref}, over 80 000 steps after an equilibrium stage of 2000 steps at a time step of 10 a.u.. The CPU time for this DMC calculation is about 4 days on an Operton 2.3 GHz Linux compute node. The time dependence of E_{ref} of a typical DMC trajectory in Cartesian coordinates is presented in Figure 6.3 for 5000 time steps at the very beginning of the trajectory. The fluctuations of E_{ref} after the equilibrium stage of 2000 steps are still large, but symmetrically distributed around $\langle E_{\mathrm{ref}} \rangle$, i.e., the average of the reference energy over 80 000 steps. In normal coordinates, the fluctuations in E_{ref} are very similar to their Cartesian analog and so we don't show them. The finite time step size was chosen short enough to keep the systematic error small but without increasing too much statistical error due to the increased correlation between the successive distributions of random walkers. The value of the time step we used for malonaldehyde calculations is consistent with the vaule used in many previous DMC studies for other molecules [15, 92].

The ground state energy of malonaldehyde was determined to be 14 677.9 cm^{-1} from DMC simulations in Cartesian coordinates, and 14 678.3 cm^{-1} in normal coordinates, which is roughly 270 cm^{-1} lower than the harmonic value. The statistical uncertainty in both of these calculations was calculated using two methods, i.e. a standard correlation time analysis method and the blocking method. The normalized autocorrelation function for a typical DMC calculation is shown in the upper plot
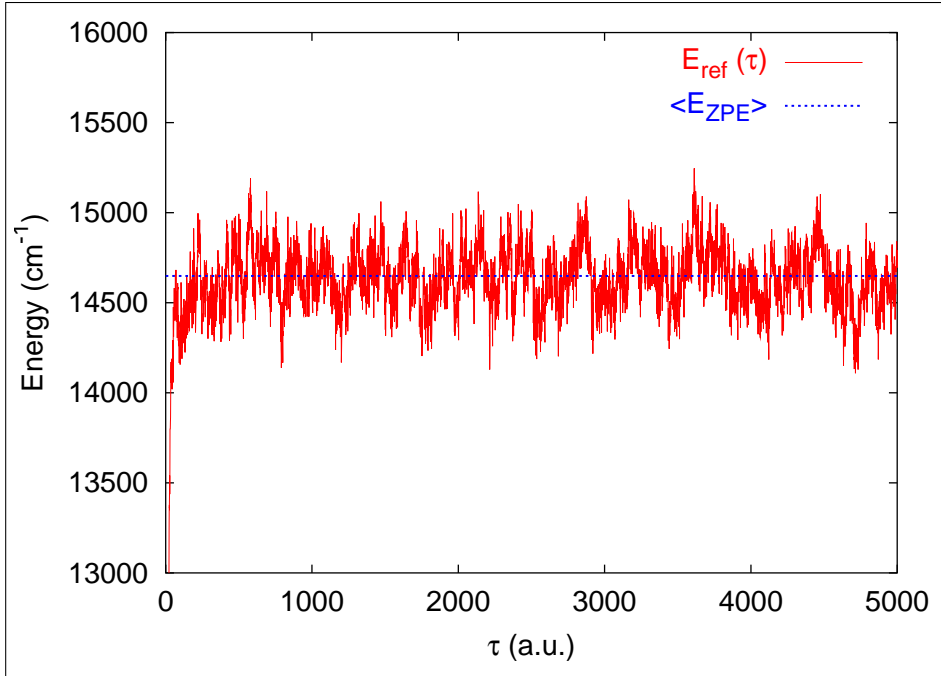
Figure 6.3. Energy fluctuations of a single DMC trajectory in Cartesian coordinates initially at the saddle point. $\langle E_{\mathrm{ZPE}} \rangle$ is the average value of E_{ref} over the last 80 000 DMC time steps indicated with dotted line.

of Figure 6.4. Using Eq. (4.28) the autocorrelation time was estimated to be 23.1 time steps, i.e. 231 a.u. of time. The statistical uncertainty was then determined to be 2.6 cm^{-1} from Eq. (4.27) with $\sigma_{\overline{\mathcal{O}}}^2 = 0.29$ cm^{-2} per time step. Additionally, the statistical uncertainty was calculated using the blocking method and the values of error is shown in the lower plot of Figure 6.4 as a function of the blocking length k from 0 to 500 time steps. We note that the estimated values of statistical uncertainty obtained using the blocking method are not converged with the increasing blocking length, but start to fluctuate about an average value. The fluctuations are due to the use of a finite number of DMC data. Averaging over the last 250 time steps, the average value was estimated to be about 2.46 cm^{-1}, which agrees quite well with the value of statistical error of 2.6 cm^{-1} obtained using correlation time analysis. The estimation of uncertainty we made for malonaldehyde is about the same order of uncertainty in previous standard DMC studies for CH_5^+ [92] and H_5^+ [15]. Within this

uncertainty the ZPEs in Cartesian and normal-coordinates (without the vibrational angular momentum terms in the kinetic energy operator) are in excellent agreement, strongly suggesting that the error made in the normal coordinate calculation is of the order of one cm^{-1} or less.

Fixed-node DMC calculations were performed for the first excited state with elimination of random walkers that crossed the node. Based on symmetry considerations the nodal surface for the first excited state wave function of malonaldehyde can be easily constructed in both coordinates. In Cartesian coordinates, the node is placed where the transferring H-atom is equidistant from the two oxygens, i.e. $r_{HO} = r_{HO'}$. In normal coordinates the nodal plane is Q_{im}=0, where Q_{im} is the saddle point imaginary frequency mass-scaled normal mode. Due to use of finite time steps, we included the recrossing correction in fixed-node DMC simulations for higher accuracy, given by Anderson.[49] These two nodal surfaces are obviously tangent to each, however, they not identical. By doing both sets of calculations the robustness of the final results can hopefully be made, subject to a determination of the accuracy of the approximate normal-coordinate approach as determined by the accuracy of the ZPE.

The final energy for the excited state is then an average energy of two sets of DMC simulations with walkers initially distributed on each side of the node. (The energies on both sides of node agree to within the statistical uncertainties in the calculation.) By calculating the energy difference of the two vibrational states, the tunneling splitting is found to be 21.6 cm^{-1} in Cartesian coordinates and 22.6 cm^{-1} in normal coordinates which are the same within the statistical uncertainties of each calculation. Both values are in excellent agreement with the experimental value of 21.6 cm^{-1}. Applying the same computational procedure, the tunneling splitting of D-atom transfer was determined to be 3.0 cm^{-1} in Cartesian coordinates and 3.1 cm^{-1} in normal coordinates with an uncertainty of roughly 2-3 cm^{-1} for each. Despite this

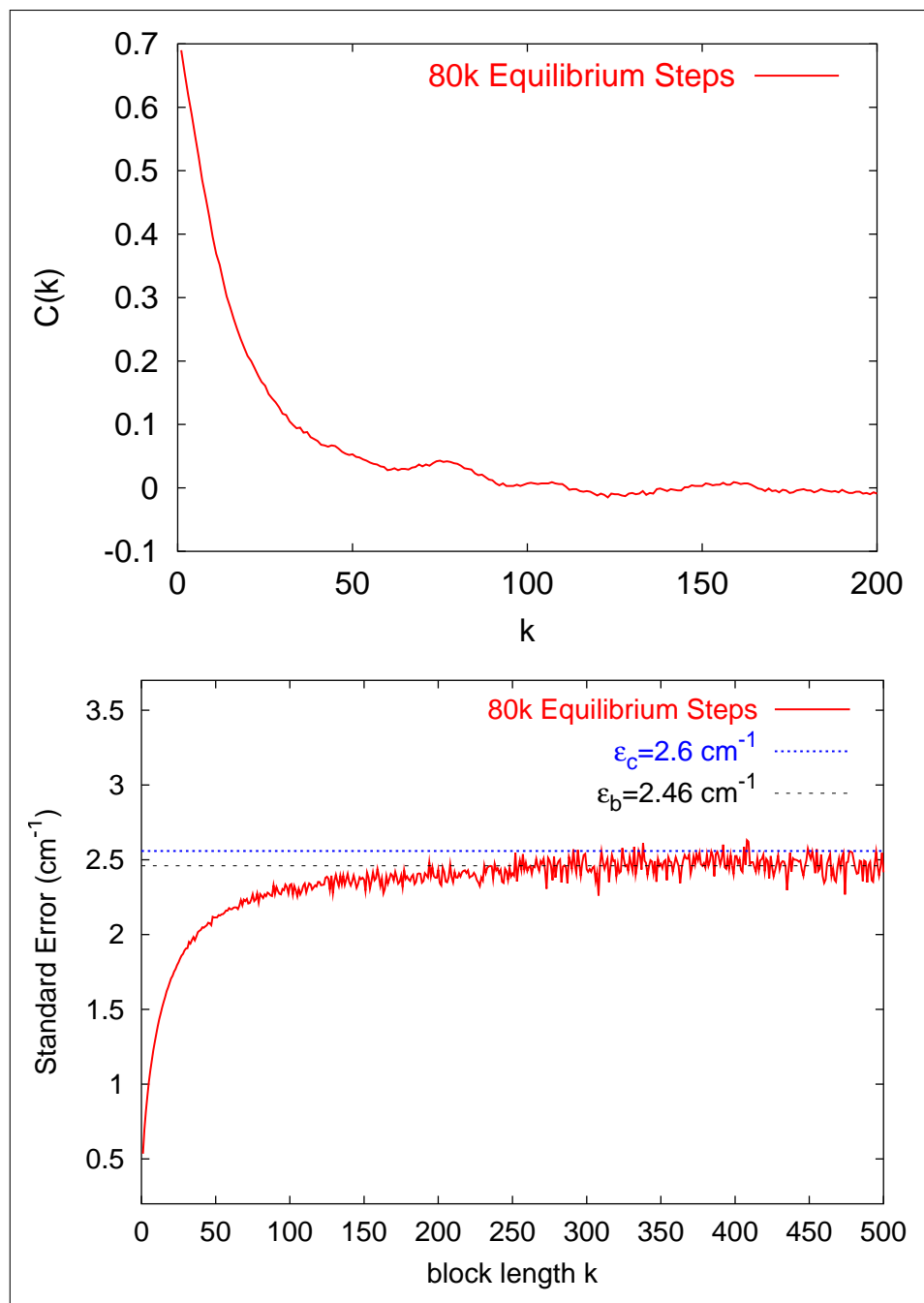**Figure 6.4.** Autocorrelation function shown with a solid line in the upper plot. Statistical uncertainties obtained using the blocking method with a solid line and the long dashed line gives the average value of uncertainties, ε_b, in the last 250 time steps, and the value obtained by a standard correlation time analysis, ε_c, indicated as a straight dotted line in the lower plot.

relatively large uncertainty the values obtained from the two independent calculations are in very good agreement with the experimental splitting of 2.915 cm^{-1}.

It also appears safe to conclude that the systematic error introduced by the approximate normal-coordinate Hamiltonian is less than the statistical uncertainty of 2-3 cm$^-$1 made in the present DMC calculations. In the following subsection we provide another independent estimate of this error that puts it between 1 and 2 cm$^-$1. This is larger than the 0.3 cm-1 statistical uncertainty of the POITSE calculations of the splitting reported by Viel *et al.* [77]; however, it doesn't absolutely rule out that error estimate as being correct since some cancellation of the systematic error in doing energy differences is quite likely.

6.3.2. Calculations using Multimode

A third and very different approach to obtain the tunneling splitting was done with the code Multimode. The global minimum was used as a reference geometry and potential grids were calculated along its normal modes. Detailed convergence studies of the zero-point energy of both malonaldehyde and the mono-deterated malonaldehyde are presented in Table 6.4 with respect to the increasing n in the hierarchical representation of potential, as well as the increasing size of the CI basis. The largest Multimode calculation reported in Table 6.4 took roughly 7 days on a single Operton 2.3 GHz Linux compute node. Based on an examination of the convergence properties of this ZPE with respect to the mode representation and the basis size, extrapolated estimates of the energies are 0.9 and 0.8 cm^{-1} below the higher-level value of 14 689.2 and 13 963.8 cm^{-1} for H and D-transfer, respectively. Additionally, by doing VCI calculations with and without vibrational angular momentum coupling terms, the error of the calculations of the ZPE using the approximate Hamiltonian

given by Eq. (4.20) was estimated to be about 1.2 cm^{-1}, consistent with the estimate given in the previous subsection.

Table 6.4. Convergence of zero point energy (cm^{-1}) of malonaldehyde and mono-deterated malonaldehyde (in italics) obtained with the code MULTIMODE using the minimum as the reference geometry. The sizes of the C$_s$ symmetry-bloc Hamiltonian matrices corresponding the "MAXSUM" parameters are given as footnotes for the 4MR and 5MR calculations (they are smaller for 3MR calculations) except for MAXSUM=7.

MAXSUM	3[a]	4[b]	5[c]	6[d]	7[e]
3MR	14709.8	14687.4	14680.3	14677.5	14676.4
	13979.7	*13962.1*	*13956.9*	*13954.9*	*13954.1*
4MR	14718.2	14698.4	14691.9	14689.2	—
	13985.8	*13970.2*	*13965.7*	*13963.8*	—
5MR	14717.6	14697.8	—	—	—
	13985.3	*13969.7*	—	—	—

[a] 1150, 872; [b] 3903, 2762; [c] 24603, 20828; [d] 65914, 53738; [e] 37924, 19184.

The calculated VCI ZPE, which is referenced to the global minimum and which uses a basis centered there, should be largely unaffected by the tunneling. Based on a simple two-state model this ZPE should exceed the "exact" ZPE, obtained by the DMC calculations in Cartesian coordinates, by half the tunneling splitting. Using extrapolated VCI ZPEs of 14 688.3 and 13 963.0 cm^{-1} for H and D-transfer, with the corresponding values of 14 677.9 and 13 961.7 cm^{-1} from the DMC calculations in Cartesian coordinates we obtain tunneling splittings of 20.8 and 2.6 cm^{-1} with uncertainties of $\pm$ 2-3 cm^{-1}, for H and D-transfer in excellent agreement with the two DMC results and all in agreement with experiment to within the statistical uncertainties.

6.4. Summary and Conclusions

We reported a full-dimensional, permutationally invariant potential energy surface for malonaldehyde based on 11 147 extrapolated high level *ab initio* electronic energies. This PES was used in two sets of Diffusion Monte Carlo calculations of the ground state tunneling splitting for H and D-atom transfer and also in a third model calculation of these splittings using the code MULTIMODE. The splittings obtained from these three calculations are in remarkable agreement with each other in giving values of 21-22 cm^{-1}. for the H atom splitting and 2-3 cm^{-1}. for the D-atom. These values are well within the estimated statistical uncertainty of $\pm$ 2-3 cm^{-1} and in excellent agreement with experiment.

Uncertainties in DMC calculations of the order reported here are difficult to reduce. Thus we are continuing with very different sets of calculations based on the "Reaction Path Hamiltonian" for which preliminary results using very approximate potential energy surfaces have already been reported [93–95]. These are challenging calculations and new strategies are being explored and results are expected in the near future.

Chapter 7.

Infrared Spectrum of H_5^+ and D_5^+

In this chapter, infrared spectra of the highly fluxional cations H_5^+ and D_5^+ have been calculated using full-dimensional quantum approaches described in precedent chapters. These cations have been postulated to exist in the interstellar medium and to play a central role in the deuterium fractionation. The calculated spectra make use of an *ab initio* potential energy surface and a new dipole moment surface and are based on results from fixed-node quantum diffusion Monte Carlo and variational vibrational calculations. Comparison has been made with experimental measurements. The successful assignment of the experimental spectra requires a proper treatment of the delocalized anharmonic shared-proton mode and indicates a major breakdown of the harmonic approximation. Several calculated intense spectral features associated with this mode in the far-infrared region could guide future observational searches of these cations.

7.1. Overview

With the observation of H_3^+ in the interstellar medium (ISM) [96, 97], aided greatly by theory [98], the reactions of this cation and its deuterated isotopologues with molecular hydrogen and its deuterated isotopologues are believed to play central roles in the deuterium fractionation in the ISM [99–102]. Since H_5^+ and its deuterated analogues are stable species, the spectroscopic detection of these cations in the ISM should be possible and would be of primary importance. This cannot be done in the absence of laboratory-based or predictive calculated spectra. A low-resolution action spectrum [103] of H_5^+ published in 1 988 reported three broad features at 3 532, 3 910, and 4 230 cm^{-1}. These features, especially the last one, were interpreted cautiously in viewof the (correctly) suspected highly fluxional nature of the vibrations based on *ab initio* calculations of scaled harmonic frequencies and intensities [104].

The highly fluxional nature of the ground vibrational state of H_5^+ and all of the deuterated isotopologues has been established from recent rigorous quantum diffusion Monte Carlo (DMC) calculations [15, 105] using a high-quality ab-initiobased potential energy surface (PES) that is invariant with respect to the 5! permutations of the H atoms [15]. An approximate anharmonic treatment of the vibrational modes also emphasizes the highly anharmonic character of these vibrations [106].

The combination of this highly anharmonic shared-proton mode plus the highly fluxional nature of the H_5^+ cation make exact quantum calculations of the IR spectrum unfeasible. Thus, our approach is to use state-of-the-artmethods to obtain the infrared (IR) spectra of H_5^+ and D_5^+ reported here. These are compared with new and improved photodissociation spectra, which also report new bands for H_5^+ and the first spectra for D_5^+
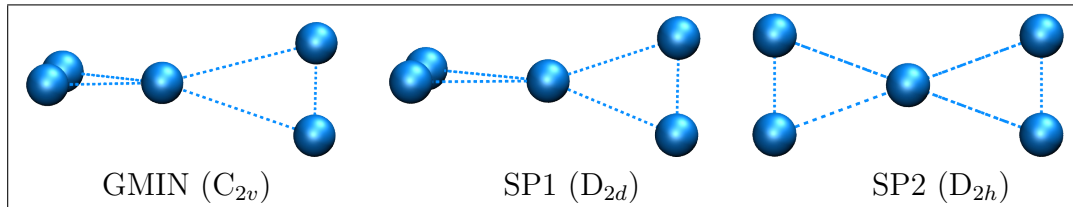
7.2. Potentials and Dipole Moments

Figure 7.1. Global minimum structure of C_{2v} symmetry, first order saddle point of D_{2d} symmetry, and second-order saddle point of D_{2h} symmetry.

The calculations reported here make use of an *ab initio* PES [15], which was fitted to $105\,888$ CCSD(T)/aug-cc-pVTZ *ab initio* energies using a many-body expansion of Morse-type invariant polynomials. The maximum power for the two-body terms is 8, 7 for the three-body terms, and 5 for the full five-body terms. This PES has full permutational symmetry with respect to interchange of H atoms and dissociates to H_3^+ and H_2. The functional form used here for the various n-body terms is the product of a polynomial and a damping function $d(\mathbf{R})$,

$$d(\mathbf{R}) = \max\left(0,\ 1 - \frac{\|\mathbf{R}\|_2}{a \cdot \sqrt{n}}\right)^5, \tag{7.1}$$

where $\mathbf{R}$ denotes the internuclear distance vector and n is the number of internuclear distances, and a is a constant. This constant is adjusted to give smooth asymptotic behavior. In the present case a is equal to 7.0 bohr. Three low-lying stationary points located on the H_5^+ PES are shown graphically in Figure 7.1.

We also employ a new full-dimensional dipole moment surface (DMS) that is a fit to roughly $5\,000$ dipole moment values obtained using density functional theory with the B3LYP functional and the aug-cc-pVTZ basis using the code MOLPRO [11]. Among the $5\,000$ data points, $3\,874$ of them were used in the complex region, and the remaining $1\,000$ data points for fragments H_3^+ and H_2. For these fragment data separate calculations were done for H_3^+ and H_2 (the H_2 dipole is zero, of course), and

the H$_5^+$ configuration was created by placing the two fragments in random relative orientation and at a variable distance not less than 5 bohr. The DMS is represented in the form of a model of effective charges at the locations of the 5 nuclei. The 5 effective charges are functions of the complete set of internuclear distances, fitted to reproduce the *ab initio* dipole moment and to satisfy the condition that the total charge is +1. The functional form of the charges is covariant under permutation of identical nuclei; under interchange of nuclei i and j, the effective charges on those nuclei are likewise interchanged. However, the validity of the model is restricted to the complex region and the region of small separation between fragments H$_3^+$ and H$_2$; at large separation there will be fractional charges on the two fragments: charge 0.6 on the H$_3$ and charge 0.4 on the H$_2$ fragment. The root mean square fitting error for the dipole moment is 1.46e-3 a.u. for the subset of configurations that have energy up to 0.02 hartree above the global min and it is 3.83 a.u. for the subset of configurations that have energy in the range 0.02-0.04 Hartree above the global minimum.

7.3. Symmetry of the Ground State Wavefunction

The previous DMC calculations of the ground vibrational state showed a highly symmetric wave function [105], which has maximum amplitude at the saddle point configuration (of D$_{2d}$ symmetry) which is only 52 cm^{-1} above two equivalent minima (of C$_{2v}$ symmetry). This indicates both delocalization of the wave function and the singular importance of this saddle point instead of the global minimum as the configuration of most relevance. With that in mind, we show the relaxed potential as a function of the imaginary frequency normal mode of this saddle point, which spans both minima, and the corresponding one-dimensional ground-state quantum density in Figure 7.2. As seen, the density maximum is at the saddle point configuration, in accord with the results of full-dimensional DMC calculations. Clearly, this wave

function is determined by a highly nonharmonic double well of this potential. The energy of this approximate 1d ground vibrational state is also indicated in the figure, and as expected, it is well above the saddle point energy. On the basis of these results, a standard harmonic analysis done at the global minimum would obviously be unrealistic.
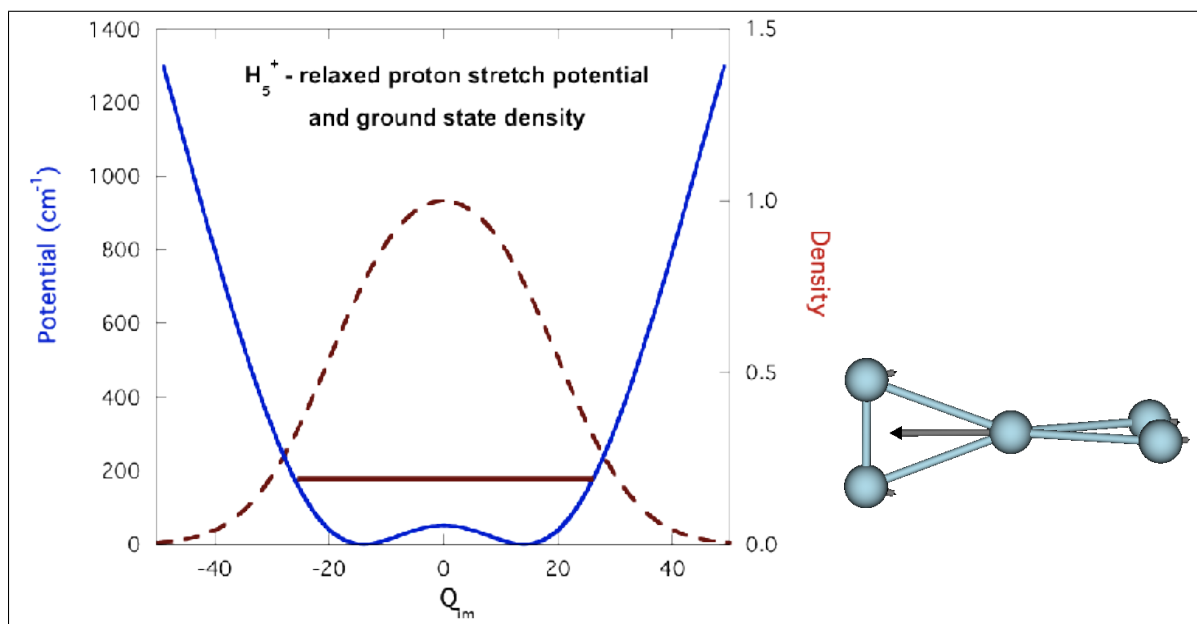

Figure 7.2. Relaxed potential along the imaginary frequency mode of the D$_{2d}$ saddle point and corresponding ground-state vibrational density.

The normal-mode eigenvectors and frequencies of the global minimum, first-order saddle point of D$_{2d}$ symmetry and another second-order saddle point of D$_{2h}$ symmetry are given in the Table 7.1. For computational convenience, the variational calculations, described in Section 7.5, are referenced to the D$_{2h}$ saddle point, and thus, mode assignments made below are based on those saddle point modes. The components of the dipole moment along the five IR-active D$_{2h}$ saddle point normal modes are plotted in the Figure 7.3. The choice of coordinate system has the x-axis connecting the centers of mass of the two H$_2$ units and passing through the central proton. Thus the imaginary frequency normal mode has only an x-component and its dipole, shown in the upper left panel, shows the largest variation with x, indicating that transitions

involving that mode should have large intensities. Note the HH-stretch, mode 8, with harmonic frequency $3\,898$ cm^{-1}, shows the next largest variation of the dipole.

On the basis of the above, it is clear that H_5^+ is another, and indeed the smallest, example of a proton-bridged dimer complex. The shared-proton coordinate in such dimers provides direct access to the intermolecular potential corresponding to shared-proton reactions. Vibrational spectra of these dimers generally contain complex band patterns that cannot be reproduced by harmonic theory [107–112], but anharmonic treatments have been successful in some systems [111, 112].
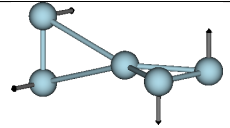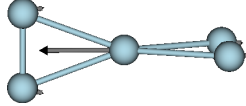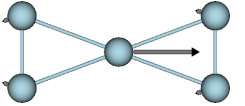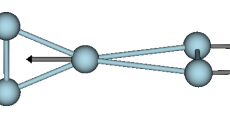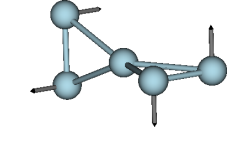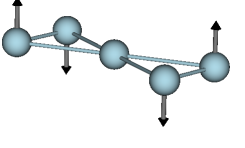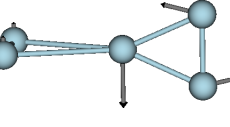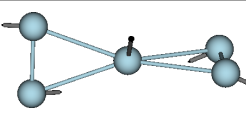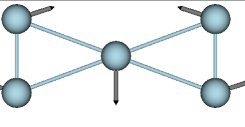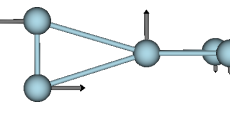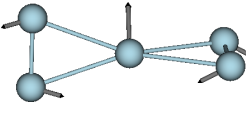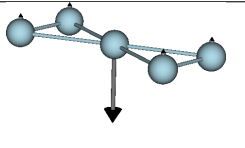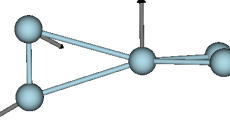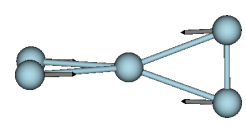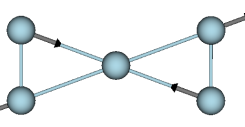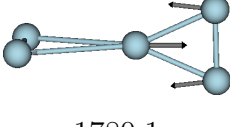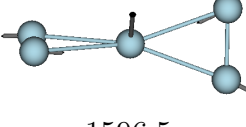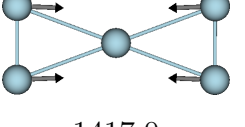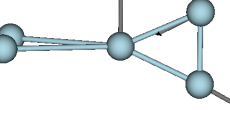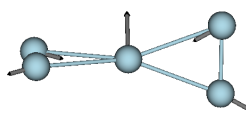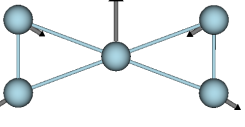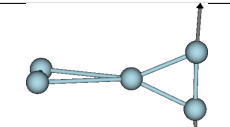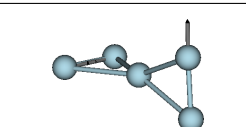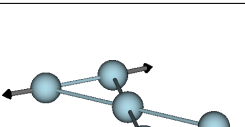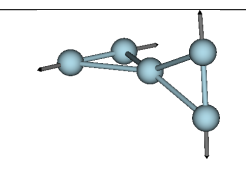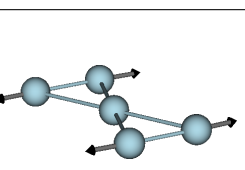
7.4. Diffusion Monte Carlo

Benchmark calculations for the ground vibrational state of H_5^+ are provided by standard DMC calculations, which are exact (within statistical uncertainties). In addition, fixed-node DMC calculations can give accurate energies of low-lying fundamental energies.

7.4.1. Setup

In the present DMC calculations energies were obtained using an ensemble of 20 000 Gaussian random walkers. After equilibrating, which typically took 2 000 time steps, propagation continued for an additional 80 000 steps. The zero-point energy (ZPE) is calculated using the standard expression given in Chapter 4. The total number of walkers is kept approximately constant by the feedback parameter α which is adjustable but which is essentially the inverse of the time step. In the present calculations α equals 0.1 a.u.

Table 7.1. Normal mode eigenvectors and frequencies (cm^{-1}) at the global minimum, denoted MIN, and two proton-transfer saddle points, denoted SP1 and SP2.

	MIN-C_{2v}	SP1-D_{2d}	SP2-D_{2h}
Mode 1	206.0	476.7i	543.2i
Mode 2	477.1	230.8	231.8i
Mode 3	823.4	960.8	898.7
Mode 4	878.5	960.8	1139.3
Mode 5	1196.6	1407.2	1307.3
Mode 6	1780.1	1596.5	1417.0
Mode 7	2079.2	1596.5	1744.4
Mode 8	3680.6	3890.2	3897.5
Mode 9	4096.9	3965.0	3982.2
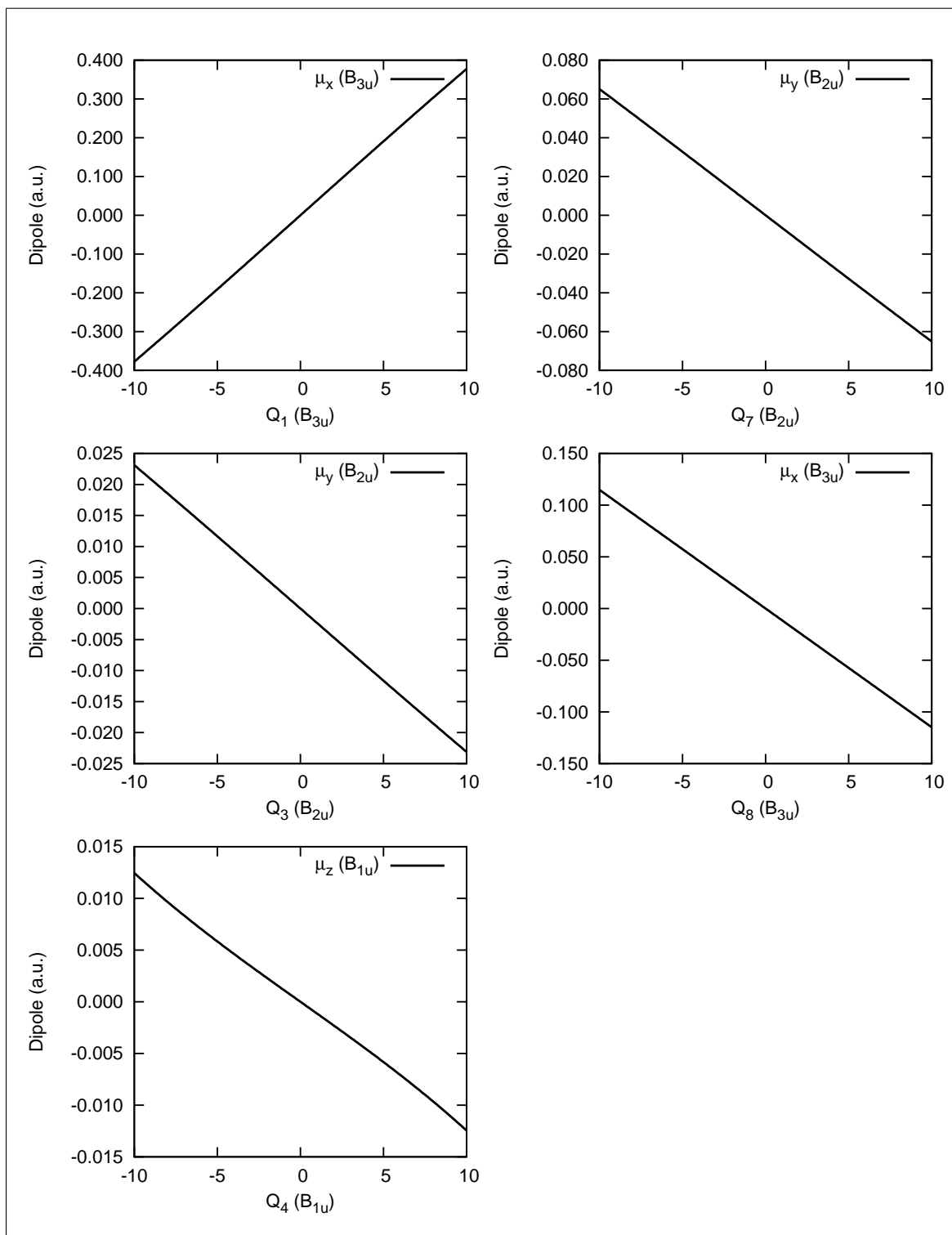
Figure 7.3. Cuts of the dipole moment components along the D_{2h} saddle point "IR active" normal modes. Q_1 is the imaginary frequency proton-transfer mode.

To extend the DMC approach for excited states, fixed-node DMC calculations[49, 113] were performed as above with the addition of a nodal surface which forces a node in the wave-function by eliminating walkers that cross the surface. A standard re-crossing correction was also applied to account for the probability of recrossing in a finite (imaginary) time step. [49] Since the DMC procedure for excited states have been discussed in detail in Chapter 4, here we focus on the definitions of the nodal surfaces.

In the present application for the first excited proton-stretch state the node was placed (in Cartesian coordinates) at the midpoint of a vector defined by the centers of mass of the two H_2 units, shown in Figure 7.1. Note this nodal surface assumes that the initial "interior" H atom maintains that position. Calculations for the (nodeless) ZPE indicate that this is the case for quite long propagation times; however, at some point an exchange does occur. Thus for the case with the shared-proton node indicated above the DMC trajectory does yield an energy above the ZPE for quite long times but eventually, due the exchange this energy relaxes to the ZPE. To prevent this from happening an additional "exchange node" was introduced. Specifically we remove any random walker which has the label of its central hydrogen changed in two successive steps. (The central hydrogen is defined as the hydrogen with the shortest distance to the COM of the molecule.) With this node the label of the central hydrogen remains unchanged for the whole ensemble. A recalculation of the ZPE with this exchange node produced identical results to within the statistical uncertainty, as expected.

This exchange node was also used in a separate calculation of the splitting due to torsional motion of the two H_2 units. In this calculation a nodal surface was place at a torsional angle, θ, of 180 degree (see Figure 7.4). In Cartesian coordinates *theta* is the angle between the two H-H vectors projected onto the plane perpendicular to

the axis passing through the COMs of the two H$_2$. A plot of the torsional potential along a "minimum energy path" is shown below.
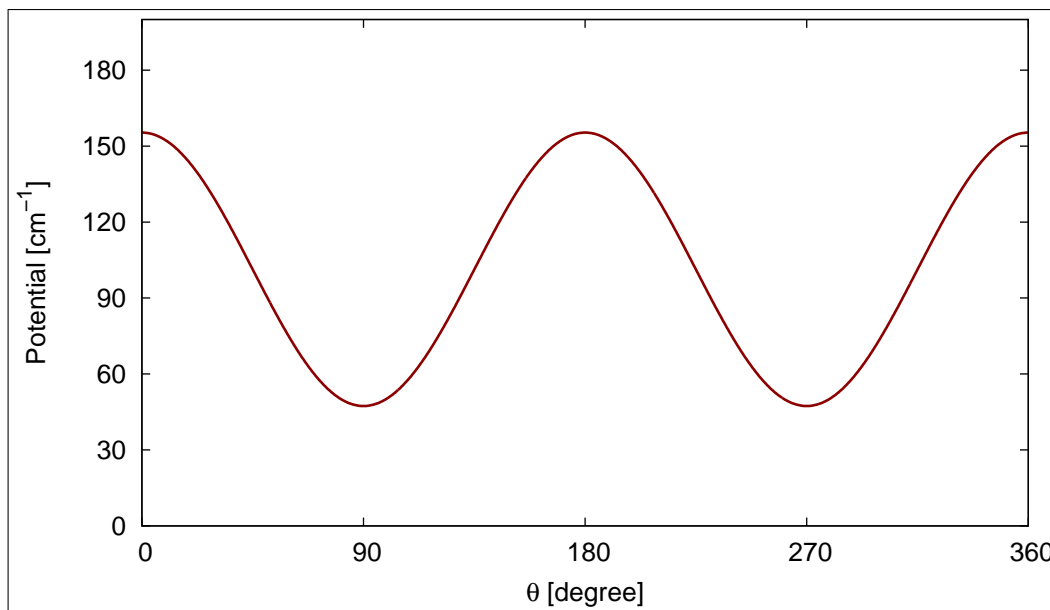
Figure 7.4. Torsional potential along the torsional "reaction path" where the minima correspond to the D$_{2h}$ second-order saddle point indicated in the Figure 7.1, which is 52 cm^{-1} above the global minimum.

7.4.2. Results

The imaginary time trajectory of the energy of this important excited state, denoted ν_{H^+}, along with the one for the ground vibrational state is given in Figure 7.5.

From these, we determined the zero-point energy (ZPE) and the ν_{H^+} fundamental excitation energy to be 7 210 and 334 cm^{-1}, respectively. A second fixed-node calculation was carried out for the torsional mode to obtain the tunneling splitting of that mode. Thus, the three DMC energies, that is, the ZPE, the ν_{H^+} fundamental, and the ground-state torsional splitting are taken as benchmark results, shown in Table 7.2. We did not attempt higher-energy, fixed-node DMC calculations due to very strong
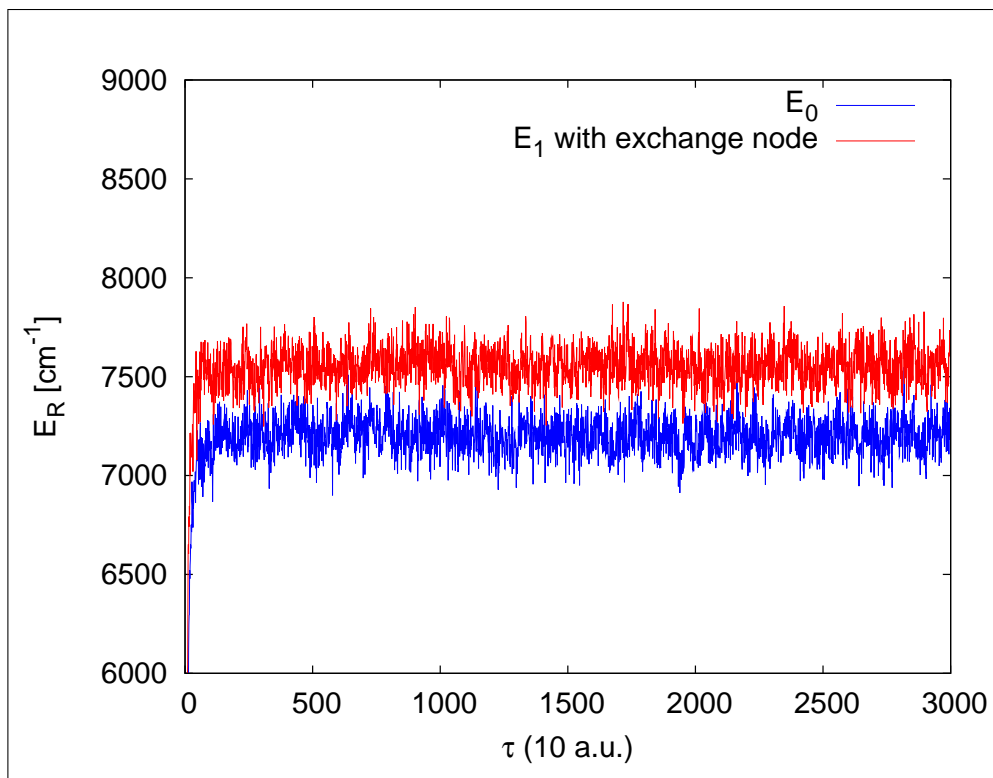
Figure 7.5. Diffusion Monte Carlo trajectories for the ground state and first excited shared-proton mode. The energies of these two states are given in Table 7.2.

mixing that occurs for such states, which precludes making nodal assignments based on simple symmetry arguments.

7.5. MULTIMODE-"Reaction Path" Version

The "reaction path Hamiltonian" version [93, 111, 114] of MULTIMODE [55, 56, 58], denoted MM-RPH, is an extension of the earlier single reference MULTIMODE to include one large amplitude motion, such as the torsional motion of the two H_2 in case of H_5^+. The fact that a torsional degree of freedom exists for H_5^+ demands the use of MM-RPH in an analysis of this system. In addition, we require the path also preserves the D_2 symmetry of the ground state wave function. To this end we chose a path with the central bridging proton collinear with and equidistant form the center of mass

of the two H_2. Then for each H_2-H_2 torsion angle the potential was minimized with respect to all the other internal coordinates. The resulting potential along this path is shown in Figure 7.4. The vibrational bases in the orthogonal degrees of freedom were obtained using the normal modes of the second order saddle point of higher symmetry, i.e., D_{2h}, shown in Figure 7.1. In principle any point along the torsional path could be used to obtain the vibrational basis and the choice made was done mainly to avoid degenerate modes, which complicate the calculation.

To obtain basis functions for the torsional path, we used 56 primitive functions which were integrated by 120 equally-spaced Gauss-Hermite points and weights. These were contracted into eleven basis functions. For the remaining $3N - 7$ normal modes, we used 16 harmonic-oscillator primitive functions which were integrated by 20 Gauss-Hermite quadrature points and weights, and these were again contracted to six basis functions for the vibrational calculations. The biggest calculation we performed uses a 4-mode representation of the full potential of the $3N - 7$ normal modes, so in total a 5-mode representation of the potential, and 2-mode coupling for the Coriolis terms, which were integrated over the reaction path coordinate. The basis functions we used include up to 6-mode excitations with a maximum quanta of 10 in the torsional path as well as the proton-stretch mode, and a maximum quanta of 5 in the remaining modes. The maximum sum-over-quanta are 10, 15, 15, 12, 10, 10 for the 1-mode, 2-mode, 3-mode, 4-mode, 5-mode, 6-mode excitations. The sizes of the four D_2 symmetry blocks are 29 259, 28 481, 28 394, 28 394 respectively. The block Davidson method was applied to obtain the first 300 eigenvalues for each symmetry block.

Table 7.2 contains a summary of selected energies from the DMC and MM-RPH calculations. The MM-RPH energies are in good agreement with the benchmark DMC ones. Note especially the strong positive anharmonicity for the overtones of the

"bright" shared-proton mode. Finally, eigen-functions are used to obtain vibrational dipole matrix elements using numerical quadrature to evaluate the integrals and also using a 5-mode representation of the coordinate dependence of the dipole components, just as was done for the potential. We note that these calculations, which also ignore H-atom exchange, are zero total angular momentum "vibrational-only" spectra. This type of spectrum is reasonable to compare to the experimental spectra, which are not rotationally resolved. These are the first fully coupled anharmonic spectra reported for these cations.

Table 7.2. Vibrational energies (cm^{-1}) of H$_5^+$ and D$_5^+$ obtained using Diffusion Monte Carlo (DMC), Reaction Path, and MULTIMODE(MM-RPH).

	H$_5^+$		D$_5^+$	
	DMC	MM-RPH	DMC	MM-RPH
ZPE	7210	7244	5152	5147
ν_{H^+}	334	382	222	257
$\Delta\nu_{\text{torsion}}$	80	66	32	28
$2\nu_{H^+}$		1718		1241
$3\nu_{H^+}$		2751		1821,1834

7.6. IR spectra

The calculated IR spectra over a large spectral range, shown as sticks and also broadened with a 30 cm^{-1} Gaussian window function, are given in Figure 7.6.

The very intense feature seen in both spectra corresponds to the shared-proton fundamental. From the fixed-node DMC calculations, this feature is predicted to occur at around 334 and 222 cm^{-1} for H$_5^+$ and D$_5^+$, respectively. Features above 2 000 cm^{-1} will be discussed in detail below in connection with the experiment. There are noteworthy additional features indicated in Figure 3 below 2 000 cm^{-1}. Also note that
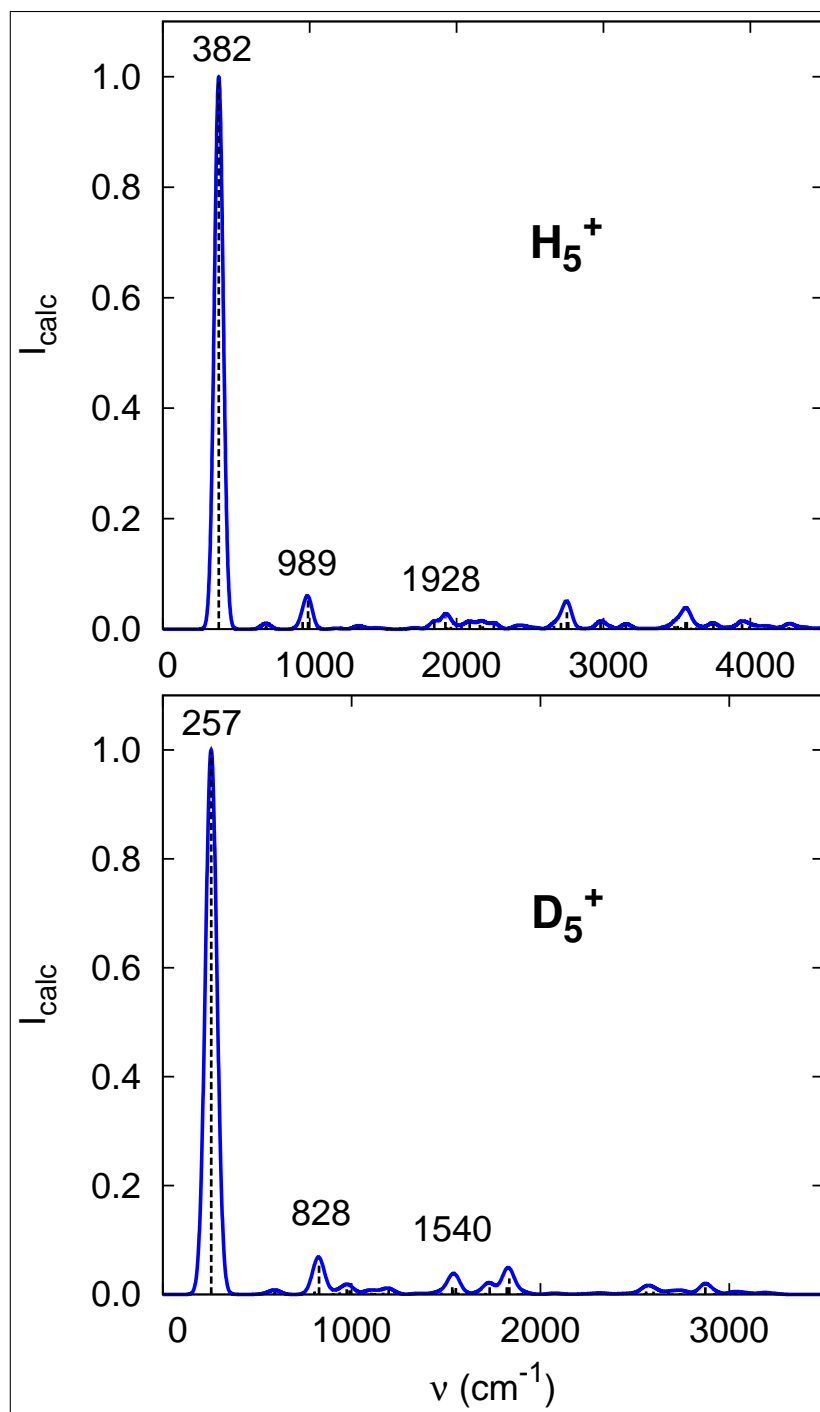
Figure 7.6. Calculated spectra of H$_5^+$ and D$_5^+$ over a large spectral range.

the energies given in this figure and Figure 7.7 are for the broadened peak positions and are close to but not the same as any molecular eigenvalue.
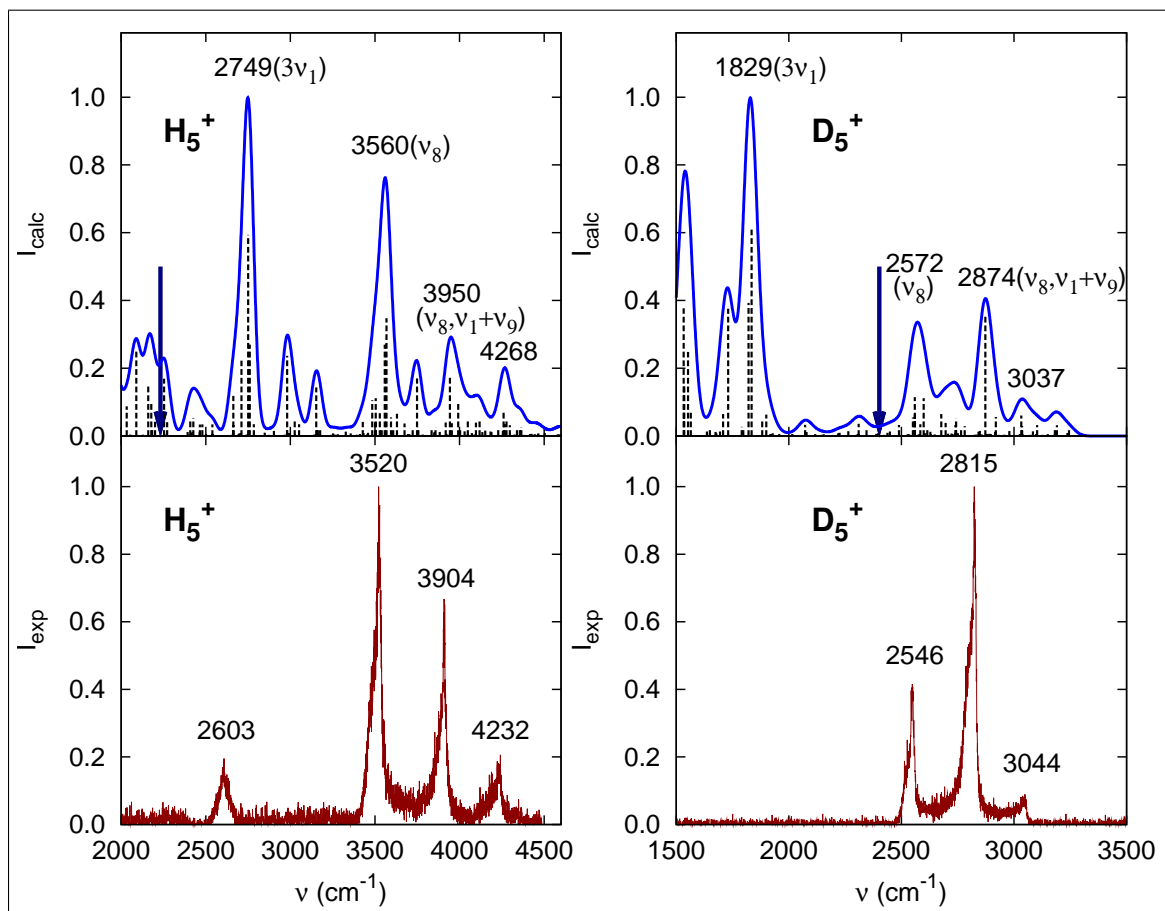
Figure 7.7. Calculated (with assignments) IR and experimental action spectra of H_5^+ and D_5^+. Arrows indicate the theoretical threshold for dissociation.

Experimental infrared photodissociation spectra and calculated absorption spectra are shown in Figure 7.7 over the spectral region of the former. These cover the region of the IR spectrum where the photon energy exceeds the dissociation energy, D_0. From DMC calculations [105], D_0 is 6.37 and 6.87 kcal/mol for H_5^+ and D_5^+ respectively, with uncertainties of roughly 0.01 kcal/mol. These energies correspond to threshold frequencies of $2\,227$ and $2\,402$ cm^{-1} for H_5^+ and D_5^+, respectively. Note that the peak positions of these photodissociation spectra correspond to those of the IR absorption spectra, but the intensities are not quantitatively comparable. With this in mind, consider the comparison between the experimental and calculated IR spectra. As seen, the experimental spectrum for H_5^+ contains four bands at $2\,603$, $3\,520$, $3\,904$, and

$4\,232$ cm^{-1}. The three higher-energy bands correspond well to the broader features reported previously with much lower signal levels [103]. The spectrum for D_5^+, which has not been studied previously, contains bands at $2\,546$, $2\,815$, and $3\,044$ cm^{-1}. The lower-energy bands therefore establish firmupper limits to the dissociation energies (D_0) for each ion, which are consistent with, but higher than, the computed values. The widths and relative intensities of these features are invariant over a wide range of laser powers down to the limit of detection and are concluded to represent the intrinsic one-photon spectra of these features. The bandwidths (40-60 cm^{-1}) are much greater than the 1 cm^{-1} laser line width, suggesting that these arise, at least in part, from predissociation. However, the bands are not symmetric, and therefore, some contribution is likely also present from the rotational contour.

The calculated spectra, with assignments, are in good accord with experiment. Note that the peaks at $3\,950$ (for H_5^+) and $2\,874$ cm^{-1} (for D_5^+) have two assignments since the molecular eigenstate has almost equal contributions from both zero-order states. Also, the calculated peaks at $4\,268$ (H_5^+) and $3\,037$ (D_5^+) cm^{-1} have no assignments because these are many contributing zero-order states, including a number with excitation of the "bright" shared-proton mode, mode 1 (indicated in Figure 7.2). Also recall that mode 8 is an IR-active HH stretch and mode 9 is a higher-energy HH stretch. Thus, from the calculations,most of the experimental spectral features involve combination bands or overtones of the shared-proton mode. The exceptions are the bands labeled ν_8 for both H_5^+ and D_5^+. Agreement between theory and experiment for this fundamental is quite good, $3\,560$ and $3\,520$ cm^{-1}, respectively, for H_5^+ and $2\,572$ and $2\,546$ cm^{-1}, respectively, for D_5^+. For transitions involving the shared-proton stretching mode, theory is above experiment. This is consistent with the MM-RPH energies for this mode being higher than the DMC result and likely significantly higher for overtones of thismode. According to theory, the experimental peaks for the D_5^+ spectrum at $2\,546$, $2\,815$, and $3\,044$ cm^{-1} correspond to, that is,

have the same assignments as, the experimental H_5^+ peaks at $3\,520$, $3\,904$, and $4\,232$ cm^{-1}. That these D_5^+ peaks are red-shifted by factors very close to the $2^{1/2}$, that is, 1.40, 1.42, and 1.39, respectively, provides additional assurance that the theoretically based correspondence is correct.

As noted above, bands at nearly the same positions as the $3\,520$, $3\,904$, and $4\,232$ cm^{-1} features, but with greater line widths, were reported previously [103] and tentatively assigned based on *ab initio* harmonic frequencies at the global minimum. Specifically, the first band was assigned as an overtone of a fundamental at $1\,746$ cm^{-1}, the second was assigned to the H_2 normal-mode stretch fundamental, and the third band was signed to a combination of the H_2 fundamental with a low-frequency H_3^+-H_2 stretch mode. The present assignments, which are based on saddle point normal modes, are, not surprisingly, completely different from the previous tentative assignments.

Finally, note some additional weaker features in the calculated spectrum for H_5^+ at roughly $2\,300$ and $3\,200$ cm^{-1}, with hints of these features in the experimental spectrum. These features are difficult to assign to a single state, and therefore, we have not done that.

7.7. Summary

In summary, new experiments and calculations have revealed and assigned unusual features in the infrared spectra of the highly fluxional H_5^+ and D_5^+ cations. The delocalized and highly anharmonic shared-proton stretch mode was shown to carry very large oscillator strength, and excitation of this modewas found to play amajor role in the assignment of experimental spectral features. In addition, several very intense features in the far-IR region have been predicted.

Part III.

Approximate Quantum Models

Chapter 8.

Intramolecular Vibrations of Clusters

In this chapter we describe quantum approaches to obtain the intramolecular vibrational energies of water clusters with possibilities of extending to any clusters, all beyond the harmonic approximation, which we term "post-harmonic". Full-dimensional rigorous quantum approaches for general clusters are far beyond current capabilities. Indeed that state-of-theart is represented by the recent 12d calculations of Leforestier et al. for the water dimer [26], discussed briefly above. So to proceed, some compromises must be made. In this spirit our focus has been on intramolecular modes, which are far less floppy than many of the intermolecular modes. The most sophisticated approach we have taken for these modes has been with the code Multimode [55, 56], which as the name implies, performs vibrational calculations for coupled modes. The essential aspects of the approach taken in this code will be given below. The other models we consider are far more approximate, much less computationally demanding, and, therefore, applicable to large clusters. One the other hand, as the continuing afford from Chapter 3, this chapter shows further evidence of the predicative accuracy of the water potential, PES(1,2,3) via computing intramolecular vibrational energies of water clusters on PES(1,2,3).

First the methodologies of a number of quantum models are described in the following section, followed with results and discussion. Finally, this chapter is completed with a summary and conclusions.

8.1. Methods

8.1.1. Local-mode model

The local-mode (LM) model has been used with considerable success recently by Auer and Skinner, to describe the OD-stretch in dilute mixtures of HOD in D_2O [115, 116]. In this model the 1d Schrödinger equation

$$\left[-\frac{\hbar^2}{2\mu} \frac{\partial^2}{\partial r_i^2} + V_i(r_i) - E_{n_i} \right] \phi_{n_i}(r_i) = 0 \tag{8.1}$$

is solved for the OD-stretch mode of HOD at local minima along a classical trajectory with all other modes held fixed. Auer and Skinner obtained the 1d potential $V_i(r_i)$ directly from efficient B3LYP/6- 311++G** calculations along a grid in the OH-stretch. More recently, Paesani et al. [20] have employed this model along with a centroid molecular dynamics (CMD) treatment of the underlying dynamics using the TTM3-F potential.

The LM model is very appealing owing to its simplicity; however, its obvious limitation is to OH(D)-stretch modes only. We will test its accuracy in the next section.

8.1.2. Anharmonic normal-mode model

The anharmonic normal-mode (ANM) model has a long history, see e.g., Ref. [117]. It is described by the single-mode Schrödinger equation in (mass-scaled) normal modes

$$\left[-\frac{\hbar^2}{2\mu}\frac{\partial^2}{\partial Q_i^2} + U_i(Q_i) - \varepsilon_{n_i} \right] \chi_{n_i}(Q_i) = 0, \tag{8.2}$$

where Q_i is a given normal mode and Ui is the potential in that mode with all other modes fixed at zero. The advantage of this model is that it can be applied to all of the normal modes of any size cluster. It also will be tested below.

For monomer H_2O, the local-mode model is known to be a better zero-order description of the overtones than the normal-mode model [118]. Here we examine these models for the fundamentals of H_2O, which are of direct relevance to water clusters and bulk water. We do that using the (semi-empirical) Partridge-Schwenke potential [119] for H_2O which gives fully-coupled OH-fundamentals at 3656 and 3755 cm^{-1}, in excellent agreement with experiment, by design. The LM model gives 3727 cm^{-1} for both stretches, which are of course identical for the monomer. This result is between the exact results as expected. The results from the ANM model are 3747 and 4038 cm^{-1}, respectively, which, although different for each mode, are less accurate than the LM result. Note that the harmonic normal-mode results are 3833 and 3944 cm^{-1}, and so the ANM result for the higher frequency anti-symmetric stretch is actually less accurate than the harmonic result. (This does not bode well for the accuracy of the ANM model for clusters.)

8.1.3. Local-monomer model

A new model we introduce here is specific for clusters. In this approach, we solve the Schrödinger equation for each monomer embedded in a cluster. The equation is

$$\left[\hat{T}_m + U_m(\mathbf{Q}_m) - \varepsilon_{n_m}\right] \chi_{n_m}(\mathbf{Q}_i) = 0 \tag{8.3}$$

where $\mathbf{Q}_m$ represents the three intramolecular normal coordinates of monomer m in the field of all other monomers (held fixed) at a given minimum, $\hat{T}_m$ is the full kinetic energy operator (including vibrational angular momentum terms) in these coordinates and U_m is the potential of perturbed monomer m. To implement this, we perform a normal-mode analysis of the perturbed, relaxed monomer in the field of all other monomers held fixed. This results in nine non-zero frequency "local normal modes" for each monomer. In principle, these nine modes could be coupled, but that would be highly computer intensive. Instead, we couple the three intramolecular modes, the perturbed monomer OH-stretches and bend. We then solve the coupled Schrödinger equation above in these modes using MM with an exact 3MR of the potential. This is clearly more computer intensive than a 1d calculation; however, it is of routine effort (provided one has the potential of course). This model, denoted "LMon", provides results for bending and stretching vibrations and it is expected to be more accurate than either single-mode anharmonic model.

8.1.4. MULTIMODE

Exact vibrational calculations in all modes are not currently feasible. Thus, we undertook "less-than-exact" vibrational calculations with the code MULTIMODE[55, 56]. This code obtains the eigenfunctions and eigenvalues of the Watson Hamiltonian using a vibrational configuration interaction (CI) approach. In order to apply the code

to moderately large molecules the following n-mode representation of the full potential[55, 56] in mass-scaled normal modes is used. (See details in Chapter 5) Typically, this representation is truncated with n between 3 and 5. An advantage of this approach is that convergence of eigenvalues can be monitored as n increases. However, even with this n-mode representation of the potential full dimensional vibrational CI calculations for the water dimer and trimer are still not feasible in large part regardless of even larger clusters, because the Watson Hamiltonian cannot describe the torsional modes in these systems.

Thus, we take an approach that exploits the disparity between the inter- and intramolecular harmonic frequencies. It is to partition the vibrational space into "system" and "bath" modes and to perform vibrational CI calculations in the partitioned spaces. For the dimer and the trimer the system consists of six monomer plus some intermolecular modes and nine monomer plus one intermolecular mode, respectively. This partitioning has been implemented in MULTIMODE. In brief, vibrational CIs are done for each group of modes (parameters of each CI calculations are identical to what is used in previous single CI as described in detail elsewhere [55, 56]) and a final diagonalization can be done in a direct-product basis of the eigenfunctions of the separate groups. For very floppy complexes, such as the water dimer especially, and also for the trimer, this final diagonalization is problematic and so we do not do that. The source of the problem is the poor rectilinear description of the lowest frequency torsional modes and the consequent artificially large coupling between those modes and the high frequency intramolecular modes. Instead we focus on the single group of system modes. We examine the convergence of monomer vibrational energies with respect to the number of modes included in the system, starting with the minimum numbers of 6 and 9 for the dimer and trimer, respectively.

The vibrational energies of the six monomer modes of $(H_2O)_2$ have been reported in several theoretical studies based at least in part on ab initio approaches [120–122]. One used a local-mode approach for these modes [120, 121] and the other used standard second-order perturbation theory [122]. These approaches were based on semirigid molecule methods, using limited parts of the potential. The good agreement with the experiment indicates that the monomer vibrational modes are not strongly influenced by the torsional modes and supports the approach taken here.

As noted we used the system-bath approach in MULTIMODE to set up and diagonalize the Watson Hamiltonian matrix in the subspace of system modes. For the dimer, the system is a minimum of six intramolecular modes and then enlarged with one to three intermolecular modes. The harmonic frequencies of these three intermolecular modes are 600, 344, and 177 cm^{-1}. Calculations were done with two-, three-, and four-mode representations of the potential. For all but the largest nine-mode calculations the results are converged to within several wavenumbers or less with the fourmode representation. For nine-mode calculations a five-mode representation is needed to achieve this level of convergence. Convergence was also checked with respect to the size of the vibrational CI and results are well converged with respect to this parameter. For the trimer CI calculations it is not feasible to add more than one intermolecular mode to the nine-monomer mode system and three choices were made for the tenth mode, i.e., intermolecular modes decreasing harmonic frequency. The calculated monomer fundamental energies changed by one or two wavenumbers relative to the ninemode calculation and so we give results for the nine-mode CI.

For the trimer CI calculations it is not feasible to add more than one intermolecular mode to the nine-monomer mode system and three choices were made for the tenth mode, i.e., intermolecular modes decreasing harmonic frequency. The calcu-

lated monomer fundamental energies changed by one or two wavenumbers relative to the ninemode calculation and so we give results for the nine-mode CI.

For the present purpose, energies from MM calculations for the water dimer and trimer will be considered the benchmarks, with the understanding that they probably are within of 10-20 cm^{-1} of the converged results, for a given potential.

8.2. Results and Discussion

In this section, We test the two single-mode models and the LMon model against MM energies for the water dimer and trimer. The tests below of the accuracy of the local-mode model. We also test the anharmonic normal-mode and new local-monomer models for the water dimer and trimer next.

8.2.1. "Benchmark" tests of $(H_2O)_2$ and $(H_2O)_3$

We now start with an examination of the accuracy of the single-mode and local-monomer models for the water dimer and trimer. This is done first for the dimer by comparing results from these models with MM results as well as experiments in Table 8.1.

We reported results from coupled vibrational MM calculations of intramolecular mode fundamentals for the water dimer [14] using the HBB1 potential. These results, and for reference the normal-mode harmonic energies, are compared with experiment [123–125], including the very recent ones done in a He nanodroplet [126]. The MM calculations used a four-mode representation (4MR) of the potential and eight coupled modes, consisting of the six intramolecular modes plus two of the highest frequency intermolecular modes. As seen, there is good agreement between experiment

and HBB1 results especially for the hydrogen-bonded stretch. Note that while there are some uncertainties in the experimental results, the magnitude of the difference between the MM calculations using HBB1 is typical of the errors seen in other cases of exact vibrational calculations of OH-stretch fundamentals using CCSD(T)/aVTZ-based potentials.

Now we turn to the comparison of the approximate quantum models against the "benchmark" MM results. As seen, the ANM model is the least accurate. The LM model is substantially more accurate and as expected the LMon model is the most accurate. The advantage of the LMon model over the LM one is in getting the additional bending fundamentals. Note that the LM model for the dimer does not suffer from the degeneracy inaccuracy seen for the water monomer. The H-bonding in the dimer is sufficiently strong to break the equivalence of the four local OH-stretches.

Table 8.1. Calculated harmonic (HO), local-mode (LM), anharmonic normal-mode (ANM), local-monomer (LMon), coupled MULTIMODE (MM) and experimental intramolecular fundamentals (cm^{-1}) of $(H_2O)_2$ at the global minimum using the HBB1 potential.

mode	HO	LM	ANM	LMon	MM	Gas-phs	He Nano[d]
bend-1	1646		1635	1595	1588	1600.6[a]	
bend-2	1665		1654	1602	1603	1620[a]	
OH-1	3736	3592	3615	3550	3573	3601[b]	3597
OH-2	3806	3702	3728	3637	3627		3654
OH-3	3892	3702	3836	3701	3709	3735[b]	3730
OH-4	3912	3714	4004	3724	3713	3745.5[c]	3739

The results for the water trimer are shown in Table 8.2. The comparisons of benchmark MM results with the experiment show good agreement, though not quite at the level seen for the dimer. Again the LMon model is seen to be quite accurate, and significantly more accurate than the ANM model and more accurate than the

LM model, which is reasonably accurate. The absolute deviations of these models from the benchmark results are plotted in Figure 8.1, where the accuracy of the LMon model can be appreciated. The MM trimer energies have more uncertainty than those for the dimer; however, as expected, they are below the approximate ones.

Table 8.2. Calculated local-mode (LM), anharmonic normal-mode (ANM), local-monomer (LMon), coupled MULTIMODE (MM) and experimental intramolecular fundamentals (cm^{-1}) of (H$_2$O)$_3$ at the global minimum using PES(1,2,3).

Mode	LM	ANM	LMon	MM	Gas Phase
bend-1		1658	1602	1599	
bend-2		1662	1612	1602	1609[a]
bend-3		1671	1615	1611	1638[a]
OH-1	3476	3554	3440	3410	
OH-2	3486	3715	3454	3459	3533[b],3523[c]
OH-3	3497	3734	3463	3470	
OH-4	3742	3851	3700	3694	
OH-5	3746	3857	3702	3698	3726[b]
OH-6	3748	3963	3704	3710	

[a] Ref. [123]; [b] Ref. [125]; [c] Ref. [127].

Thus, based on these tests for the dimer and trimer we conclude that the LM and LMon models provide "usably" accurate results for the OH-stretch, and OH-stretch and bend fundamentals, respectively. The latter model, as expected, is more accurate in addition to providing results for the intramolecular bending modes.

8.2.2. Predictive tests of (H$_2$O)$_6$ and (H$_2$O)$_{10}$

It will be difficult to further test these models for larger clusters, as MM, or other similar calculations, will become prohibitively difficult. We do provide a limited test along these lines for the water hexamer in Table 8.3, where we give 3MR MM results using the efficient-to-evaluate PES(1,2,KS/WB) and compare results from
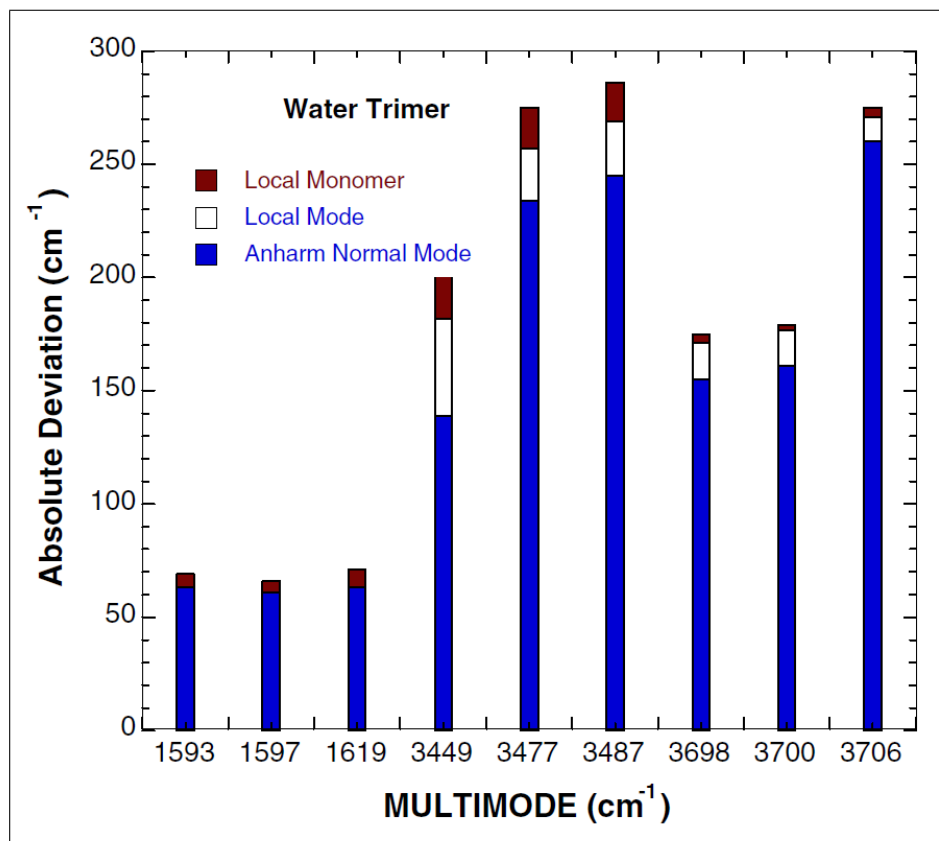
Figure 8.1. Absolute differences in energy (cm^{-1}) for the fundamental intramolecular modes of the water trimer between anharmonic normal-mode, local-mode and local-monomer and benchmark coupled mode results obtained with MULTI-MODE as explained in the text.

the LM model. We also show LM results using PES(1,2,3). As seen, there is good agreement between the MM and LM results; however it should be kept in mind, that the MM-3MR results are not well converged. Based on previous experience, they are probably higher than the converged results by 10 cm^{-1} or more. The results on the two different potential surfaces show fairly good agreement although PES(1,2,3) does yield somewhat lower energies, especially for the strongly H-bonded stretches.

Table 8.3. MULTIMODE (MM), local-mode (LM) OH-stretch fundamentals (cm^{-1}) for the water hexamer prism using PES(1,2,KS/WB) and LM results for PES(1,2,3).

Mode	PES(1,2,KS/WB)		PES(1,2,3)
	MM	LM	LM
OH-1	3340	3338	3293
OH-2	3406	3410	3371
OH-3	3491	3507	3467
OH-4	3508	3520	3490
OH-5	3537	3554	3491
OH-6	3583	3596	3551
OH-7	3599	3619	3563
OH-8	3622	3642	3628
OH-9	3654	3666	3678
OH-10	3713	3737	3689
OH-11	3723	3743	3716
OH-12	3738	3763	3740

Finally in Table 8.4 we show harmonic and local-mode results for the OH-stretches of the water decamer using PES(1,2,3) and PES(1,2,KS/WB). Here we see increased differences between the two potentials for the strongly H-bonded OH-stretches relative to the hexamer. For the decamer, there are 45 2-body and 120 3-body interactions compared to 15 2-body and 20 3-body interactions for the hexamer, so these differences may be due to the increasing number of important 3-body interactions relative to the hexamer. This issue will be examined in detail in the future. Based on the

hexamer tests, the LM results using PES(1,2,3) for the decamer are probably accurate to within 20-40 cm^{-1}. Also it is worth noting that the LM model has the nice feature of assigning the energies to specific OH-stretches.

Table 8.4. Harmonic (HO) and local-mode (LM) OH-stretch fundamentals (cm^{-1}) for the water decamer using PES(1,2,3) and PES(1,2,KS/WB).

PES(1,2,3)		PES(1,2,KS/WB)	
HO	LM	HO	LM
3302	3174	3538	3364
3322	3194	3557	3375
3330	3200	3564	3394
3337	3203	3575	3394
3459	3365	3651	3490
3482	3400	3663	3498
3486	3416	3702	3576
3498	3416	3704	3577
3504	3419	3724	3578
3516	3425	3726	3579
3597	3432	3756	3581
3608	3435	3762	3585
3617	3441	3765	3588
3637	3451	3776	3590
3641	3454	3785	3601
3830	3714	3878	3756
3849	3759	3881	3757
3864	3774	3886	3764
3871	3776	3888	3765
3874	3779	3890	3766

We conclude this section with a comparison of the LM OH-stretch energies using PES(1,2,3) for the hexamer and the decamer with the experimental IR spectrum of bulk water [128] at 298 K in Figure 8.2. As seen, the energies for the decamer

are shifted in the direction of the experiment relative to those of the hexamer, as expected, perhaps indicating that the decamer is approaching the bulk limit.
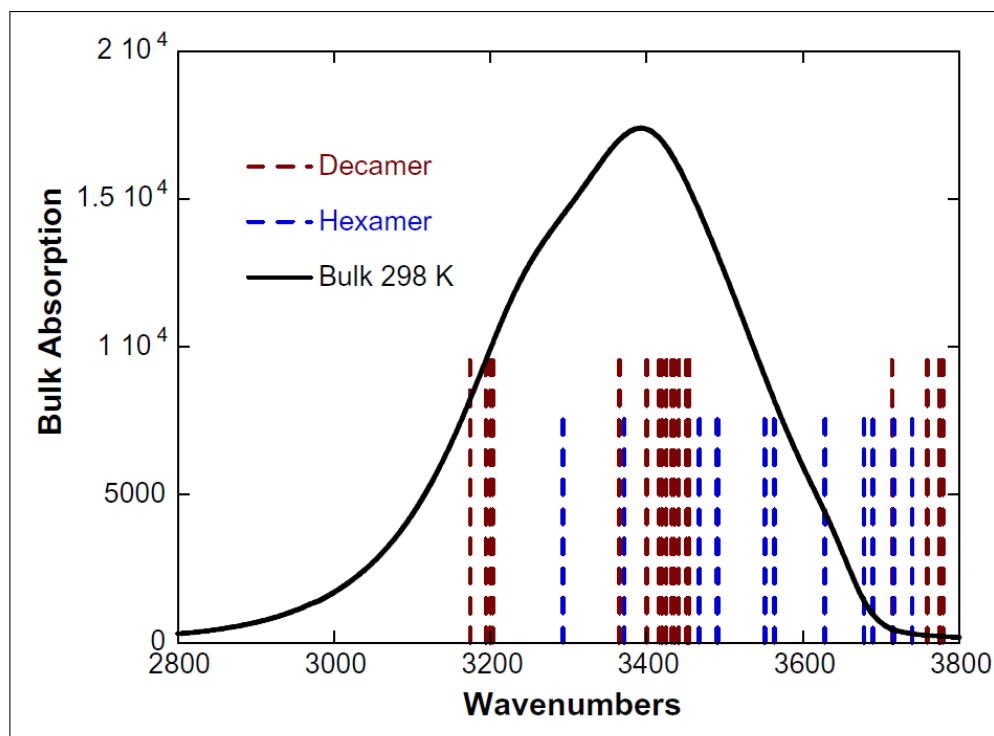
Figure 8.2. Local-mode energies of the water hexamer and decamer superimposed on the bulk water IR spectrum at 298 K in the OH-stretch region.

More work with the local-mode and local-monomer models, including the application to larger clusters, needs to be done. The calculation of infrared intensities using local-mode and localmonomer models looks to be quite feasible and this will be done in the future, using the *ab initio* dipole moment surface, which we have reported previously and which was shown to be very accurate for the water hexamer [129].

8.3. Summary and Conclusions

We reported progress on two aspects of the theoretical and computational description of water and water clusters, namely the potential energy surface and vibrational

calculations. Specifically, we described 2- and 3-body full-dimensional *ab initio* potentials based on fitting tens of thousands of electronic energies. The fits are feasible because the permutation symmetry inherent in them is exploited. Harmonic and post-harmonic calculations of intramolecular fundamentals were presented for the water dimer, trimer, hexamer and decamer. A new local-monomer model was described and shown to be of very good accuracy for the water dimer and trimer by comparison with benchmark calculations. Future work will include calculations of infrared and Raman spectra using these potentials and the local-monomer model. Additional, more computationally efficient, representations of these *ab initio* potentials, especially the 3-body potential, will be needed in order for bulk properties of water to be investigated using these accurate potentials.

Chapter 9.

One-dimensional tunneling calculations

This chapter shows a novel approximate quantum model of tunneling calculations that could be easily extended to fairly large molecular systems. The one-dimensional (1D) quantum model suggests a much better accuracy than any other 1D models existed in dealing with molecular systems in this study. All calculations are for zero total angular momentum J. Some remarks about extending the method for nonzero J are made at the end of this chapter. Further multidimensional extensions as well as nonzero J extensions to such 1D approach to tunneling splittings were reported on a follow-up paper [E. Kamarchik, Y. Wang, and J. Bowman J. Phys. Chem. A 113, 7556 (2008)].

Here, we present tunneling calculations using the reaction path Hamiltonian in the zero-curvature approximation and a one-dimensional Hamiltonian in the imaginary-frequency, rectilinear normal mode of a saddle point, neglecting the vibrational angular momentum terms. This latter Hamiltonian was recently introduced and applied to the tunneling splitting in full-dimensional malonaldeyde [Y. Wang *et al.*, J. Chem.

Phys. 128, 224314 (2008)]. The results using the latter method are shown to be much more accurate than those using the former one for the ground-state tunneling splittings for H and D-transfer in malonaldehyde and for the D+H2 reaction in three dimensions for zero total angular momentum.

9.1. Introduction

Quantum mechanical tunneling in activated chemical processes has been widely recognized since the earliest days of quantum theory. Perhaps the first theory of tunneling in this context was proposed by Wigner [130]. This was based on a parabolic description of the reaction barrier and a series expansion for the resulting thermal transmission coefficient. The analytical expression is referred to as the "Wigner tunneling correction" and is still in use today.

The curvature of the reaction barrier is given by the magnitude of the imaginary frequency of one normal mode of the (first-order) saddle point separating reactants from products (this mode is referred to as the "imaginary-frequency mode"). It comes for "free" when doing the standard normal mode analysis at the saddle-point in transition state theory. The potential in the saddle-point normal modes is usually strongly nonseparable in the reactant and product regions and thus the separable Wigner model cannot be used to describe tunneling in the extended region covering the reactants, saddle point, and products. To address this, a curvilinear path coordinate, now termed the intrinsic reaction coordinate (IRC) was introduced to describe the reaction [131–133]. This coordinate is defined as the path of steepest descent from the saddle point (usually in mass-scaled Cartesian coordinates) to reactants and products. This path is also generally referred to as the minimum energy path (MEP). The potential along this path is referred to as the MEP potential and it

provides a simple one-dimensional (1D) model for the tunneling. Hereafter we use the terms IRC and MEP interchangeably.

The IRC is mathematically one coordinate of $3N - 6$ internal coordinates plus three rotational coordinates that are needed to rigorously describe the reaction. A rigorous treatment of all of these degrees of freedom is described by the reaction path Hamiltonian (RPH) [134]. The kinetic energy operator of this Hamiltonian is fairly complex and so often approximations are made to it. A popular one, termed the zerocurvature approximation, is used in this paper and will be described briefly below.

The exact (Watson) Hamiltonian in rectilinear normal coordinates is well known[57]. Most applications of this Hamiltonian have been to calculations of rovibrational energies and wave functions, and the normal coordinates are associated with a minimum of the potential energy surface (PES). There have been applications of this Hamiltonian using saddlepoint normal coordinates. An example of such an application was reported by Seideman and Miller [135, 136], who used the exact Watson Hamiltonian to obtain the cumulative reaction probability (CRP), defined below, for the three-dimensional H+H$_2$ reaction using an exact method for zero total angular momentum $J = 0$. They also demonstrated that neglecting the vibrational angular momentum (VAM) terms in the Hamiltonian led to minor changes in the probability [136]. This approximation has been used in recent subsequent applications by Wu et al. [137] in an essentially exact calculation of the CRP for the H+CH$_4$ reaction for $J = 0$.

The exact Watson Hamiltonian has also been applied to a full-dimensional calculation of the tunneling splittings in H$_3$O$^+$ [138] and NH$_3$ [139]. Recently this Hamiltonian, without VAM terms, was used by Viel et al. [77] to calculate the ground-state tunneling splitting in malonaldehyde and malonaldehyde-d_1 in full dimensionality, using a diffusion Monte Carlo (DMC) method[77] and a recent full-dimensional PES[74].

We recently reported calculations of these tunneling splittings using a new accurate PES in full dimensionality [129]. Unbiased DMC calculations of the tunneling splittings were done in both Cartesian and saddle-point normal coordinates, using the exact Hamiltonian and also without the VAM terms, respectively. Based on the agreement found in these two independent calculations, the estimated error due to neglecting the VAM terms was roughly 1 cm^{-1} or less, or about 5% of the tunneling splitting.

We also reported tunneling splittings using an approximate 1D Hamiltonian in the imaginary-frequency normal mode, Q_{im}. This Hamiltonian consisted of a 1D kinetic energy operator, neglecting VAM terms, and potentials that are functions of Q_{im}. In one case, this potential was the fully relaxed one in 20 normal modes for fixed values of Q_{im}. The ground tunneling splittings obtained from the eigenvalues of this 1D Hamiltonian were 25.9 and 4.6 cm^{-1} and for H and D-transfer, respectively, in very good agreement with the exact results of 22 and 3 cm^{-1} with statistical uncertainties of roughly 2 cm^{-1}. These 1D results were substantially more accurate than previous ones using 1D MEP potentials, although on a slightly different PES [74]. In that work, the zero-curvature RPH was used and the H and D-atom tunneling splittings were 1.76×10^{-3} and 2.28×10^{-4} cm^{-1}, respectively. These are much smaller than the full-dimensional ones reported by of Viel et al., using the same PES of 25.7 and 3.2 cm^{-1} for H and D-transfer, respectively. Thus, for malonaldehyde the 1D results obtained using a relaxed potential in Q_{im} are evidently much more accurate than those using the conventional MEP in the zero-curvature approximation.

An unambiguous comparison of the splittings using the RPH (without curvature) and the Q_{im}-Hamiltonian without VAM terms on the same PES has not been done. We do that in this communication, and we also present new calculations of tunneling

in the D+H$_2$ reaction for $J = 0$ using the Q_{im}-Hamiltonian and the RPH one (without curvature) and compare the results to exact quantum calculations.

9.2. Method

9.2.1. One-dimensional models

The coordinates are standard, mass-scaled normal coordinates, and the Hamiltonian is the exact Watson Hamiltonian for J=0, neglecting the VAM and so-called "Watson" terms and is given by

$$\hat{H}_{Q_{im}} = -\frac{1}{2}\frac{\partial^2}{\partial Q_{im}^2} + V(Q_{im}), \tag{9.1}$$

where $V(Q_{im})$ is the fully relaxed potential for a given Q_{im}.

In the context of an exact calculation with the exact Hamiltonian, this 1D Hamiltonian can be regarded as one that defines a 1D basis in Q_{im} for use in a variational approach to obtain the eigen-functions of the exact Hamiltonian. It can also be used in multidimensional approximate methods. The one used here is the vibrationally adiabatic (VA) approximation. In this widely used approximation, a normal mode analysis is done at each value of Q_{im}, using the projected force constant matrix [134], and eigenvalues of the $3N - 7$ vibrational subspace problem are added to $V(Q_{im})$. In the simplest VA theory, the harmonic approximation is made for these eigenvalues and for the very important ground vibrational state, the 1D VA Hamiltonian for J=0 is given by

$$\hat{H}_{Q_{im}}^{\text{VAGS}} = -\frac{1}{2}\frac{\partial^2}{\partial Q_{im}^2} + V_{\text{GS}}(Q_{im}), \tag{9.2}$$

where in the harmonic approximation

$$V_{\mathrm{GS}}(Q_{im}) = V(Q_{im}) + \sum_k \frac{1}{2}\hbar\omega_k^{3N-7}(Q_{im}). \tag{9.3}$$

The 1D, zero-curvature reaction-path Hamiltonians for J=0 are given by equations quite similar to Equation 9.1 and 9.1, namely

$$\hat{H}_s = -\frac{1}{2}\frac{\partial^2}{\partial s^2} + V(s) \tag{9.4}$$

and

$$\hat{H}_s^{\mathrm{VAGS}} = -\frac{1}{2}\frac{\partial^2}{\partial s^2} + V_{\mathrm{GS}}(s). \tag{9.5}$$

where s is the path length of the MEP. This coordinate can be simply obtained from the known $3N - 6$ relaxed normal coordinates corresponding to a given Q_{im}, since the mass-scaled normal coordinates are orthogonal transformations of the mass-scaled Cartesian coordinates that are typically used to determine the MEP.

9.2.2. Numerical solutions

The fully relaxed for any one normal mode Q (i.e. Q_{im} in this particular application) is obtained by minimizing the full-dimensional potential with respect to all the other $3N - 7$ normal modes $\mathbf{Q}'$ as Q was varied stating at Q = 0, the stationary point. Newton search was used for the minimization problem in normal coordinates at each fixed Q.

Then, cubic spline method is employed to interpolate between a fixed number of points (usually equally spaced) along the fully relaxed potential $V(Q)$. More specifi-

cally, in each interval, $[Q_i, Q_{i+1}]$, we use a third order polynomial $S_i(Q)$ to represent the piecewise potential function as

$$S_i(Q) = a_i + b_i(Q - Q_i) + c_i(Q - Q_i)^2 + d_i(Q - Q_i)^3; \quad i = 1, 2, \cdots, n-1 \quad (9.6)$$

Then the four unknown coefficients, (a_i, b_i, c_i, d_i), for each piecewise formula $S_i(Q)$ are determined under a number of constraints, i.e. the function itself, its first-order and second-order derivatives are required to be smooth as follows,

$$S_i(Q_i) = V(Q_i) \qquad i = 1, 2, \cdots, n-1 \tag{9.7}$$

$$S_i(Q_{i+1}) = V(Q_{i+1}) \qquad i = 1, 2, \cdots, n-1 \tag{9.8}$$

$$S_i'(Q_{i+1}) = S_{i+1}'(Q_{i+1}) \qquad i = 1, 2, \cdots, n-2 \tag{9.9}$$

$$S_i''(Q_{i+1}) = S_{i+1}''(Q_{i+1}) \qquad i = 1, 2, \cdots, n-2. \tag{9.10}$$

This gives a total of $4(n-1) + 2 = 4n - 2$ equations for the $4n$ unknowns. To obtain two more conditions, require that the second derivatives at the endpoints be zero, so

$$S_0''(Q_0) = 0; \tag{9.11}$$

$$S_{n-1}''(Q_n) = 0. \tag{9.12}$$

Once the analytical expression of the relaxed potential is obtained, we solve the Schrödinger equations numerically, using the equally-spaced "Discrete Variable Representation" (DVR) of the kinetic energy operator due to Colbert and Miller [140]. In this approach, the second derivative of the coordinate is approximated using an

infinite order finite difference formula,

$$y''(Q_0) = -\frac{1}{\Delta Q^2}\left[\frac{\pi^2}{3}y(Q_0) + \sum_{k=1}^{\infty}(y(Q_k) + y(Q_{-k}))\frac{2(-1)^k}{k^2}\right], \qquad (9.13)$$

and the potential is naturally diagonal in the DVR basis. We then turn the ordinary differential equation problem into a standard eigenvalue problem, which can be solved by diagonalizing the Hamiltonian matrix.

9.3. Tests

9.3.1. Tunneling splitting in malonaldehyde

The VA ground-state tunneling splittings of malonaldehyde and singly deuterated malonaldehyde were calculated using the 1D Q_{im}-Hamiltonians given by Equation 9.1 and 9.2 and also using the recent full-dimensional PES of Ref. [129]. They have been calculated using the MEP potential in Equation 9.4. Before presenting the results, we show the potentials $V(Q_{im})$ and $V(s)$ in Figure 9.1. As expected, these are double-well potentials; however, $V(s)$ is much wider than $V(Q_{im})$. This difference is obvious because s is the path length at the value Q_{im} from the saddle point and this is larger than Q_{im} itself. The tunneling splittings were obtained using these potentials as the difference between the two lowest energy eigenvalues, which were obtained numerically. The results are 25.9 and 4.6 cm^{-1} for H and D-transfer, as reported previously [129] for $V(Q_{im})$ and 0.30 and 0.10 cm^{-1}, respectively, for $V(s)$. As noted already, the former pair are in quite good agreement with the full-dimensional DMC splittings of 21-22 and 3-4 cm^{-1} and thus much more accurate than the ones obtained with $V(s)$.
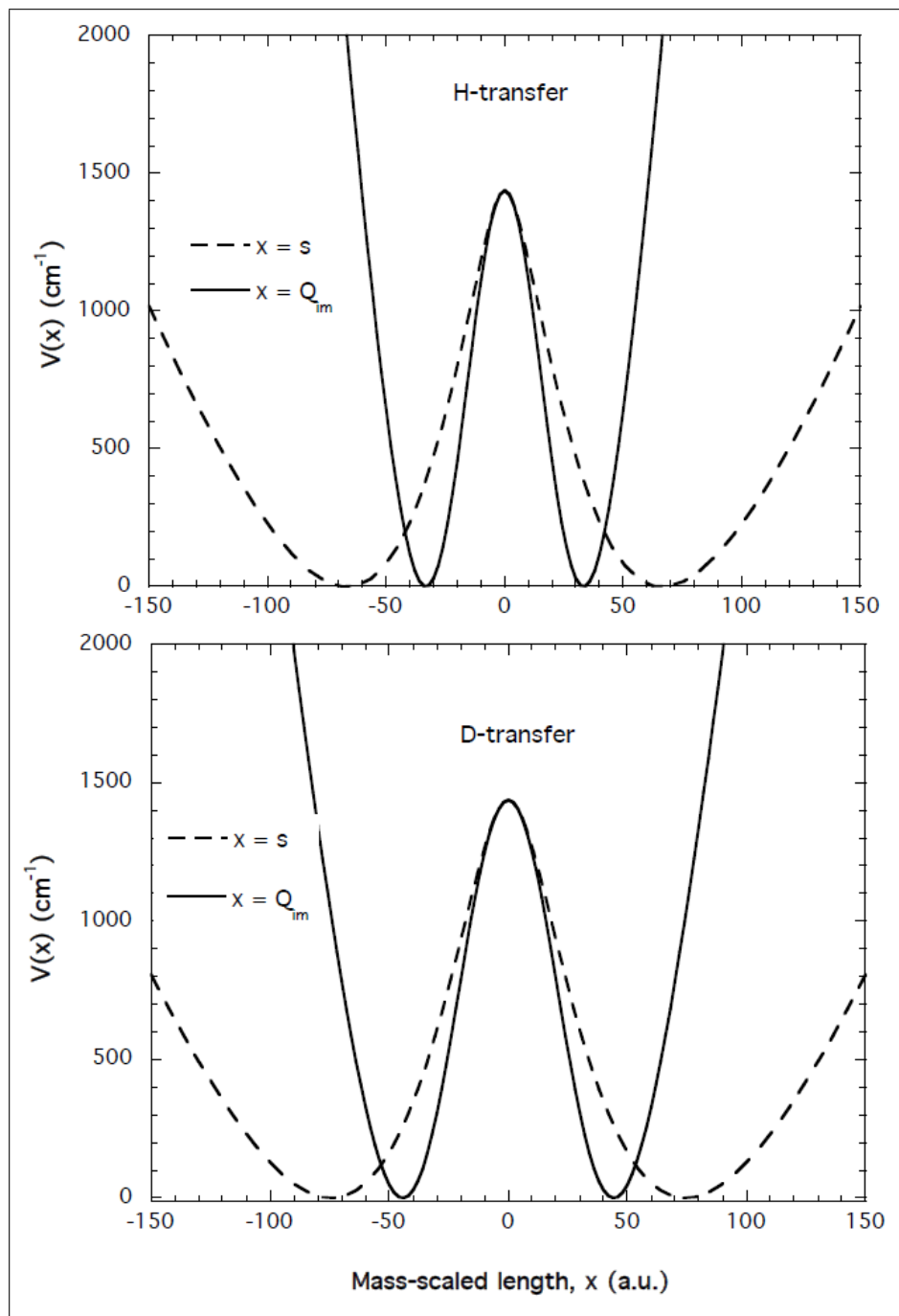
Figure 9.1. 1D potentials describing the H and D-transfer in malonaldehyde, using the full-dimensional potential of Ref. [129], as a function of the mass-scaled normal mode Q_{im} and the "reaction path" s, as described in the text.

We obtained tunneling splittings for the VA ground-state 1D potentials and the results are 17.1 and 2.7 cm^{-1}, respectively for H and D-transfer. These are fairly small changes relative to the results obtained with the bare potentials, and they reflect the small differences between $V_{\text{GS}}(Q_{im})$, which has a barrier of 1606 cm^{-1}, and $V(Q_{im})$, which has a barrier of 1438 cm^{-1}. We do not report the corresponding splittings for the VA ground-state MEP potential as they would be smaller and thus even less accurate than ones obtained with bare MEP potential. Note the VA ground-state potential reported in Ref. [129] was obtained using an approximate normalmode analysis done by diagonalizing with the Hessian in the 20 real-frequency modes of the saddle point. The resulting $V_{\text{GS}}(Q_{im})$ potentials in that reference are about 1% smaller than the ones here. This presumably accounts for the 0.2 cm^{-1} difference in the D-atom splitting here compared to the one in Ref. [129]. That the H-transfer tunneling splitting here agrees with value of 17.1 cm^{-1} given in Ref. [129] is probably fortuitous.

9.3.2. D+H$_2$ reaction

We now consider tunneling in the D+H$_2$ reaction. Exact quantum scattering calculations using an accurate potential [141] have been reported for this reaction [142], and these serve as the benchmark results. For this reaction, there is a fairly large drop in the zero-point energy (ZPE) of the saddle point relative to the reactant H$_2$ (roughly 0.05 eV), and so we consider only the 1D potentials $V_{\text{GS}}(s)$ and $V_{\text{GS}}(Q_{im})$. The adiabatic vibrational energies were obtained with the projected force constant matrix at each value of Q_{im} (and s). These effective potentials are plotted in Figure 9.2. As seen, the MEP potential is much wider than the Q_{im} one (similar to the comparison seen for malonaldehyde). The tunneling probability as a function of the reactant translational energy Etrans was obtained using the well-known semiclassical

expression $\left(1 + e^{2\theta}\right)^{-1}$, where θ is the usual 1D action integral obtained as a function of E_{trans}.
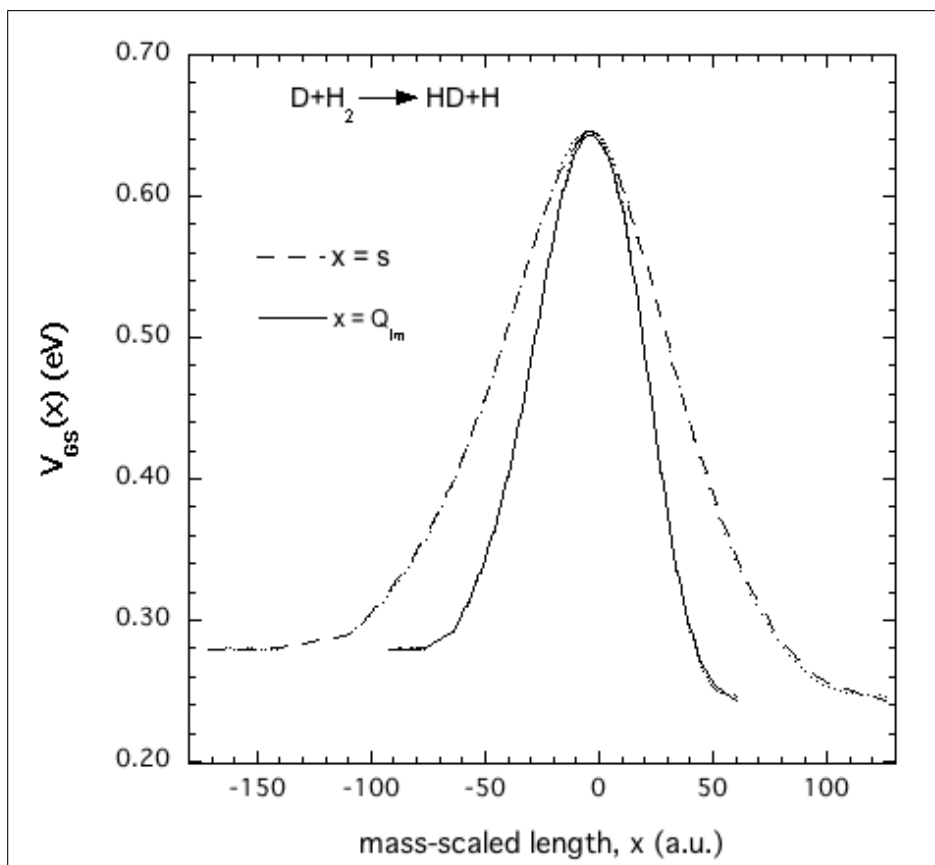
Figure 9.2. 1D VA ground-state potential for the D+H$_2$ reaction, using the full-dimensional potential of Ref. [141], as a function of Q_{im} and the reaction path s, as described in the text.

The results of the tunneling calculations using $V_{\text{GS}}(s)$ and $V_{\text{GS}}(Q_{im})$ are plotted in Figure 9.3 along with the exact quantum ones versus the total energy E. The exact quantum result is the CRP. It was obtained by summing the initial state selected probabilities for $j = 0 - 5$ for the ground vibrational state of H$_2$ for a given E. This range of j is sufficient to obtain a well-converged value for the benchmark CRP in this energy range. To convert the 1D tunneling results to functions of E, a choice for the H$_2$ ZPE must be made. In the tunneling region, there is some difference between choosing the exact or the harmonic value. This has been discussed in the literature

and the arguments generally favor adding the accurate ZPE. The justification for this comes from the near equality of the VA barrier height if one uses the harmonic approximation for V_{GS} or a more accurate anharmonic one. Thus we have added 0.2702 eV (the ZPE of the quantum calculations) to E_{trans} to get E for the 1D results (for reference, the harmonic ZPE is 0.273 eV). Also we should note that in the energy range shown, the CRP is dominated by the adiabatic ground state and so the tunneling probabilities obtained with potentials $V_{GS}(s)$ or $V_{GS}(Q_{im})$ give the corresponding approximate CRPs.
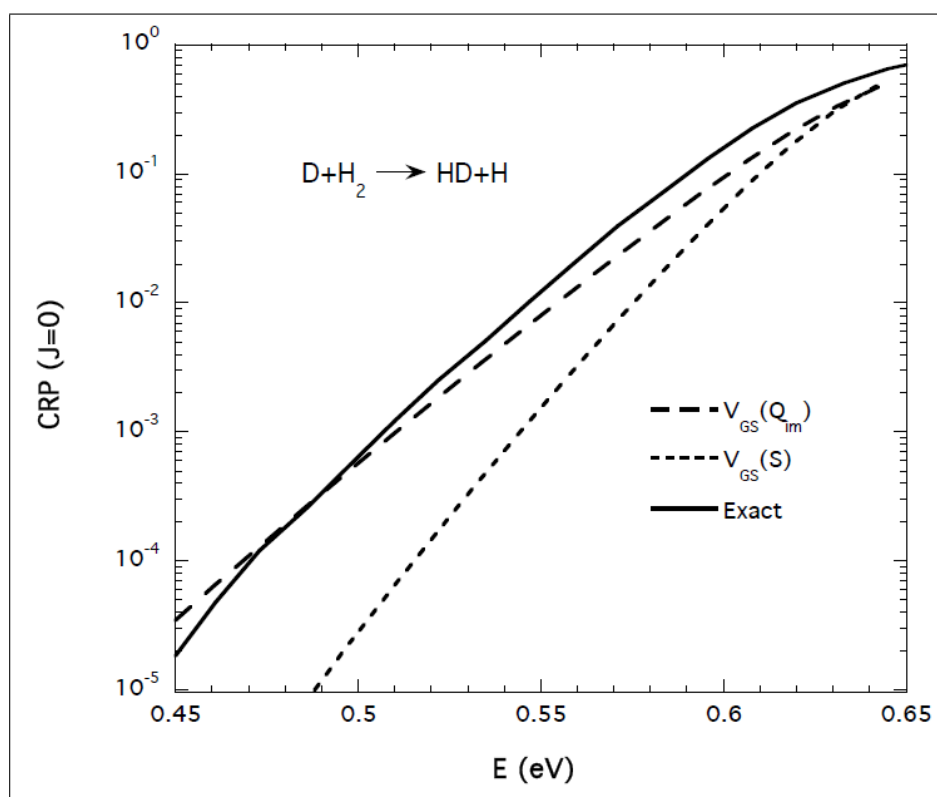
Figure 9.3. CRP vs the total energy in the tunneling region from exact quantum calculations [142] and present Q_{im} and reaction path s, potentials as described in the text.

As seen, the CRP obtained with the Q_{im}-Hamiltonian is in much better agreement with the exact CRP than is the CRP obtained using the zero-curvature RPH Hamiltonian. (The comparison shown here between the exact and zerocurvature RPH

results is quite similar to the comparison reported earlier by Miller et al. [134] for the H+H_2 reaction, $J = 0$.) The accuracy of the probability obtained with the 1D Q_{im}-Hamiltonian (roughly 20%-40% of the exact result) in energy range shown is quite good, considering the simplicity of this Hamiltonian.

To conclude this subsection, we note that it is possible to obtain the CRP using the Q_{im}-Hamiltonian over an extended energy range. First, one needs to extend the ground state reaction probability to total energies above the barrier [143]. Second, to account for vibrationally excited states, one can replace V_{GS} with the appropriate excited-state potentials or use simple energy-shifting theories that have been extensively discussed and tested [144]. Also extension of the method to J greater than zero can be done either using the relevant term in the Watson Hamiltonian, and to be consistent with the approximation used here, neglecting the VAM part of it, or by simpler J-shifting methods [144].

9.4. Discussion

The tests presented here for (21 degrees of freedom) malonaldehyde tunneling splittings and the D+H_2 reaction probability in the tunneling region are qualitatively different and so the accuracy of the simple Q_{im}-Hamiltonian approach is encouraging. Space does not permit an extensive analysis of why this Hamiltonian gives more accurate results for these two examples than the zero-curvature RPH, and so we defer this to a later publication. However, one possible factor may be the relatively small error made by neglecting the VAM terms in the Watson Hamiltonian compared to neglecting curvature in the RPH. It is also of interest to speculate a bit on why the tunneling path in the Q_{im}-space is evidently more accurate/realistic than the one in s-space. The latter path (without curvature corrections) has consistently been found

to underestimate tunneling, implying that the barrier is too "wide in this space". As shown here the tunneling barrier in the rectilinear Q_{im}-space is narrower than the s-space one and this leads to an increase in the tunneling probability. The error in the width of the s-space barrier is substantially corrected when curvature terms in the kinetic energy operator are included and this suggests that the neglect of curvature is an important source of error in the zero-curvature RPH. Evidently neglecting the VAM terms in the Q_{im}-Hamiltonian leads to smaller errors. This has been verified extensively in the literature and it is largely attributable to the fact the VAM terms scale like the reciprocal of the moment of inertia tensor, i.e., rotation constants.

It is important to note that extensive work has been done, especially for chemical reactions, to go beyond the zero-curvature RPH Hamilitonian used here. These include a rigorous treatment of curvature for the $H+H_2$ reaction[134], as already noted, which does lead to significantly improved agreement for the CRP for $J = 0$. Also, so-called "corner-cutting" curvilinear paths have been suggested, e.g., the Marcus-Coltrin path[145]. Many of these important aspects and extensions to the RPH have been incorporated by Corchado et al. in the code POLYRATE[146], which is widely used to obtain tunneling corrections to transition-state theory rate constants.

For malonaldehyde, a number of reaction paths used, in semiclassical methods, that are more sophisticated than the zero-curvature MEP one tested here have been used to obtain the ground-state tunneling splitting. These including a variety of 1D reaction paths[76,147] as well as instanton paths[76,147]. Space does not permit a detailed discussion of these; however, with several very recent benchmark calculations available on full-dimensional PESs, these other methods can be tested, and it will be interesting to determine their accuracy relative to the very good accuracy of the Qim-Hamiltonian presented here.

Finally another topic for future investigation is the generality of the Q_{im}-Hamiltonian method. The procedure to obtain the relaxed potential $V(Q_{im})$ and the adiabatic energies was quite straightforward in the two examples here. Whether this is always the case remains to be determined. As with the RPH, technical challenges may appear with the Q_{im}-Hamiltonian method. In particular, it is worthwhile to point out that the evaluation of the normal-mode frequencies away from stationary points is coordinate dependent. It has been argued that doing this analysis in curvilinear coordinates (where the results also depend on the specific choice of curvilinear coordinates) may be more robust than doing the analysis in rectilinear coordinates [148]. Here we did the analysis in rectilinear coordinates without any difficulties; however, this issue should be kept in mind in future applications.

Chapter 10.

Ionization thresholds of C$_3$H

Ionization of linear-C$_3$H and cyclic-C$_3$H is the final molecular system studied in this thesis using an approximate quantum model in reduced dimensionality using MP2-based potential energy surfaces and CCSD(T)/aug-cc-pVTZ electronic calculations at selected geometries. Briefly speaking, the essence of the strategy was first to determine the Franck-Condon factors associated with direct excitations from the ground vibrational state of the neutral C$_3$H to a range of vibrational states of C$_3$H cation. Such a Franck-Condon analysis was only done selectively for several key vibrational modes in this ionization process. On the basis of this analysis combined with a simple harmonic treatment of the energies of the remaining modes and key electronic energy differences obtained with CCSD(T)/aug-cc-pVTZ calculations, we obtained two distinguishable ionization thresholds for the two nearly isoenergetic species of C$_3$H, thresholds that could be applied to identify the two isomers.

10.1. Introduction

The reaction of C(^{3}P) with C$_2$H$_2$ to form C$_3$ + H$_2$ and C$_3$H + H has attracted a considerable amount of attention, both experimentally [149–163] and theoretically [164–170], due in part to the importance of the reaction in the interstellar medium, where the C$_3$H product has been detected. The experiment is challenging if ones wants to distinguish between the two nearly isoenergetic isomers of C$_3$H, i.e., linear and cyclic C$_3$H, denoted l-C$_3$H and c-C$_3$H, respectively, because conventional massspectrometric detection cannot be used for this purpose.

One technique that can be used to distinguish isomers formed in chemical reactions is threshold photoionization spectroscopy [171]; this could be a fruitful approach for the identification of the l-C$_3$H and c-C$_3$H products of the C(^{3}P) with C$_2$H$_2$ reaction. Previous studies have been reported on aspects of the ionization of C$_3$H. Ikuta reported the ionization energy of c-C$_3$H to be 9.06 eV at the MRCI/aug-cc-pVTZ level of theory/basis [172]. Chaudhuri et al. [173] performed high-level *ab initio* calculations of energy differences between l-C$_3$H and c-C$_3$H and the respective cations, and vertical ionization energies. They reported vertical ionization energies of 9.21 eV for l-C$_3$H using their calculated geometry and 9.33 eV using the experimental geometry, and 10.66 eV for c-C$_3$H for both their calculated and experimental geometry. Clearly there are significant differences between these two sets of calculations for the ionization of c-C$_3$H. Also, it should be noted that these calculations did not consider zero-point energy corrections and did not report Franck Condon factors for the ionization.

These systems are interesting and challenging for several reasons. Perhaps the most interesting one is, as tentatively reported earlier [172] and verified here, c-C$_3$H$^+$ does not exist as a stable minimum, but as a first-order saddle point. Thus the standard model of vertical photoionization of c-C$_3$H, which is a stable minimum, is

problematic. A second complication is that the l-C$_3$H minimum has been reported to be linear or slightly bent, depending on the level of *ab initio* theory and basis, whereas the l-C$_3$H$^+$ minimum is linear.

We investigate these interesting aspects of the photoionization of both isomers of C$_3$H in this paper. We do this by constructing full-dimensional potential energy surfaces for the neutral and cationic C$_3$H systems based on MP2/aug-cc-pVTZ calculations, doing reduced dimensionality calculations of Franck-Condon factors using these surfaces, and finally using CCSD(T)/aug-cc-pVTZ energies for certain key electronic energy differences.

The calculations and some details of the potential energy surface (PES) fitting are given in the next section as are relevant properties of the PESs and comparisons with previous *ab initio* calculations at stationary points. The reduced dimensionality Franck-Condon calculations are described and presented in Section 10.3 and a summary and conclusions are given in Section 10.4.

10.2. Ab initio Calculations and the Potential Energy Surfaces

We calculated MP2/aug-cc-pVTZ energy of 42 186 configurations using MOLPRO 2002 [11] for the case of C$_3$H and 17 812 for the case of C$_3$H$^+$. The fitting approach has been described in great details in Chapter 2. Briefly, for both surfaces we used a many-body expansion with Morse variable polynomials that are invariant with respect to permutation of the three C atoms up to total degree 8 for all the terms. With the fixed one-body potentials, which are the constant energies of single atoms, we have a total of 744 free coefficients for the 2-body, 3-body, and 4-body terms, altogether. The

present fits are semi-global in that they do don't describe fragmentation; however, they do describe the isomerization of C_3H and C_3H^+.
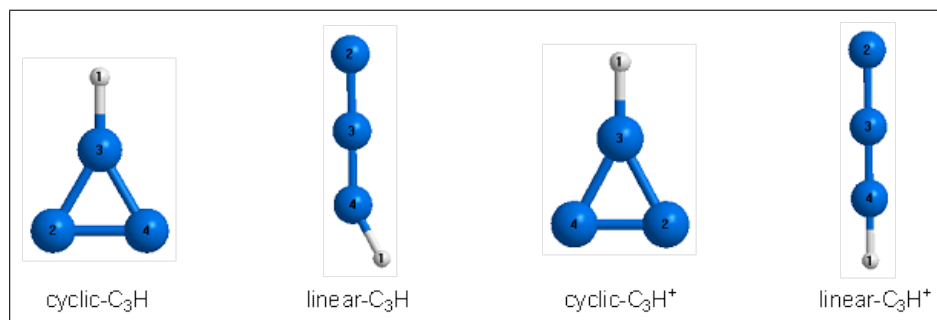
Figure 10.1. Equilibrium minimum structures of l-C_3H, l-C_3H^+, c-C_3H, and the saddle point structure of l-C_3H^+.

Stationary points are located on these PESs. These are shown graphically in Figure 10.1, where as seen the PES finds the minimum of l-C_3H to be slightly bent. There is generally excellent agreement for all structures with previous benchmark *ab initio* calculations[163, 172], with only slightly problematic one being the minimum for l-C_3H. Even with extensive electronic structure studies such as these, the controversy regarding whether the neutral C_3H potential has a double minimum feature with a small barrier in the bending coordinate or it is just a flat, anharmonic potential with a linear minimum remains unresolved. The present neutral PES indicates the former.

Table 10.1 contains the normal-mode frequencies and harmonic zero-point energies obtained from the PESs and results from previous *ab initio* calculations[163, 174]. It also contains a comparison of energies, relative to the global minimum energy of c-C_3H, of previous CCSD(T)/aug-cc-pVTZ calculations by Ikuta[172] at the geometries indicated in Figure 10.1 and also new CCSD(T)/aug-cc-pVTZ that we did at the PES stationary points. We see good agreement between the PES normal-mode frequencies for l-C_3H with those from previous CCSD(T)/TZP calculations[163], with the exception of modes 4 and 6. For c-C_3H the comparison shows good agreement with the calculations of Stanton[174] except for mode 1. As he discussed, there is a

Table 10.1. Harmonic frequencies (cm^{-1}) and zero-point energies (ZPE) from the PESs and other sources, as indicated. Also, energies (cm^{-1}) relative to the global minimum, c-C$_3$H, from the PESs, previous sources and the present CCSD(T)/aug-cc-pVTZ calculations done at the PES geometries.

	l-C$_3$H-linear	l-C$_3$H-bent	l-C$_3$H$^+$	c-C$_3$H	c-C$_3$H$^+$
Mode 1	417i^a		110^a		
Mode 2	417i	259^a, 208^b	110	718^a, 281^c	461i^a
Mode 3	289	289, 351	808	917, 898	873
Mode 4	289	581, 369	808	939, 957	1053
Mode 5	1162	1189, 1170	1199	1175, 1244	1457
Mode 6	1928	2011, 1876	2164	1508, 1639	1808
Mode 7	3387	3339, 3380	3291	3261, 3330	3241
ZPE	–	3833, 3677	4245	4260, 4175	4216
PES	2736	2436	74296	0	79963
ab initio^d	1014	1105	73197	0	79123
ab initio^e	949	–	73095	0	79049

^{a} Present PES; ^{b} CCSD(T)/TZP calculations from Ref. [163]; ^{c} CCSD(T)/EOM calculations from Ref. [174]; ^{d} Present CCSD(T)/aug-cc-pVTZ calculations. ^{e}CCSD(T)/aug-cc-pVTZ calculations from Ref. [172].

strong pseudo Jahn-Teller interaction, which is not accounted for in the present MP2 calculations and so that could be affecting the frequency of mode 1 from the PES.

Next consider a comparison of the energies given in the table. The PES results are in good agreement with the present and previous CCSD(T)/aug-cc-pVTZ[172] values, which are themselves in excellent agreement, considering the slight differences in the geometries used to obtain these energies. The PES energies and their difference for l-C$_3$H (linear and bent) are higher than the CCSD(T) ones and the order is reversed. This is essentially an error due to the MP2 method. For the present purpose of this paper the significant number is the height of the PES barrier between the linear and bent geometries of l-C$_3$H, which is 300 cm^{-1}. Although this value is higher than the 66 cm^{-1} barrier obtained at the highest level *ab initio* calculations, CCSD(T)/ cc-pVQZ, obtained at the CCSD(T)/TZP geometries [163], we show in the next section that the PES almost certainly describes the zero-point wavefunction l-C3H qualitatively correctly.

On the basis of the results in Table 10.1 using the present CCSD(T)/aug-cc-pVTZ calculations, we obtained rough estimates of the ionization thresholds. For c-C$_3$H the "vertical" ionization energy to the c-C$_3$H$^+$ saddle point is 9.8 eV and the vertical ionization energy for l-C$_3$H (linear) to l-C$_3$H$^+$ is roughly 8.95 eV. Given that some of the stationary points used in these estimates are saddle points, we stress that these can only be regarded as rough estimates. A treatment of the vibrational wave functions for the highly anharmonic imaginary modes is needed for a more precise treatment of the ionization process. We address this in the next section where we present a reduced dimensionality Franck-Condon analysis for these highly anharmonic modes.

10.3. Franck-Condon Analysis

10.3.1. Methodology

In the Franck-Condon approximation the threshold ionization region is described by the overlap of the neutral wave function (typically the ground state) with wave functions of the cation and the relevant electronic energy differences between the neutral and cationic wave functions. Franck-Condon factors (FCFs) are the squares of these overlaps. Obtaining FCFs in full-dimensionality for C$_3$H (six degrees of freedom) is a considerable challenge and we do not do that here.

A separable, harmonic model is certainly feasible; however, this would be inadequate for some modes of this system, as discussed in the previous section. Specifically c-C$_3$H$^+$ is a firstorder saddle point and also l-C$_3$H either is slightly bent or has a very flat bending potential. For these modes and the corresponding ones for c-C$_3$H and l-C$_3$H$^+$ we take a numerical approach to evaluate FCFs involving the highly nonharmonic modes. To do this, we identified the imaginary frequency modes of c-C$_3$H$^+$ and l-C$_3$H (linear) and then were able to identify very similar normal modes of c-C$_3$H and l-C$_3$H$^+$, respectively. We then obtained numerical potentials for these modes, corresponding numerical wave functions and finally numerical FCFs as described next.

First, consider the analysis for c-C$_3$H $\rightarrow$ c-C$_3$H$^+$. As noted, c-C$_3$H exists in a true minimum, whereas c-C$_3$H$^+$ is a saddle point. The imaginary frequency (mass-scaled) normal mode of c-C$_3$H$^+$ is shown in Figure 10.2 along with the normal mode of c-C$_3$H which most resembles the imaginary frequency one. These modes were obtained from the PESs and the mode of c-C$_3$H shown is labeled mode 2 in Table 10.1. Numerical FCFs for these two modes are then the ones of interest and we obtain them by assuming the normal modes are the same (obviously they are close but not identical) and so we ignore the "Duschinsky rotation" between them. We also ignore
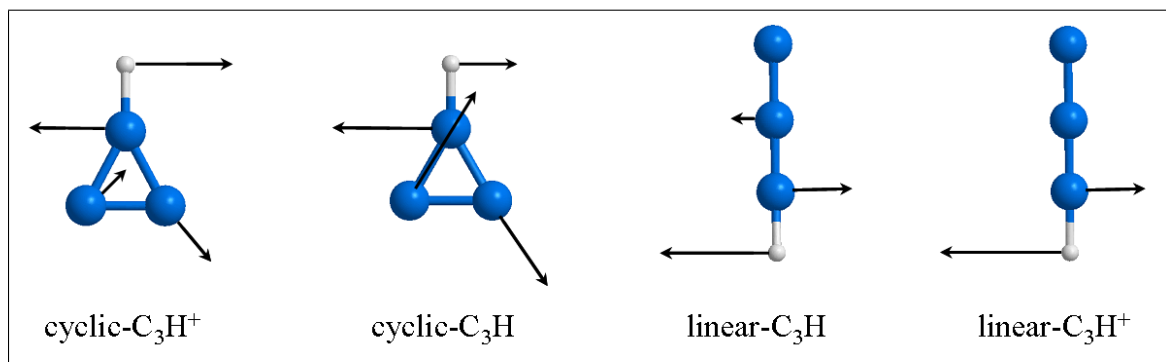
cyclic-C$_3$H$^+$ cyclic-C$_3$H   linear-C$_3$H   linear-C$_3$H$^+$

Figure 10.2. Imaginary-frequency normal mode of c-C$_3$H$^+$, corresponding real-frequency normal mode for c-C$_3$H, imaginary-frequency normal mode of l-C$_3$H, and corresponding real-frequency normal mode for l-C$_3$H$^+$.

small differences in the reference geometries of c-C$_3$H and c-C$_3$H$^+$. Thus, a direct calculation of the FCFs for these two modes assuming the normal modes are equal is a reasonable approximation.

Similar considerations for l-C$_3$H also lead to the conclusion that FCFs involving the imaginary frequency bending mode of l-C$_3$H in the linear geometry and an analogous bending mode in l-C$_3$H$^+$ should be a physically reasonable model. The relevant normal modes of the neutral and cation are also shown in Figure 10.2. The cation normal mode is the doubly degenerate bend with ω=808 cm^{-1}, and as seen, it is quite similar to the (doubly degenerate) imaginary frequency mode of l-C$_3$H (linear).

Having identified the imaginary frequency modes for c-C$_3$H$^+$ and l-C$_3$H and the similar real frequency ones for c-C$_3$H and l-C$_3$H$^+$ it remains to determine the corresponding potentials along these modes, all denoted generically as "Q", using the PESs and to solve the 1d Schrödinger equations for the eigenfunctions and eigenvalues. For the imaginary-frequency mode of c-C$_3$H$^+$ the full-dimensional PES was minimized with respect to the other normal modes as Q was varied starting at Q=0, the saddle point. The same procedure was followed for one of the two degenerate imaginary-frequency modes of l-C$_3$H (linear). The resulting potentials are shown in Figures 10.3 and 10.4, respectively, where we also show the relaxed potentials along

the corresponding real-frequency normal mode of c-C$_3$H and l-C$_3$H$^+$ in the respective figures. Note the potentials for the neutrals are zero at the local minima and the potentials for the corresponding cations include the electronic energy of the cation, measured relative to the zero potential value shown in these figures.

As seen in Figure 10.3, the relaxed c-C$_3$H$^+$ potential decreases from the saddle point value, where Q) 0, by 5700 cm^{-1} at the minimum, Q) (265, which corresponds to the l-C$_3$H$^+$ structure, as it should. (From Table 10.1 the precise energy difference is 5667 cm^{-1}.) Beyond this value of Q the potential rises steeply, resulting in a double-well potential over the range of Q shown. If Q were an angular variable, the potential would be periodic as the system would return to another c-C$_3$H$^+$ configuration. This does not occur with the rectilinear normal mode and so the potential shown is valid for the region of Q shown and wave functions obtained with this potential are realistic for energies not very far in excess of the barrier energy. (As we will see later, this is sufficient for our analysis.)

The relaxed potential for the imaginary-frequency mode of l-C$_3$H is shown in Figure 10.4. As seen, this is a double well potential, as expected, with a barrier height of 300 cm^{-1}. The corresponding potential for l-C$_3$H$^+$ along the bending normal mode that is close in character to the imaginary frequency one of l-C$_3$H is also shown in this figure. As seen, it is, to a good approximation, quite harmonic.

The analytical expression of the four potentials was obtained using the cubic-spline formula. The Schrödinger equation was the solved for these four potentials, using the equally spaced "Discrete Variable Representation" of the Cartesian kinetic energy operator due to Colbert and Miller [140]. The resulted Hamiltonian matrices were diagonalized using standard Math Library in Fortran 90. The convergence of the calculations are achieved by increasing the number of grid points in DVR basis. Numerical methods used have been described in Section 9.2.2 of Chapter 9.
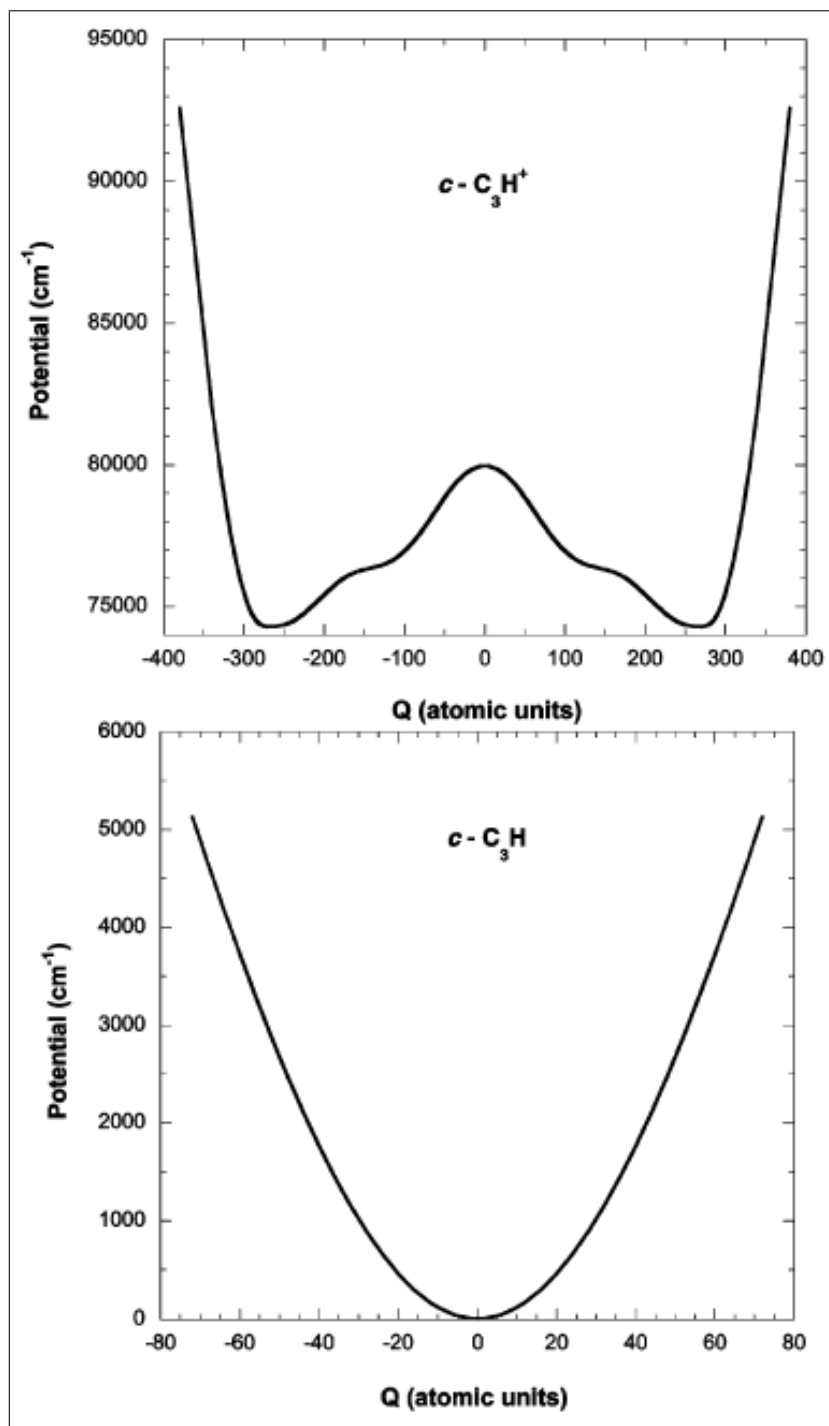
Figure 10.3. Relaxed potential for the imaginary frequency mode of c-C$_3$H$^+$ (top) and corresponding potential for the real frequency mode for c-C$_3$H (bottom).
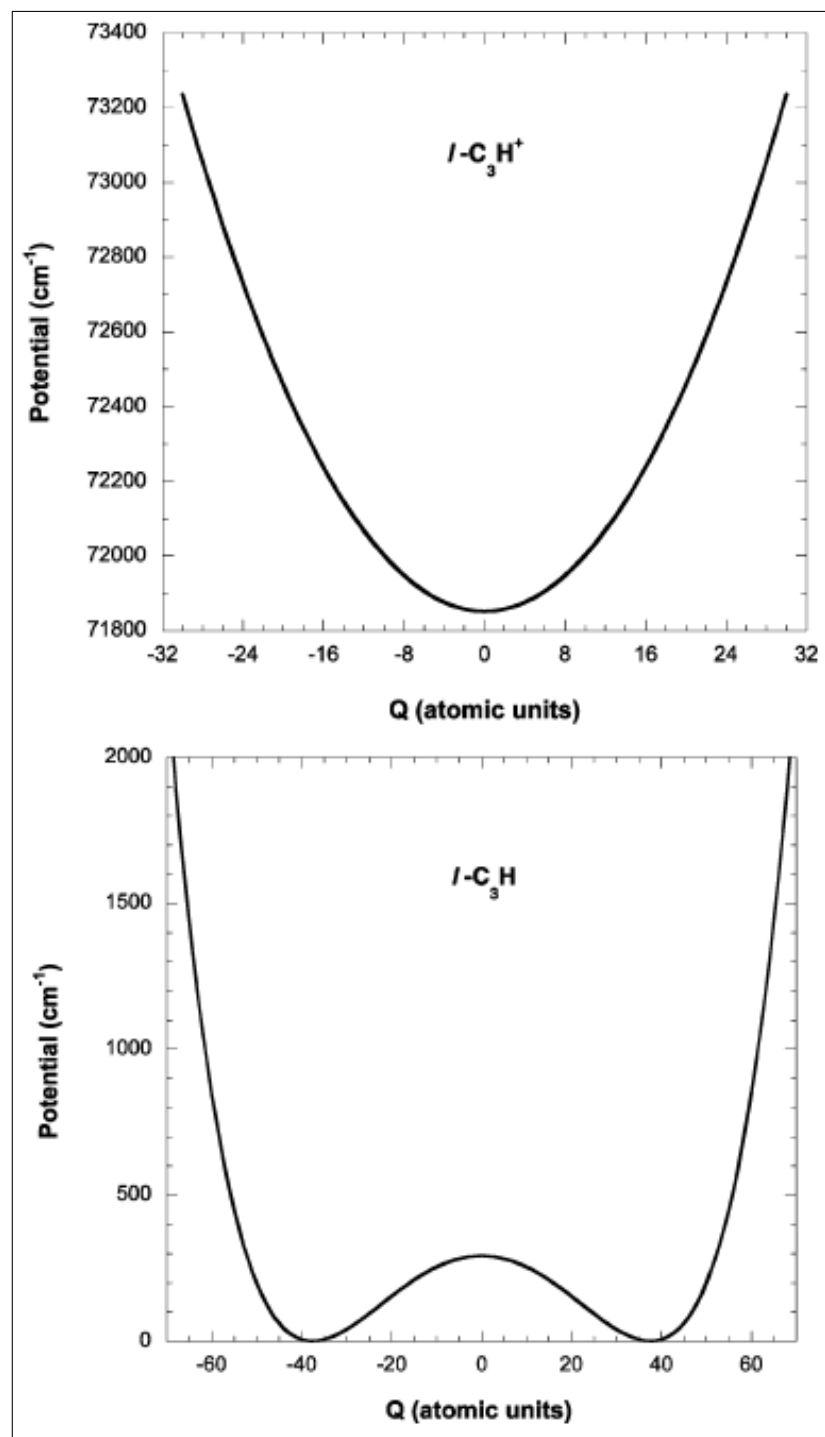
Figure 10.4. Relaxed potential for the real frequency mode of l-C$_3$H$^+$ (top) and corresponding potential for the imaginary frequency mode for l-C$_3$H (bottom).

Franck-Condon factors were then calculated numerically from these wave functions but restricted to the ground state wave functions for the neutrals, c-C$_3$H and l-C$_3$H.

10.3.2. Results and discussion

The ground state wave function for the imaginary-frequency mode of l-C$_3$H, with potential given in Figure 10.4, is shown in Figure 10.5. The energy of this wave function, 215 cm^{-1}, is slightly below the barrier height of 300 cm^{-1}. As a result, the function has a small dip at Q=0 and two peaks at approximately Q=$\pm$40, where the numerical potential has identical minima. However, as seen, the wave function has considerable amplitude at Q=0 and thus can be accurately characterized as being delocalized over the two minima and saddle point. This delocalization essentially removes the concern over whether the l-C$_3$H has its minimum at the linear geometry or a slightly bent one.

The ground state wave function for c-C$_3$H is shown in Figure 10.6 along with the excited state wave function of c-C$_3$H$^+$ that has the maximum overlap with it, and hence the largest FCF. The energy of this excited state wave function is 5700 cm^{-1}, relative to the minimum of the potential for the cation, plotted in Figure 10.3. This energy is nearly identical to the barrier height shown in that figure and, as expected, the wave function is concentrated in the region of the barrier, and thus has a substantial overlap with the ground state wave function of c-C$_3$H.

The results of the Franck-Condon calculations are given in Figure 10.7, where FCFs are plotted versus energy. These FCFs are only for the 1d wave functions obtained from the four numerical potentials presented above. FCFs for all other modes were not calculated under the assumption that the largest FCF would be for
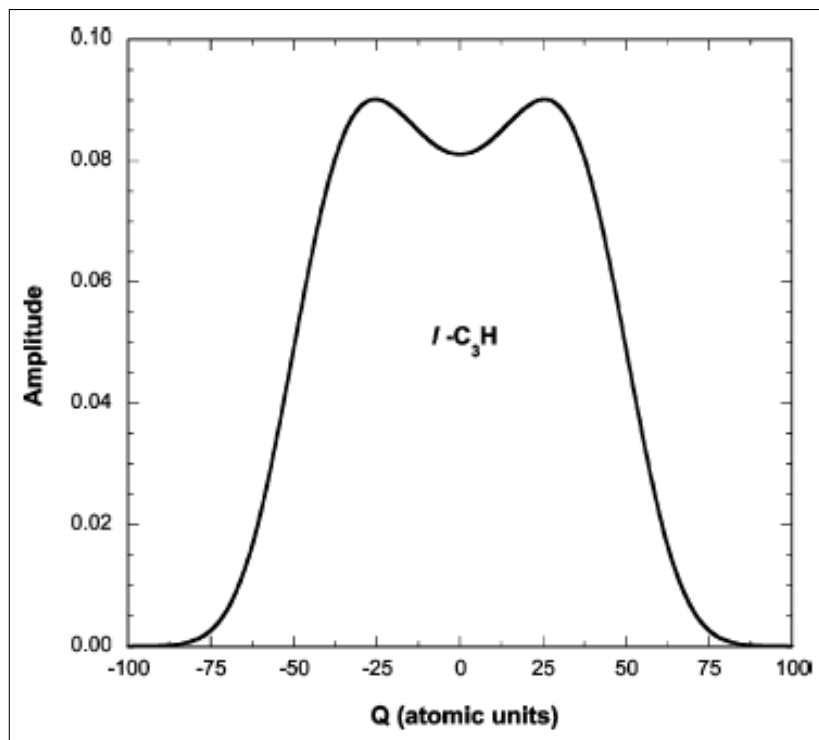
Figure 10.5. Ground state vibrational wavefunction for the relaxed potential of the imaginary frequency mode of l-C$_3$H shown in Figure 10.4

the ground state to ground state transitions for these modes. This follows primarily from the similarity of the relevant neutral and cation equilibrium geometries.

Before discussing the FCFs, we explain how the energy axis was determined. Basically, these energies are differences in the full-dimensional ZPE for the two neutral species and the cations for which FCFs were calculated plus an appropriate electronic energy difference. The electronic energy differences were obtained from CCSD(T)/aug-cc-pVTZ calculations at the relevant PES geometries described below instead of the MP2 energy differences from the two PESs because the former energies are more accurate than the latter ones. For l-C$_3$H the full dimensional ZPE was obtained as the sum of the harmonic ZPE of all real-frequency modes of l-C$_3$H plus the ZPE obtained numerically for the doubly degenerate imaginary-frequency mode. The ZPE of c-C$_3$H was obtained similarly as the sum of the ZPE of the wave function shown in Figure 10.7 plus the harmonic ZPEs and for all other c-C$_3$H
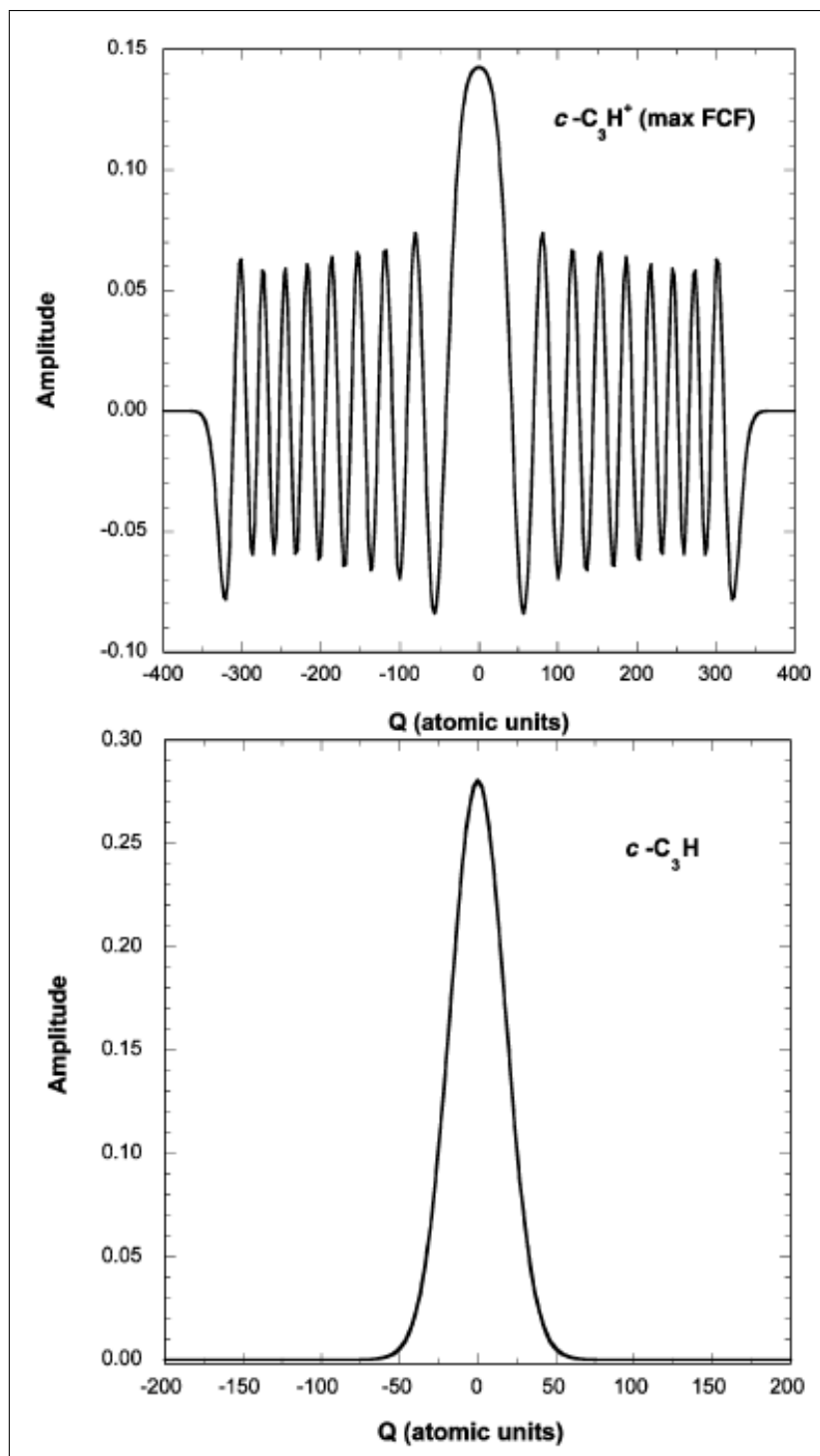
Figure 10.6. Ground state vibrational wave function for the relaxed potential of the real frequency mode of c-C$_3$H shown in Figure 10.3 (top) and the excited state vibrational wave function of c-C$_3$H$^+$ from the potential shown in Figure 10.3 (bottom) with the maximum overlap with the ground state wave function of c-C$_3$H.

modes. For l-C$_3$H$^+$ the vibrational energies are the sum of the harmonic ZPEs for all real-frequency modes plus the numerically determined vibrational energies of wave functions determined from the potential shown in Figure 10.4. Relative to this origin, the cation energy for the l-C$_3$H FCFs was obtained using the accurate CCSD(T)/aug-cc-pVTZ energy difference between the equilibrium structures of l-C$_3$H (slightly bent) and l-C$_3$H$^+$ (linear) plus the vibrational energies of l-C$_3$H$^+$ obtained relative to the equilibrium structure of l-C$_3$H$^+$. The same procedure was followed for the energies of the FCFs for c-C$_3$H$^+$ with the origin of the 1d vibrational energies being the l-C$_3$H$^+$ equilibrium. The real-frequency modes of c-C$_3$H$^+$ are the ones at the saddle point geometry. The relevant electronic energy difference is the electronic energy of the equilibrium structure of c-C$_3$H and the electronic energy of l-C$_3$H$^+$ equilibrium, again obtained using CCSD(T)/aug-cc-pVTZ energies instead of the PES values.

Returning now to Figure 10.7 and considering first the FCFs for l-C$_3$H $\rightarrow$ l-C$_3$H$^+$ we see, as expected, a "textbook" progression with the largest FCF corresponding to the adiabatic transition, *i.e.*, to the ground vibrational state of l-C$_3$H$^+$. The energy of this transition is 9.06 eV, and this represents the present vaule of the threshold energy for l-C3H ionization. This value is 0.11 eV above the vertical ionization energy, without ZPE correction, of 8.95 eV given in the previous section.

Consider now the FCFs for c-C$_3$H $\rightarrow$ c-C$_3$H$^+$. As seen, the maximum FCF occurs at 9.76 eV (the cation wave function corresponding to the FCF was shown in Figure 10.6), which is quite close to the vertical energy estimate to the saddle point of 9.8 eV given in the previous section. However, there are significant FCFs at lower energies, making the assignment of a threshold energy somewhat problematic. With this in mind a threshold ionization of c-C$_3$H in the range 9.70-9.76 eV is reasonable.

The present calculations of the threshold IPs will hopefully be of use in experimental determinations of them. A partial validation of the calculations does exist

from a recent experiment, which reported a threshold IP of 9.7±0.2 eV [175, 176], however, without resolving which isomer or isomers the measurement corresponds. The present calculations point to the c-C$_3$H isomer.
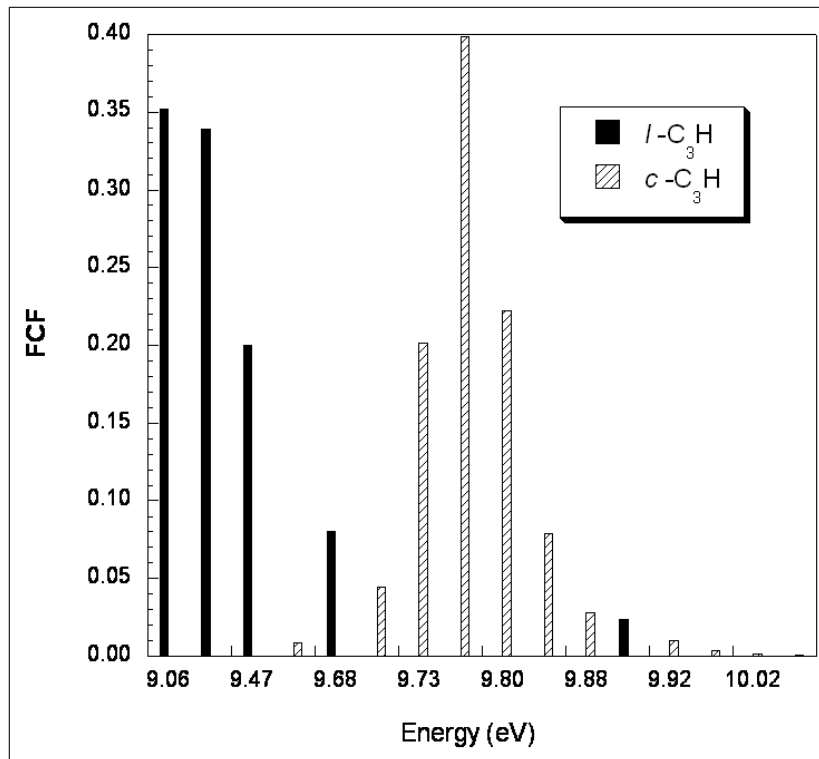

Figure 10.7. Franck-Condon factors for l-C$_3$H and c-C$_3$H ionization vs energy. See the text for a discussion of the energy axis.

10.4. Summary

We presented a Franck-Condon analysis in reduced dimensionality for the ionization thresholds of l-C$_3$H and c-C$_3$H using MP2-based potential energy surfaces and CCSD(T)/aug-cc-pVTZ calculations of electronic energies at selected geometries. Comparisons were made with previous electronic structure calculations for stationary point geometries and energies of the neutrals and cations.

Relaxed numerical potentials were determined along the imaginary frequency mode of c-C$_3$H$^+$, which exists as a first order saddle point, and also along the imaginary frequency mode of l-C$_3$H, which on our PES also exhibits a saddle point structure at the strictly linear geometry. Corresponding, similar normal modes were identified for the c-C$_3$H and l-C$_3$H$^+$, and numerical potentials were also determined along these modes. Numerical solutions to the 1d Schroödinger were obtained and used to calculate the 1d Franck-Condon factors describing the ionization of l-C$_3$H and c-C$_3$H. From these results we reported ionization thresholds of 9.06 and 9.70-9.76 eV, respectively. These results differ from previous estimates in the literature, especially for c-C$_3$H, which did not consider a Franck-Condon analysis. Given the approximations made in this analysis we estimate that the present ionization energies are accurate to within roughly ± 0.05eV.

Bibliography

[1] M. Born and J. R. Oppenheimer, Ann. Physik. **84**, 457 (1927)

[2] S. L. Zou and J. M. Bowman, Chem. Phys. Lett. **368**, 421 (2003)

[3] X. B. Zhang, S. L. Zou, L. B. Harding, and J. M. Joel, J. Phys. Chem. A **108**, 8980 (2004)

[4] J. N. Murrell, S. Carter, S. C. Farantos, P. Huxley, and A. J. C. Varandas, *Molecular potential energy functions* (John Wiley & Sons, Chichester, 1984)

[5] Schmelzer A. and J. N. Murrell, Int. J. Quant. Chem. **2**, 287 (1985)

[6] B. J. Braams and J. M. Bowman, Int. Rev. Phys. Chem. **28**, 577 (2009)

[7] Z. Xie and J. M. Bowman, J. Chem. Theory Comput. **6**, 26 (2010)

[8] H. Derksen and G. Kemper, *Computational Invariant Theory* (Springer Verlag, Berlin, 2002)

[9] W. Bosma, J. Cannon, and C. Playoust, J. Symbolic Comput. **24**, 235–265 (1997)

[10] *Handbook of Magma Functions*, 2nd ed., edited by J. J. Cannon and W. Bosma (2007) see http://magma.maths.usyd.edu.au/magma/htmlhelp/MAGMA.htm

[11] H.-J. Werner, P. J. Knowles, R. Lindh, F. R. Manby, M. Schütz, P. Celani,

T. Korona, G. Rauhut, R. D. Amos, A. Bernhardsson, A. Berning, D. L. Cooper, M. J. O. Deegan, A. J. Dobbyn, F. Eckert, C. Hampel, G. Hetzer, A. W. Lloyd, S. J. McNicholas, W. Meyer, M. E. Mura, P. Palmieri A. Nicklass, R. Pitzer, U. Schumann, H. Stoll, A. J. Stone, R. Tarroni, and T. Thorsteinsson, *MOLPRO* (2006), version 2002.1, 2006.1

[12] X. Huang, B. J. Braams, and J. M. Bowman, J. Phys. Chem. A **110**, 445 (2006)

[13] X. Huang, B. J. Braams, J. M. Bowman, R. E. A. Kelly, J. Tennyson, G. C. Groenenboom, and A. van der Avoird, J. Chem. Phys. **128**, 034312 (2008)

[14] Y. Shank, A. Wang, A. Kaledin, B. J. Braams, and J. M. Bowman, J. Chem. Phys. **120**, 144314 (2009)

[15] Z. Xie, B. J. Braams, and J. M. Bowman, J. Chem. Phys. **122**, 224307 (2005)

[16] U. Niessar, G. Corongiu, E. Clementi, G.R. Kneller, and D.K. Bhattacharya, J. Phys. Chem. **94**, 7949 (1990)

[17] K. Szalewicz, C. Leforestier, and A. van der Avoird, Chem. Phys. Lett. **482**, 1 (2009)

[18] G. S. Fanourgakis and S. S. Xantheas, J. Chem. Phys. **128**, 074506 (2008)

[19] R. Kumar, F.-F. Wang, G. R. Jenness, and K. D. Jordan, J. Chem. Phys. **132**, 014309 (2010)

[20] F. Paesani, S. S. Xantheas, and G. A. Voth, J. Phys. Chem. B **113**, 5702 (2009)

[21] G. S. Fanourgakis S. Habershon and D. E. Manolopoulos, J. Chem. Phys. **129**, 074501 (2008)

[22] R. Bukowski, K. Szalewicz, G. C. Groenenboom, and A. van der Avoird, Science **315**, 1249 (2007)

[23] R. Bukowski, K. Szalewicz, G. C. Groenenboom, and A. van der Avoird, J. Chem. Phys. **128**, 094314 (2008)

[24] E. M. Mas, R. Bukowski, and K. Szalewicz, J. Chem. Phys. **118**, 4386 (2003)

[25] W. Cencek, K. Szalewicz, C. Leforestier, R. van Harrevelt, and A. van der Avoird, Phys. Chem. Chem. Phys. **10**, 4716 (2008)

[26] C. Leforestier, R. van Harrevelt, and A. van der Avoird, J. Phys. Chem. A **113**, 12285 (2009)

[27] L. B. Braly, J. D. Cruzan, K. Liu, R. S. Fellers, and R. J. Saykally, J. Chem. Phys. **112**, 10293 (2000)

[28] L. B. Braly, K. Liu, M. G. Brown, F. N. Keutsch, R. S. Fellers, and R. J. Saykally, J. Chem. Phys. **112**, 10314 (2000)

[29] T. Taketsugu and D. Wales, Molec. Phys. **100**, 2793 (2002)

[30] G. S. Tschumper, M. L. Leininger, B. C. Hoffman, E. F. Valeev, H. F. Schaefer III, and M. Quack, J. Chem. Phys. **116**, 690 (2002)

[31] S. S. Xantheas, C. J. Burnham, and R. J. Harrison, J. Chem. Phys. **116**, 1493 (2002)

[32] S. F. Boys and F. Bernardi, Molec. Phys. **19**, 553 (1970)

[33] H.-J. Werner and P. J. Knowles, Theor. Chim. Acta. **78**, 175 (1990)

[34] R. J. Gdanitz and R. Ahlrichs, Chem. Phys. Lett. **143**, 413 (1988)

[35] T. H. Dunning, Jr., J. Chem. Phys. **90**, 1007 (1989)

[36] S. S. Xantheas, Chem. Phys. **258**, 225 (2000)

[37] E. Dahlke, R.M. Olson, H.R. Leverentz, and D.G. Truhlar, J. Phys. Chem. A

112, 2976 (2008)

[38] S. Maheshwary, N. Patel, N. Sathyamurthy, A. D. Kulkarni, and S. R. Gadre, J. Phys. Chem. A **105**, 10525 (2001)

[39] J. A. Anderson, K. Crager, L. Fedoroff, and G. S. Tschumper, J. Chem. Phys. **121**, 110023 (2004)

[40] J. K. Gregory and D. C. Clary, J. Phys. Chem. A **101**, 6813 (1997)

[41] K. Liu, M. G. Brown, C. Carter, R. J. Saykally, J. K. Gregory, and D. C. Clary, Nature **381**, 501 (1996)

[42] K. Nauta and R. E. Miller, Science **287**, 293 (2000)

[43] D.M. Bates and G.S. Tschumper, J. Phys. Chem. A **113**, 3555 (2009)

[44] B. Santra, A. Michaelides, M. Fuchs, A. Tkatchenko, C. Filippi, and M. Scheffler, J. Chem. Phys. **129**, 194111 (2008)

[45] H.-J. Werner and K. Pflüger, Annu. Rep. Comp. Chem. **2**, 53 (2006)

[46] R. Polly, H.-J. Werner, F. R. Manby, and P. J. Knowles, Molec. Phys. **102**, 2311 (2004)

[47] M. Schütz and H.-J. Werner, J. Chem. Phys. **114**, 661 (2001)

[48] J. B. Anderson, J. Chem. Phys. **63**, 1499 (1975)

[49] J. B. Anderson, J. Chem. Phys. **65**, 4121 (1976)

[50] R. P. Feynman and A. R. Hibbs, *Quantum mechanics and path integral* (McGraw-Hill, New York, 1965)

[51] Ioan Kosztin, Byron Faber, and Klaus Schulten, Am. J. Phys. **64**, 633 (1996)

[52] M. B. Priestley, "Spectral analysis and time series," (Academic, London, 1981)

Chap. 5-7

[53] T. W. Anderson, *The Statistical Analysis of Time Series* (Wiley, New York, 1971)

[54] N. Madras, J. Stat. Phys. **50**, 109 (1988)

[55] J. M. Bowman, S. Carter, and X. Huang, Int. Rev. Phys. Chem. **22**, 533 (2003)

[56] S. Carter, J. M. Bowman, and N. C. Handy, Theor. Chem. Account. **100**, 191 (1998)

[57] J. K. G. Watson, Molec. Phys. **15**, 479 (1968)

[58] S. Carter, S Culik, and J. M. Bowman, J. Chem. Phys. **107**, 10458 (1997)

[59] J. M. Bowman, J. Chem. Phys. **68**, 608 (1978)

[60] J. M. Bowman, Acc. Chem. Rev. **18**, 202 (1986)

[61] S. Carter, J. M. Bowman, and L. B. Harding, Spectrochim. Acta A **53**, 1179 (1997)

[62] Burcl R., S. Carter, and N. C. Handy, Chem. Phys. Lett. **380**, 237 (2003)

[63] A. R. Carter, S. Sharma, J. M. Bowman, P. Rosmus, and R. Tarroni, J. Chem. Phys. **131**, 224106 (2009)

[64] D. W. Firth, K. Beyer, M. A. Dvorak, S. W. Reeve, A. Q. Gushow, and K. Leopold, J. Chem. Phys. **94**, 1812 (1991)

[65] T. Baba, T. Tanaka, I. Morino, K. M. T. Yamada, and K. Tanaka, J. Chem. Phys. **110**, 4131 (1999)

[66] S. L. Baughcum, Z. Smith, E. B. Wilson, and R. W. Duerst, J. Am. Chem. Soc. **106**, 2260 (1984)

[67] T. Carrington and W. H. Miller, J. Chem. Phys. **84**, 4364 (1986)

[68] B. A. Ruf and W. H. Miller, J. Chem. Soc. Faraday Trans. **84**, 1523 (1988)

[69] N. Makri and W. H. Miller, J. Chem. Phys. **91**, 4026 (1989)

[70] N. Shida, P. F. Barbara, and J. E. Almolöf, J. Chem. Phys. **91**, 4061 (1989)

[71] T. D. Sewell, Y. Guo, and D. L. Thompson, J. Chem. Phys. **103**, 8557 (1995)

[72] M. Ben-Nun and T. Marttnez, J. Phys. Chem. A **103**, 6055 (1999)

[73] P. P. Schmidt, Molec. Phys. **105**, 1217 (2007)

[74] K. Yagi, T. Taketsugu, and K. Hirao, J. Chem. Phys. **115**, 10647 (2001)

[75] G. V. Mil'nikov, K. Yagi, T. Taketsugu, H. Nakamura, and K. Hirao, J. Chem. Phys. **120**, 5036 (2004)

[76] G. V. Mil'nikov, K. Yagi, T. Taketsugu, H. Nakamura, and K. Hirao, J. Chem. Phys. **119**, 10 (2003)

[77] A. Viel, M. D. Coutinho-Neto, and U. Manthe, J. Chem. Phys. **126**, 024308 (2007)

[78] R. Ahlrichs, M. Baer, M. Haeser, H. Horn, and C. Koelmel, Chem. Phys. Lett. **162**, 165 (1989)

[79] C. Hättig and Weigend F., J. Chem. Phys. **113**, 5154 (2000)

[80] F. A. Bischoff, S. Höfener, A. Glöß, and W. Klopper, Theor. Chem. Account. **121**, 11 (2008)

[81] S. Höfener, F. A. Bischoff, A. Glöß, and W. Klopper, Phys. Chem. Chem. Phys. **10**, 3390 (2008)

[82] D. P. Tew and W. Klopper, J. Chem. Phys. **123**, 074101 (2005)

[83] S. Ten-no, J. Chem. Phys. **126**, 014108 (2007)

[84] W. Klopper and C. C. Samson, J. Chem. Phys. **116**, 6397 (2002)

[85] Stanislav Kedžuch, Matú Milko, and Jozef Noga, "Alternative formulation of the matrix elements in mp2-r12 theory," International Journal of Quantum Chemistry **105**, 929–936 (2005)

[86] E. F. Valeev, Chem. Phys. Lett. **395**, 190 (2004)

[87] F. Weigend, A. Köhn, and C. Hättig, J. Chem. Phys. **116**, 3175 (2002)

[88] C. Hättig, unpublished

[89] R. A. Kendall, T. H. Dunning, Jr., and R. J. Harrison, J. Chem. Phys. **96**, 6796 (1992)

[90] S. T. Baughcum, R. W. Duerst, W. F. Rowe, Z. Smith, and E. B. Wilson, J. Am. Chem. Soc. **103**, 6296 (1981)

[91] V. Barone and C. Adamo, J. Chem. Phys. **105**, 11007 (1996)

[92] A. Brown, A. B. McCoy, B. J. Braams, Z. Jin, and M. J. Bowman, J. Chem. Phys. **121**, 4105 (2004)

[93] D. P. Tew, N. C. Handy, S. Carter, S. Irle, and J. M. Bowman, Molec. Phys. **101**, 3513 (2003)

[94] D. P. Tew, N. C. Handy, and S. Carter, Molec. Phys. **102**, 2217 (2004)

[95] D. P. Tew, N. C. Handy, and S. Carter, J. Chem. Phys. **125**, 084313 (2006)

[96] T. R. Geballe and T. Oka, Nature **384**, 334 (1996)

[97] B. McCall and T. Oka, Science **287**, 1941 (2000)

[98] S. Miller and J. Tennyson, Chem. Soc. Rev. **21**, 281 (1992)

[99] K. Giles, N. G. Adams, and D. Smith, J. Phys. Chem. **96**, 7645 (1992)

[100] M. Cordonnier, D. Uy, R. M. Dickson, K. E. Kerr, Y. Zhang, and T. Oka, J. Chem. Phys. **113**, 3181 (2000)

[101] D. Gerlich, F. Windisch, P. Hlavenka, R. Plašil, and J. Glosik, Phil. Trans. R. Soc. London, Ser. A **364**, 3007 (2006)

[102] E. Hugo, O. Asvany, and S. Schlemmer, J. Chem. Phys. **130**, 164302 (2009)

[103] M. Okumura, L. I. Yeh, and Y. T. Lee, J. Chem. Phys. **88**, 79 (1988)

[104] Y. Yamaguchi, J. F. Gaw, R. B. Remington, and III. Schaeffer, H. F., J. Chem. Phys. **86**, 5072 (1987)

[105] P. H. Acioli, Z. Xie, B. J. Braams, and J. M. Bowman, J. Chem. Phys. **128**, 104318 (2008)

[106] W. P. Kraemer, V. Špirko, and O. Bludsky, J. Mol. Spectrosc. **164**, 500 (1994)

[107] J. Headrick, E. G. Diken, R. S. Walters, N. I. Hammer, R. A. Christie, J. Cui, E. M. Myshakin, M. A. Duncan, M. A. Johnson, and K. D. Jordan, Science **308**, 1765 (2005)

[108] J. R. Roscioli, L. R. McCunn, and M. A. Johnson, Science **316**, 249 (2007)

[109] G. E. Douberly, A. M. Ricks, B. W. Ticknor, and M. A. Duncan, J. Phys. Chem. A **112**, 950 (2008)

[110] A. M. Ricks, G. E. Douberly, and M. A. Duncan, J. Chem. Phys. **131**, 104312 (2009)

[111] A. B. McCoy, X. Huang, S. Carter, and J. M. Bowman, J. Chem. Phys. **123**, 064317 (2005)

[112] O. Vendrell, F. Gatti, and H.-D. Meyer, J. Chem. Phys. **131**, 034308 (2009)

[113] A. B. McCoy, Int. Rev. Phys. Chem. **25**, 77 (2006)

[114] S. Carter and N. C. Handy, J. Chem. Phys. **113**, 987 (2000)

[115] B. Auer, R. Kumar, J. R. Schmidt, and J. L. Skinner, Proc. Natl. Acad. Sci. USA **104**, 14215 (2007)

[116] B. M. Auer and J. L. Skinner, J. Chem. Phys. **128**, 224511 (2008)

[117] H. Romanowski, J. M. Bowman, and L. B. Harding, J. Chem. Phys. **82**, 4155 (1985)

[118] R. T. Lawton and M. S. Child, Molec. Phys. **37**, 1799 (1979)

[119] H. Partridge and D. W. Schwenke, J. Chem. Phys. **106**, 4618 (1997)

[120] G. R. Low and H. G. Kjaergaard, J. Chem. Phys. **110**, 9104 (1999)

[121] D. P. Schofield and H. G. Kjaergaard, Phys. Chem. Chem. Phys. **5**, 3100 (2003)

[122] M. E. Dunn, T. M. Evans, K. N. Kirschner, and G. C. Shields, J. Phys. Chem. A **110**, 303 (2006)

[123] J. B. Paul, R. A. Provencal, C. Chapo, K. Roth, R. Casaes, and R. J. Saykally, J. Phys. Chem. A **103**, 2972 (1999)

[124] F. Huisken, M. Kaloudis, and A. Kulcke, J. Chem. Phys. **104**, 17 (1996)

[125] Z. S. Huang and R. E. Miller, J. Chem. Phys. **91**, 6613 (1989)

[126] K. Kuyanov-Prozument, M. Y. Choi, and A. F. Vilesov, J. Chem. Phys. **132**, 014304 (2010)

[127] J. B. Paul, C. P. Colher, R. J. Saykally, J. J. Scherer, , and A. O'Keefe, J. Phys. Chem. A **101**, 5211 (1997)

[128] J. E. Bertie and Z. Lan, Appl. Spectrosc. **50**, 1047 (1996)

[129] Y. Wang, B. J. Braams, S. Carter, D. P. Tew, and J. M. Bowman, J. Chem. Phys. **128**, 224318 (2008)

[130] E. Wigner, Z. Phys. Chem. Abt. B **19**, 203 (1932)

[131] R. Marcus, J. Chem. Phys. **43**, 1598 (165)

[132] K. Fukui, J. Phys. Chem. **74**, 4161 (1970)

[133] L. Hofacker, Z. Naturforsch. B **43**, 1598 (1965)

[134] W. H. Miller, N. Handy, and J. Adams, J. Chem. Phys. **72**, 99 (1980)

[135] T. Seideman and W. H. Miller, J. Chem. Phys. **96**, 4412 (1992)

[136] T. Seideman and W. H. Miller, J. Chem. Phys. **97**, 2499 (1992)

[137] T. Wu, H.-J. Werner, and U. Manthe, J. Chem. Phys. **124**, 164307 (2006)

[138] J. M. Bowman, X. Huang, and S. Carter, Spectrochim. Acta A **58**, 839 (2002)

[139] C. Leonard, N. Handy, J. Bowman, and S. Carter, Spectrochim. Acta A **58**, 825 (2002)

[140] D. Colbert and W. H. Miller, J. Chem. Phys. **96**, 992 (1982)

[141] D. G. Truhlar and C. J. Horowitz, J. Chem. Phys. **68**, 2466 (1978)

[142] J. Dai and J. Zhang, J. Chem. Phys. **93**, 699 (1997)

[143] E. C. Kemble, *The Fundamental Principles of Quantum Mechanics* (McGraw-Hill, New York, 1937)

[144] J. M. Bowman, J. Phys. Chem. **95**, 4960 (1991)

[145] R. A. Marcus and M. E. Coltrin, J. Chem. Phys. **67**, 2609 (1977)

[146] J. C. Corchado, Y. Y. Chuang, P. L. Fast, W. P Hu, Y. P Liu, G. C. Lynch, K. A. Nguyen, C. F. Jackels, A. F. Ramos, B. A. Ellingson, B. J. Lynch, J. Zheng, V. S. Melissas, J. Villà, I. Rossi, E. L. Coitino, J. Pu, T. V. Albu, R. Steckler, B. C. Garrett, A. D. Isaacson, and D. G. Truhlar, *PLOYRATE*, University of Minnesota, Minneapolis (2007), version 9.7

[147] G. V. Mil'nikov, K. Yagi, T. Taketsugu, H. Nakamura, and K. Hirao, J. Chem. Phys. **120**, 5036 (2004)

[148] C. F. Jackels, Z. Gu, and D. G. Truhlar, J. Chem. Phys. **102**, 3188 (1995)

[149] D. C. Clary, E. Buonomo, I. R. Sims, W. M. Smith, W. D. Geppert, C. Naulin, M. Costes, L. Cartechini, and P. Casavecchia, J. Phys. Chem. A **106**, 5541 (2002)

[150] I. W. M. Smith, Chem. Soc. Rev. **31**, 137 (2003)

[151] R. I. Kaiser, T. N. Le, T. L. Nguyen, A. M. Mebel, N. Balucani, Y. T. Lee, T. Stahl, P. V. R. Schleyer, and H. F. Schaefer III, Faraday Discuss. **119**, 51 (2001)

[152] D. C. Clary, N. Haider, D. Husain, and M. Kabir, Astrophys. J. **422**, 416 (1994)

[153] B. E. Turner, E. Herbst, and R. Terzieva, J. Suppl. Ser. **126**, 427 (2000)

[154] J. Keene, K. Young, T. G. Philips, and T. H. Buttegenbach, Astrophys. J. **415**, L131 (1993)

[155] R. I. Kaiser, C. Ochsenfeld, M. Head-Gordon, Y. T. Lee, and A. G. Suits, J. Chem. Phys. **106**, 1729 (1997)

[156] N. Haider and D. J. Husain, J. Chem. Soc. Faraday Trans. **89**, 7 (1993)

[157] D. Chastaing, P. L. James, I. R. Sims, and I. W. Smith, Phys. Chem. Chem.

Phys. **1**, 1729 (1999)

[158] D. Chastaing, S. D. Le Picard, I. R. Sims, and I. W. Smith, Astron. Astrophys. **365**, 241 (2001)

[159] R. I. Kaiser, D. Stranges, Y. T. Lee, and A. G. Suits, Astrophys. J. **477**, 982 (1997)

[160] R. I. Kaiser, A. M. Mebel, and Y. T. Lee, J. Chem. Phys. **114**, 231 (2001)

[161] L. Cartechini, A. Bergeat, G. Capozza, P. Casavecchia, G. G. Volpi, W. D. Geppert, C. Naulin, and M. Costes, J. Chem. Phys. **116**, 5603 (2002)

[162] M. Costes, N. Daugey, C. Naulin, A. Bergeat, F. Leonori, E. Segoloni, N. Petrucci, R. Balucani, and P. Casavecchia, Faraday Discuss. Chem. Soc. **133**, 157 (2006)

[163] C. Ochsenfeld, R. I. Kaiser, Y. T. Lee, A. G. Suits, and M. Head-Gordon, J. Chem. Phys. **106**, 4141 (1997)

[164] J. Takahashi and K. Yashimata, J. Chem. Phys. **104**, 6613 (1996)

[165] R. Guadagnini, G. C. Schatz, and S. P. Walch, J. Phys. Chem. A **102**, 5857 (1998)

[166] A. M. Mebel, W. M. Jackson, A. H. H. Chang, and S. H. Lin, J. Am. Chem. Soc. **120**, 5751 (1998)

[167] E. Buonomo and D. C. Clary, J. Phys. Chem. A **105**, 2694 (2001)

[168] T. Takayanagi, Chem. Phys. **312**, 61 (2005)

[169] T. Takayanagi, J. Phys. Chem. A **110**, 361 (2006)

[170] W. K. Park, S. C. Park, B. J. Braams, C. Chen, and Bowman. J. M., J. Chem.

Phys. **125**, 081101 (2006)

[171] T. A. See for example, Cool, K. Nakajima, T. A. Mosterfaoui, F. Qi, A. McIlroy, P. R. Westmoreland, M. E. Law, L. Poisson, D. S. Peterka, and M. Ahmed, J. Chem. Phys. **119**, 8356 (2003)

[172] S. Ikuta, J. Chem. Phys. **106**, 4536 (1997)

[173] R. K. Chaudhuria, A. Majumder, and K. F. Freed, J. Chem. Phys. **112**, 9301 (2000)

[174] J. F. Stanton, Chem. Phys. Lett. **237**, 20 (1995)

[175] J. Benedikt, D. J. Eijkman, W. Vandamme, S. Agarwal, and M. C. M. Van de Sanden, Chem. Phys. Lett. **402**, 37 (2005)

[176] J. Benedikt, S. Agarwal, D. J. Eijkman, W. Vandamme, M. Creatore, and M. C. M. Van de Sanden, J. Vac. Sci. Technol. A **23**, 1400 (2005)